A Thesis Submitted for the Degree of PhD at the University of Warwick

TITLE A Wideband Spectrometer for the Measurement of Permittivity

AUTHOR Philip Charles Jarrett Pring

INSTITUTION and DATE University of Warwick 1989

A Wideband Spectrometer for the Measurement of Permittivity

by

Philip Charles Jarrett Pring

A thesis submitted to
the University of Warwick
for admission to the degree of
Doctor of Philosophy

Department of Physics
August 1989

DECLARATION

This thesis is submitted to the University of Warwick in support of my application for admission to the degree of Doctor of Philosophy. It contains an account of my own research work carried out at the University of Warwick under the general supervision of Dr M J A Smith from October 1983 to August 1989. No part of it has previously been used in a degree thesis submitted to this or any other university. The work described in this thesis is the result of my own independent research except where specifically acknowledged in the text.

August 1989 **Philip C J Pring**

ACKNOWLEDGEMENTS

I would like to express my gratitude to Dr M J A Smith, my supervisor, for his guidance and relentless support throughout all stages of the project. I must also thank particularly Mr C F Randle for his patience and skillful technical assistance in much of the mechanical construction.

I am indebted to the staff of both the Electronic and Mechanical workshops of the Department of Physics for their considerable help in the construction stages and to Mr G J Pratt for advice on the interpretation of dielectric data. I am also grateful to Mrs C Gow and Miss H Gilder who skilfully typed the thesis.

The work was funded by a Science and Engineering Research Council studentship, the Department of Physics and the University of Warwick Research and Innovations Sub-Committee. I am grateful to these and in particular the chairman of the Department of Physics, Dr H Mykura, for his organisational skills and personal interest.

Finally, I am thankful for my parents whose conviction and support have enabled me to complete this and previous studies.

August 1989 **Philip C J Pring**

ABSTRACT

Measurements of dielectric relaxations below 1 GHz, and over a wide temperature range, can yield important information on the dynamics of dipoles at both the microscopic and macroscopic levels. Complete characterisations of materials over this region are rare and normally require the integration of several measuring techniques. Although advances in electronics have extended the range of existing techniques, there remains, however, a need for an instrument of superior bandwidth. The present work addresses this problem and is concerned specifically with the methodology and implementation of an automated spectrometer designed to measure the complex permittivity of solids over 13 decades of frequency (between 10^{-5} Hz and 10^{8} Hz) and at temperatures between -185 °C and +600 °C.

Following reviews of current theory and experimental methods, the design and operational criteria of the spectrometer are discussed in principle and in detail. The structure of the operating software is described and examples of algorithms are given.

The successful operation of the spectrometer is demonstrated by experiment, including isothermal investigations of the dielectric behaviour of poly(methylmethacrylate) at 35 °C and low density poly(ethylene) at 30 °C.

CONTENTS

Page

1. Introduction

2. Direct measurement of the electrical impedance of dielectrics

3. Design Criteria and Operational Principles of the Spectrometer

4. Practical Implementation of the Spectrometer

5. Software Structure and Algorithms

6. Spectrometer Performance

References

Bibliography

List of Figures

List of Tables

Following Page

CHAPTER 1

Dielectric Relaxations

1.1 INTRODUCTION

Figure 1.1 shows the various contributions to dielectric polarisation in solid matter experiencing an applied alternating field (1). At far infrared frequencies and above, polarisation results purely from electronic and ionic displacements, the charges being subject to nearly elastic restoring forces, giving rise to resonance-type behaviour (2), (3).

As the frequency is lowered below that of atomic vibration, any molecular dipoles present are progressively able to follow the changing field direction, giving rise to an additional polarisation. In the simplest model (4), the restoring force is a diffusion force of thermodynamic origin imposing a characteristic decay or relaxation time on the dipole motion. Such a process constitutes a dielectric relaxation. At lower frequencies, interfacial and space change movements, where again diffusion mechanisms are involved, behave as relaxing dipoles.

This chapter introduces the Debye relation, describing dielectric relaxation, and examines its consequences. Types of relaxation are classified. A number of empirical relations, representing the real behaviour of dielectrics, are discussed, followed by an outline of theoretical models.

1.2 THE DEBYE THEORY OF DIPOLE RELAXATION

1.2.1 The relaxation time

The Langevin theory of dipole orientation (1) states that, at a temperature T and in a steady, uniform field E, the steady state

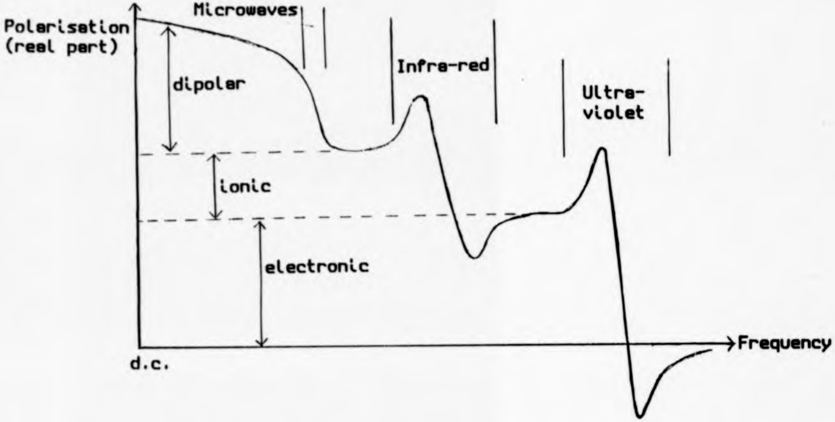

Fig. 1.1 Frequency Dependence of Contributions to Polarisation

statistical distribution of dipoles is such that:

$$\langle \cos\theta \rangle = \frac{\int_0^\pi \cos\theta . \exp(y\cos\theta) d\cos\theta}{\int_0^\pi \exp(y\cos\theta) d\cos\theta} \qquad (1.1)$$

where θ is the angle between dipole and field and $y = \mu E/kT$, μ being the average dipole moment. The brackets < > here and elsewhere refer to the ensemble average at thermal equilibrium.

If the field is suddenly removed, the dipoles will progress, through random collisions, to a situation with no net moment, with a characteristic relaxation time τ. The treatment of this process, according to Debye (4), shows that τ is included in the Langevin factor:

$$f(t) = \exp[y\cos\theta . \Phi(t)]$$

where, for $y<<1$ and $\Phi_0(t) = \exp(-t/\tau)$ then:

$$\exp[y\cos\theta . \Phi(t)] = 1 + y\cos\theta . \Phi_0(t)$$

giving, from (1.1)

$$\langle \cos\theta \rangle = 1/3\ y \exp(-t/\tau) \qquad (1.2)$$

The resultant orientational polarisation is, therefore, of the form:

$$P_{or}(t) = P_{or}(0)[1 - \exp(-t/\tau)] \qquad (1.3)$$

If P_s is the static or steady state polarisation, and P_∞ that at frequencies above the onset of orientational polarisation, then $P_{or}(0)$, the steady state orientational polarisation, is the difference $P_s - P_\infty$ and the total polarisation $P(t)$ is given by:

$$P(t) = P_\infty + P_{or}(t) = P_\infty + (P_s - P_\infty)[1 - \exp(-t/\tau)] \qquad (1.4)$$

By assuming that the field at the dipole is the applied field, the complex permittivity $\varepsilon(\omega)$ may be written

$$\varepsilon(t) = \varepsilon_\infty + (\varepsilon_s - \varepsilon_\infty)[1 - \exp(-t/\tau)] \qquad (1.5)$$

or, by transforming to the frequency domain,

$$\varepsilon(\omega) = \varepsilon_\infty + \frac{\varepsilon_s - \varepsilon_\infty}{1 + i\omega\tau} \qquad (1.6)$$

which is the well-known Debye relation for the frequency response of the complex permittivity of a non-conducting dielectric. Often the real and imaginary parts are separated:

$$\varepsilon'(\omega) = \varepsilon_\infty + \frac{\varepsilon_s - \varepsilon_\infty}{1+\omega^2\tau^2} \quad \text{(capacitive term)} \qquad (1.7)$$

$$\varepsilon''(\omega) = \frac{(\varepsilon_s - \varepsilon_\infty)\omega\tau}{1+\omega^2\tau^2} \quad \text{(resistive or dissipative term)} \qquad (1.8)$$

These functions are shown plotted versus log frequency in Figure 1.2 using nominal relative values. Figure 1.3, obtained by plotting $\varepsilon''(\omega)$ versus $\varepsilon'(\omega)$, is the well-known "Cole-Cole" or Argand plot, used particularly in the comparison of non-Debye behaviour. A Debye process will give a semi-circle of radius $(\varepsilon_s - \varepsilon_\infty)/2$ centred on $((\varepsilon_s + \varepsilon_\infty)/2, 0)$.

1.2.2 <u>Temperature dependence of Debye relaxation</u>

The physical model used by Debye involves the re-orientations of spherical molecules in a viscous medium where

$$\tau = \zeta/2kT$$

ζ is the 'internal friction coefficient' given by Stokes' law:

$$\zeta = 8\pi\eta a^3$$

a is the molecular radius and η is the viscosity of the medium which is thermally activated, that is

$$\eta = \eta_0 \exp(U/kT)$$

where U is the activation energy. Thus the Debye relaxation is also thermally activated and therefore

$$\tau = \frac{8\pi\eta_0 a^3}{2kT} \cdot \exp(U/kT) \qquad (1.9)$$

1.2.3 <u>Influence of the Local Field</u>

The Debye relaxation time was derived assuming that the applied field and local field are identical. Although more detailed calculations can be performed, the effect on the relaxation process can be seen at least qualitatively by considering the Lorentz field

Fig. 1.2 Frequency Dependence of the Contribution to Complex Relative Permittivity due to an Ideal Debye Relaxation

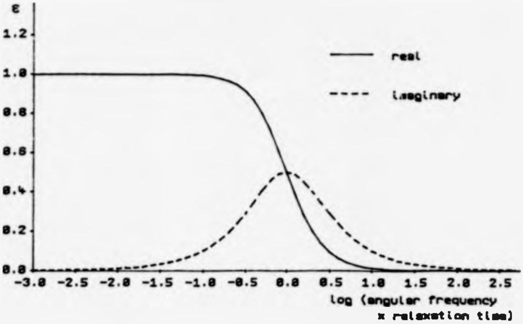

Fig. 1.3 Cole-Cole Plot for an Example of a Debye Relaxation

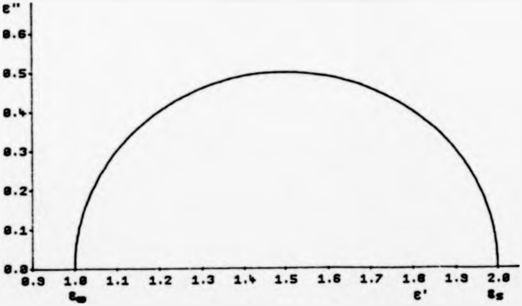

(permittivity values are relative)

correction for solids (1) where:

$$E_{local} = E + \frac{P}{3\varepsilon_o} = \frac{\varepsilon + 2\,\varepsilon_o}{3\varepsilon_o}\,E \qquad (1.10)$$

Therefore:

$$\varepsilon_{local}(\omega) = \frac{3\,\varepsilon\,(\omega)}{\varepsilon(\omega)+2\varepsilon_o} \cdot \varepsilon_o \qquad (1.11)$$

From which we may write:

$$\varepsilon(\omega) = \varepsilon_\infty + \frac{\varepsilon_s - \varepsilon_\infty}{1+i\omega\tau'} \qquad (1.12)$$

where τ' is a modified relaxation time given by:

$$\tau' = \frac{\varepsilon_s + 2\varepsilon_o}{\varepsilon_\infty + 2\varepsilon_o} \cdot \tau \qquad (1.13)$$

So it can be expected that, for solids, the relaxation time of the same dipole will be greater than for liquids, this is experimentally verified (5).

1.2.4 Conducting dielectrics

A conducting dielectric may be treated as a non-conducting dielectric in parallel with a conductance, therefore:

$$\varepsilon(\omega) = \varepsilon_\infty + \frac{\varepsilon_s - \varepsilon_\infty}{1 + i\omega\tau} - \frac{i\sigma}{\omega} \qquad (1.14)$$

where σ is the conductivity.

1.2.5 Multiple relaxations

It is not uncommon for dielectric materials to have more than one dipolar group, in which case:

$$\varepsilon(\omega) = \varepsilon_\infty + \frac{\varepsilon_1}{1+i\omega\tau} + \frac{\varepsilon_2}{1+i\omega\tau_2} + \ldots\ldots\ldots\ldots \qquad (1.15)$$

If the relaxation times are close, then the processes can superpose giving an especially broadened loss-peak in $\varepsilon''(\omega)$ versus frequency. It has been shown (6) that for two equally weighted processes, the τ_1/τ_2 ratio must be at least 5.8 before two loss-peaks can be resolved.

1.2.6 Equivalent circuit model

Since the study of dielectric relaxation normally involves making the sample part of an electrical circuit, it is helpful to have a circuit representation. Figure 1.4 shows the preferred, all-frequency equivalent circuit. The admittance $Y(\omega)$ is given by:

$$Y(\omega) = j\omega C_\infty + \frac{j\omega(C_s - C_\infty) + \omega^2\tau(C_s - C_\infty)}{1 + \omega^2\tau^2} + \frac{1}{R_{dc}} \qquad (1.16)$$

where $C_s = C_\infty + C_{or}$ and $\tau = R_{or} C_{or}$ completing the analogy with the Debye relation. Additional relaxation processes can be modelled by including further components R_{or}', C_{or}' as shown in Figure 1.4.

1.3 CLASSIFICATION OF RELAXATION PROCESSES

1.3.1 Primary or α-relaxation

It is not uncommon for molecules, especially polymers, to have more than one dipolar axis due to the presence of side-chains. In such cases, relaxation due to the longitudinal dipolar component about a short molecular axis is referred to as primary or α-relaxation.

1.3.2 Secondary or β-relaxation

Rotation of the transverse dipole moment about the long molecular axis is known as secondary or β-relaxation. Owing to the generally lower viscous and inertial forces opposing rotation, the relaxation time is shorter than for the corresponding α-process.

1.3.3 Tertiary or γ-relaxation

Crankshaft-type motion of polymer chains is known as tertiary or γ-relaxation. Such restricted movements often give rise to high frequency losses.

1.3.4 Interfacial or Maxwell-Wagner-Sillars relaxation

A Maxwell-Wagner-Sillars (M.W.S.) process describes relaxation in an heterogeneous material, which can be regarded as an assembly of phases each with characteristic ε_i and σ_i.

The simplest M.W.S. relaxation is described by the double-layer capacitor of Figure 1.5. The permittivity behaves as in the Debye case but with a conductivity term:

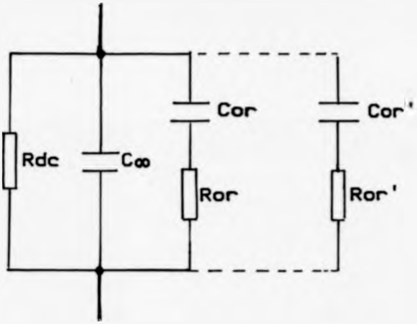

Fig. 1.4 Equivalent Circuit Model of Debye Relaxation

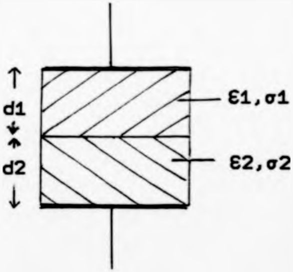

Fig. 1.5 Representation of a Double-Layer Capacitor

$$\varepsilon(\omega) = \varepsilon_\infty + \frac{\varepsilon_s - \varepsilon_\infty}{1 + i\omega\tau} - \frac{i\varepsilon_0}{\omega\tau_0} \tag{1.17}$$

where: $\varepsilon_s = \dfrac{d\sigma_1\sigma_2\ (\varepsilon_1 d_2 + \varepsilon_2 d_1)}{\sigma_1 d_2 + \sigma_2 d_1}$

$\varepsilon_\infty = \dfrac{d\ \varepsilon_1\varepsilon_2}{\varepsilon_1 d_2 + \varepsilon_2 d_1}$,

$\tau_0 = \dfrac{\varepsilon_0\ (d_1\sigma_2 + d_2\sigma_1)}{d\sigma_1\sigma_2}$,

and $\tau = \dfrac{d_1\ \varepsilon_2 + d_2\ \varepsilon_1}{d_1\sigma_2 + d_2\sigma_1}$.

1.3.5 Space charge relaxation

Whenever there are blocking electrodes or boundaries to charge flow, the application of a field will result in an accumulation of space-charge. Thermal diffusion along the concentration gradient will oppose charge accumulation resulting in relaxation-type behaviour.

By application of Poisson's equation with a time dependent field and assuming parallel plate geometry and charge conservation, we find:

$$\varepsilon(\omega) = \frac{\varepsilon\ (1 + i\omega\tau)}{i\omega\tau + (\tanh Y)/Y} \tag{1.18}$$

for a single carrier type, where

$Y = \sqrt{1 + i\omega\tau}\ d/\lambda$ and d is the half width between the parallel plates and λ is the Debye length for carriers. A derivation may be found in Coelho (5).

1.3.6 Hopping processes

The Langevin theory used by Debye was derived for freely rotating dipoles. In reality, dipoles may be constrained to a set of distinct orientations. For example, the dipole formed between an anion vacancy and an anion is an imperfect lattice, changes in dipole orientation taking place by vacancy movement.

A Langevin-type expression can be obtained for the polarisation by considering an assembly of dipoles in a constant field E as temperature T. Each dipole is able to 'hop' between a set of orientations i each with energy ω_i. The average dipole moment $<\mu_E>$ is given by:

$$<\mu_E> = \frac{\sum_i \mu\, e^{-\omega_i/kT}}{\sum_i e^{-\omega_i}} \simeq \frac{\mu^2 E}{3kT} \qquad (1.33)$$

A time dependent treatment (for example(5)) yields a Debye-type relaxation process.

In real hopping systems, vacancies are not so constrained and can move through the material. The d.c. conductivity is then determined by the least difficult 'percolation path' whilst the high frequency limit is set by 'nearest pair' transitions.

1.4 THE RELATIONSHIP BETWEEN ε' AND ε"

1.4.1 Kramers-Kronig relations

If $\phi(t)$ represents the decay function of a displacement D(t), which results linearly from an applied field $E_0\cos\omega t$, then, in the steady state:

$$D(t) = \varepsilon_\infty E_0 \cos\omega t + E_0 \int_0^\infty \phi(x) \cos(\omega t - x)\,dx \qquad (1.20)$$

which may be rewritten as:

$$D(t) - \varepsilon_\infty E_0 \cos\omega t = E_0 \cos\omega t \int_0^\infty \phi(x) \cos\omega x\, dx + E_0 \sin\omega t \int_0^\infty \phi(x) \sin\omega x\, dx \qquad (1.21)$$

Now, from the definition of complex permittivity,

$$D(t) - \varepsilon_\infty E_0 \cos\omega t = E_0 \cos\omega t \,.\, \varepsilon'(\omega) + E_0 \sin\omega t \,.\, \varepsilon''(\omega) \qquad (1.22)$$

Thus, by comparison of equations (1.21) and (1.22), we have:

$$\varepsilon'(\omega) - \varepsilon_\infty = \int_0^\infty \phi(x) \cos\omega x\, dx. \qquad (1.23)$$

$$\varepsilon''(\omega) = \int_0^\infty \phi(x) \sin\omega x\, dx. \qquad (1.24)$$

Since both $\varepsilon'(\omega)$ and $\varepsilon''(\omega)$ are derived from the same function $\phi(t)$, they are not independent. By performing a Fourier transformation of equation (1.24) to obtain $\phi(x)$ in terms of $\varepsilon''(\omega)$ and by substituting for $\phi(x)$ in equation (1.23), we obtain:

$$\varepsilon'(\omega) - \varepsilon_{\infty} = \frac{2}{\pi} \int_{0}^{\infty} \varepsilon''(x) \, . \, \frac{x}{(x^2-\omega^2)} \, . \, dx \qquad (1.25)$$

and, therefore:

$$\varepsilon''(\omega) = \frac{2}{\pi} \int_{0}^{\infty} (\varepsilon'(x)-\varepsilon_{\infty}) . \, \frac{\omega}{(\omega^2-x^2)} \, . \, dx. \qquad (1.26)$$

Equations (1.25) and (1.26) are so-called Kramers-Kronig relations applicable to real linear systems (1). Thus if one component of $\varepsilon^*(\omega)$ is known over the entire frequency range, then the other may be deduced.

1.4.2 Exploitation of the relationship

Certain practical considerations can make the interrelationship between $\varepsilon'(\omega)$ and $\varepsilon''(\omega)$ more useful. Firstly, in order to apply Kramers-Kronig, it is usually only necessary to know the form of one component over the interval of relaxation and not over the entire frequency range. Secondly, equations (1.25) and (1.26) assume no prior knowledge of the response function except that it is linear. However, it has been shown (3) that, even for non-Debye relaxations, the response function can be interpreted, at least mathematically, as the superposition of a distribution $y(\tau)$ of decay processes. In this case, the overall decay function $\phi(t)$ becomes:

$$\phi(t) = \int_{0}^{\infty} e^{-t/\tau} \, y(\tau) \, \frac{d\tau}{\tau} \qquad (1.27)$$

By substitution of $\phi(t)$ into equations (1.23) and (1.24) and by a subsequent Fourier transformation, we obtain:

$$\varepsilon'(\omega) - \varepsilon_\infty = \int_0^\infty \frac{y(\tau)d\tau}{1+\omega^2\tau^2} \qquad (1.28)$$

and $$\varepsilon''(\omega) = \int_0^\infty \frac{y(\tau)\omega\tau d\tau}{1+\omega^2\tau^2} \qquad (1.29)$$

Thus both $\varepsilon'(\omega)$ and $\varepsilon''(\omega)$ are both derived from the distribution function $y(\tau)$. It has been shown, for example by Lynch (7), that if the distribution function $y(\tau)$ is such that $\varepsilon''(\omega)$ is constant with frequency, and if ε_1, ε_2 are values of $\varepsilon'(\omega)$ at frequencies f_1 and f_2 respectively, then:

$$\varepsilon_1 - \varepsilon_2 = \varepsilon'' \cdot \frac{2}{\pi} \log_e \left(\frac{f_2}{f_1}\right) \qquad (1.30)$$

which may be written as:

$$\frac{\Delta\varepsilon'}{\varepsilon'} = 1.5 \tan\delta \log_{10} \left(\frac{f_2}{f_1}\right) \qquad (1.31)$$

where $\Delta\varepsilon'$ represents $\varepsilon_1 - \varepsilon_2$ and ε' is a mean value.

Lynch (7) has also shown that, for a Debye process,

$$\frac{\Delta\varepsilon'}{\varepsilon'} = m \tan\delta \log_{10} \left(\frac{f_2}{f_1}\right) \qquad (1.32)$$

where m lies between 1.0 and 2.3.

Since the Debye process is the narrowest, in frequency terms, that is normally encountered, and since the constant ε'' is the broadest, equation (1.31) is likely to hold, at least within a factor of about 1.5, for most materials. Good agreement has been found with a range of experimental data (7).

Equation (1.14) shows that an additional loss arises from d.c. conductivity. Since conduction is not part of the relaxation process, no commensurate change in $\varepsilon'(\omega)$ is observed. Equations (1.23), (1.24) and (1.31) may, therefore, be employed not only as a check on measured data, but also as a means of identifying d.c. processes.

1.5 EMPIRICAL RELATIONS DESCRIBING DIELECTRIC RELAXATION

1.5.1 Introduction

Very few materials can be considered to obey the Debye relation although it is generally a first order approximation. This section describes some of the empirical relations used to match data and compare theoretical models. A more complete discussion of the mathematical consequences can be found in reference (8) and more empirical examples can be found in (8) and (9).

1.5.2 The Cole-Cole Equation

Curve A on the Cole-Cole plot in Figure 1.6 is an example of the empirical function devised by Cole and Cole (10) where,

$$\varepsilon(\omega) = \varepsilon_\infty + \frac{(\varepsilon_s - \varepsilon_\infty)}{1+(i\omega\tau_o)^{1-\alpha}} \qquad 0 \leq \alpha < 1 \qquad (1.34)$$

A semi-circle with its centre depressed below the real axis is obtained for $0<\alpha<1$. The historical priority of the function has led to its use in the interpretation of much data, covering both solids and liquids.

1.5.3 The Cole-Davidson Equation

The Cole-Davidson equation (11) is represented by curve B on Figure 1.6 and may be written:

$$\varepsilon(\omega) = \varepsilon_\infty + \frac{(\varepsilon_s - \varepsilon_\infty)}{(1 + i\omega\tau_o)^{\beta}} \qquad 0 < \beta \leq 1 \qquad (1.35)$$

For $\beta<1$ a skewed arc is obtained. For $\omega<1/\tau$ the behaviour is Debye-like, whereas, at high frequencies the polarisation falls as $\omega^{-\beta}$.

1.5.4 The Havriliak-Negami Equation

The Havriliak-Negami equation (12) combines the Cole-Cole and Cole-Davidson relations, reducing to either with suitable parameter

Fig. 1.6 Cole-Cole Plots for Examples of Various Empirical Relations

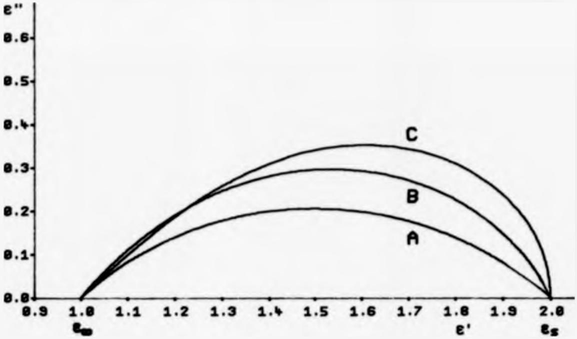

A : Cole-Cole ($\alpha=0.5$)
B : Cole-Davidson ($\beta=0.5$)
C : Havriliak-Negami ($\alpha=0.25, \beta=0.75$)

(permittivity values are relative)

values, it is written:

$$\varepsilon(\omega) = \varepsilon_\infty + \frac{(\varepsilon_s - \varepsilon_\infty)}{(1+(i\omega\tau_o)^{1-\alpha})^{\beta}} \qquad \begin{matrix} 0\leq \alpha<1 \\ 0< \beta\leq 1 \end{matrix} \qquad (1.36)$$

Curve C of Figure 1.6 is representative. The behaviour at low frequencies is determined mostly by α. Whereas, at high frequency, both α and β are significant. The flexibility afforded by two parameters has enabled close data matching of many polymer systems over a considerable frequency range.

1.5.5 <u>The Williams-Watts Function</u>

The Williams-Watts orientational polarisation decay function (13) is described by:

$$\Phi(t) = \Phi_o \exp[-(t/\tau_o)^{\beta w}] \qquad 0<\beta w<1 \qquad (1.37)$$

A skewed Cole-Cole plot is produced with a loss-peak lower than for Cole-Davidson. Not surprisingly, the Havriliak-Negami equation gives better data fits.

1.5.6 <u>The Fuoss-Kirkwood Function</u>

The Fuoss-Kirkwood function (14) is based on a theoretical treatment of chain relaxation in an hydrodynamic continuum, where:

$$\varepsilon''(\omega) = \frac{2\,\varepsilon''_{max}}{(\omega\tau_o)^{-\alpha}+(\omega\tau_o)^{\alpha}} \qquad 0< \alpha<1 \qquad (1.38)$$

The result is similar to the Cole-Cole equation.

1.5.7 <u>The Jonscher Function</u>

The Jonscher function (15) is a two parameter generalisation of the Fuoss-Kirkwood function, allowing the tailoring of both high and low frequency behaviour. In this case,

$$\varepsilon''(\omega) = \frac{A}{(\omega\tau_o)^{-m}+(\omega\tau_o)^{1-n}} \qquad \begin{matrix} 0<n<1 \\ 0<m<1 \end{matrix} \qquad (1.39)$$

Hill (16) has added another parameter:

$$\varepsilon''(\omega) \simeq \frac{(\omega\tau_o)^{m}}{[1+(\omega\tau_o)^{2s}]^{(m+1-n)/2s}} \qquad \begin{matrix} 0<n<1 \\ 0<m<1 \\ 0<s<1 \end{matrix} \qquad (1.40)$$

1.6 THEORETICAL MODELS OF NON-DEBYE RELAXATION

1.6.1 The Dipole Correlation Function

Many theoretical models relate non-Debye behaviour to dipole-dipole interactions, the dipole-correlation function is a formal way of expressing these. A distribution function $\rho(t)$ for dipoles of moment μ_i is proposed such that:

$$P_{or}(t) = (1/v) <\Sigma i \; \mu_i \; \rho(t)> \qquad (1.41)$$

where 1/v is for unit volume. Now $\rho(t)$ is not an explicit function of time, but varies implicitly as a result of the individual dipole coordinates qi and momenta p_i.

i.e. $$\frac{d\rho(t)}{dt} = \frac{\partial\rho(t)}{\partial t} + \sum_i \left(\frac{\partial\rho_i}{\partial t} \cdot \frac{\partial\rho(t)}{\partial p_i} + \frac{\partial q_i}{\partial t} \cdot \frac{\partial\rho\,(t)}{\partial q_i} \right) = 0 \qquad (1.42)$$

for all distributions

or $$\frac{\partial\rho(t)}{\partial t} + \sum_i \left(\frac{\partial H}{\partial q_i} \cdot \frac{\partial\rho}{\partial p_i}(t) - \frac{\partial H}{\partial p_i} \cdot \frac{\partial\rho}{\partial q_i}(t) \right) = 0 \qquad (1.43)$$

where H is the system Hamiltonian. We can also write:

$$\frac{\partial\rho(t)}{\partial t} + L\rho(t) = 0 \qquad (1.44)$$

where L is the classical Louisville many-body operator. On application of a field E(t), the Hamiltonian contains an extra term involving the new potential. Following the convention of E(t) parallel to the z-axis and using the Kubo theory of linear response (17) we obtain:

$$\frac{\partial\rho_1(t)}{\partial t} + L_o\rho_1(t) = E(t) \; \Sigma_i \; \frac{\partial\mu_{zi}}{\partial z_i} \; \frac{\partial\rho_o}{\partial p_{zi}} = -E(t)(\Sigma_i \frac{\partial\mu_{zi}}{\partial t})\rho_o/kT \qquad (1.45)$$

where $\rho_o = A\exp(-H_o/kT)$ and the subscript 'o' refers to the no-field equilibrium situation and $\rho_1(t)$ is the perturbation. Solving for $\rho_1(t)$ and using (1.40) we get:

$$P_{or_z}(t) = -(kTv)^{-1} \int_{-\infty}^{t} dt' E(t') <(\Sigma_i \mu_{zi}) e^{-(t-t')L_o} \; (\Sigma_i \; \frac{\partial\mu_{zi}}{\partial t}) \rho_o> \qquad (1.46)$$

where the limit '$-\infty$' refers to the equilibrium situation. We satisfy the above by allowing:

$$E(t') = E_o \exp\,(i\omega t')$$

The macroscopic correlation function $\Phi_{\mu z}(t)$ is introduced as:

$$\Phi_{\mu z}(t) = <(\Sigma_i \mu_{zi})e^{tL_0}(\Sigma_i \mu_{zi})\rho_0>$$

$$= <(\Sigma_i \mu_{zi})(\Sigma_i \mu_{zi}(t)\rho_0)> \qquad (1.47)$$

Using the definition of $\Phi_{\mu z}(t)$, Laplace transforming equation (1.23) to the frequency domain and dividing by E_0, we have:

$$\epsilon(\omega) - \epsilon_\infty = (KTv)^{-1}[\Phi_{\mu z}(0) - j\omega \mathcal{L}\,\Phi_{\mu z}(t)] \qquad (1.48)$$

showing that $\Phi_{\mu z}(t)$ is equivalent to the step response of the orientational polarisation. In the Debye situation, where dipole-dipole interactions are not included, then:

$$\Phi_{\mu z}(t) = <\mu_z(0)\mu_z(t)\rho_0> = k'\psi(t) \qquad (1.49)$$

where $\psi(t)$ is the microscopic or dipole correlation function. In this case, each individual dipole moment is an eigenfunction of the Louisville operator.

A detailed discussion of the relationship between the macroscopic and microscopic correlation functions for non-Debye systems is given in Bottcher and Bordewijk (8).

The many-body behaviour resulting from the inclusion of the Louisville operator is far too general for a practical model. Those theories which involve many-body, dipole-dipole interactions must, therefore, include suitable approximations and statistical methods.

1.6.2 Distributions of Relaxation Times

Non-Debye behaviour can result from the superposition of a number of Debye processes with different relaxation times. It has been customary to find either continuous distribution functions or multiple discrete relaxations to match empirical data. The correlation function then becomes either an integral or a sum over a distribution of exponentials, e.g.:

$$\Phi(t) = \sum_i A_i \exp(-t/\tau_i) \qquad (1.50)$$

Where loss-peaks cover many decades, logarithmic distribution functions are introduced. Bottcher and Bordewijk (8) have described distribution functions corresponding to the classical Cole-Cole plots described in section 1.4. In some polymer systems, where molecular weight distributions arise, such analyses may be helpful. However, in most cases, the distribution gives little more insight than the original empirical behaviour.

1.6.3 Defect diffusion and fluctuation

The first defect diffusion model, introduced by Glarum (18), is based on the postulate that the decay of polarisation is the result of two processes:

i) a Debye exponential depending on the instantaneous polarisation,

ii) the randomising of dipole orientation by interaction with mobile defects.

The correlation function is given by:

$$\Phi(t) = \exp(-t/\tau_o)[1-P(t)] \qquad (1.51)$$

where P(t) is the probability of arrival, at time t, of the defect that was nearest at t = 0. With P(t) given by diffusion theory, the frequency dependence of the orientational polarisation is of the form:-

$$P_{or}(\omega) \propto \frac{1}{1+i\omega\tau_o}\left[1 + \frac{j\omega\tau_o}{1+(\tau_d/\tau_o)^{\frac{1}{2}}(1+i\omega\tau_o)^{\frac{1}{2}}}\right] \qquad (1.52)$$

where τ_o is the dipole relaxation time and τ_d the diffusion relaxation time. Debye behaviour results from $\tau_d \gg \tau_o$, Cole-Davidson from $\tau_d = \tau_o$ and Cole-Cole from $\tau_d \ll \tau_o$.

Other models have been developed following this approach, notably; Phillips, Barlow and Lamb (19) who considered two defects, Bordewijk (20) who considered all defects and Hunt and Powles (21) who developed a 3-D model. Anderson and Ullman (22) have developed a 'fluctuation model' assuming a restricted Brownian motion of the environment around the dipole. The latter predict a broadening of the relaxation time distribution on cooling, which is not observed in practice.

1.6.4 Shore and Zwanzig Model

The Shore and Zwanzig model (23) introduces a specific dipole-dipole coupling such that the dipole motion is governed by:

i) rotational diffusion as in Debye,

ii) a torque proportional to the cosines of the differences in the angles of rotation of nearest-neighbour dipoles, which are grouped in chains.

Debye behaviour results from short chains; with long chains Havriliak-Negami behaviour is found.

1.6.5 Jonscher, Dissado and Hill Model

The many-body theory of Jonscher is claimed to have universial application (24). A refinement introduces the theory of Dissado and Hill (25) outlined below.

The dielectric is modelled using 'correlated states' where, in a disordered arrangement, the constituent elements are mutually interactive. A two-level potential well describes the relaxation process, the macroscopic dipole moment being determined by the occupancies of the wells. The potential difference between the bottoms of the two wells is a function of both the local potential and the occupancy. Transitions between the wells occur by three mechanisms:

i) 'Large transitions'. A particle jumps over the potential barrier into the other well. The process is thermally activated resulting in Debye-type behaviour near the loss peak, ω_p.

ii) 'Local flip transitions'. The result of 'configurational tunneling' or co-operative local adjustments after which the total polarisation is altered. The process is not thermally activated and is reversible. The time scale is 10^{-12} seconds. This process gives rise to the parameter n in the empirical Johnsher equation (see section 1.4.7) n=1 corresponds to total correlation of the flip processes.

iii)'Local flip-flop transitions'. Flip-flop transitions involve two oppositely directed tunneling processes which leave the macroscopic polarisation unchanged but alter the energy distribution among the states. The time scale is 10^{-9} seconds.

The correlation of flip-flop processes is represented by 'm' in the Johnsher equation, m = 1 for total correlation.

The behaviour is similar to Havriliak-Negami. Critics have pointed out that, according to the model, Cole-Davidson behaviour can only occur at high frequency or for total flip-flop correlation, which is not fully consistent with experiment.

1.6.6 Ising Model

Rather than consider explicit dipole-dipole interactions, the Ising model, applied by Anderson (26), introduces constraints of the chain dynamics to the dipole motion. Broadened loss-peaks and skewed-arc behaviour result.

1.7 GENERALISED ANALYSIS OF EXPERIMENTAL DATA

The existence of the emprical formulae, described in section 1.5, and the number of differing theoretical models, described in section 1.6, indicates that dielectric relaxation is not completely understood. There is, therefore, not only a need for further investigation, but also an apparent problem for those presenting and interpreting data. A pragmatic approach, based on commonly-accepted principles, but not theoretically specific, is often adopted.

It has been seen in section 1.4 that a relationship exists between the real and imaginary components of linear dielectric spectra and that d.c. conductivity can be separated readily.

The existence of α-, β- and other relaxation processes is not in dispute. Although the interactions between relaxing dipoles and their surroundings vary in reality and in interpretation, the processes are normally activated. Although the temperature dependence may differ from that of equation (1.9), since relaxation is fundamentally of thermodynamic origin, a dominant exponential term will, in general, enable an equivalent activation energy to be ascribed to any relaxation process. Thus it is often possible to characterise and resolve multiple processes within a given material.

Determination of activation energy normally involves finding the frequency at which the loss component for a given process is at a maximum, that is a determination of the relaxation time, and plotting its logarithm against the reciprocal measurement temperature. If the measurement is repeated at different temperatures, then the activation energy may be derived from the gradient. Since the relaxation time can vary exponentially with temperature, measurements over a wide frequency range are often required.

Figure 1.7 is a contour map, due to Pratt and Smith (27), showing the variation of the loss tangent ($\varepsilon''/\varepsilon'$) of a grade of commercial polycarbonate with both frequency and temperature. Although a detailed analysis reveals up to nine separate relaxation processes, three very distinct dispersion regions can be identified. The process between 162 °C at 30 Hz and 190 °C at 100 kHz has been shown to have an activation energy compatible with the known

Fig. 1.7

Contour Map Showing the Variation of the Loss Tangent of LEXAN 141 Polycarbonate with Temperature and Frequency (Pratt and Smith)

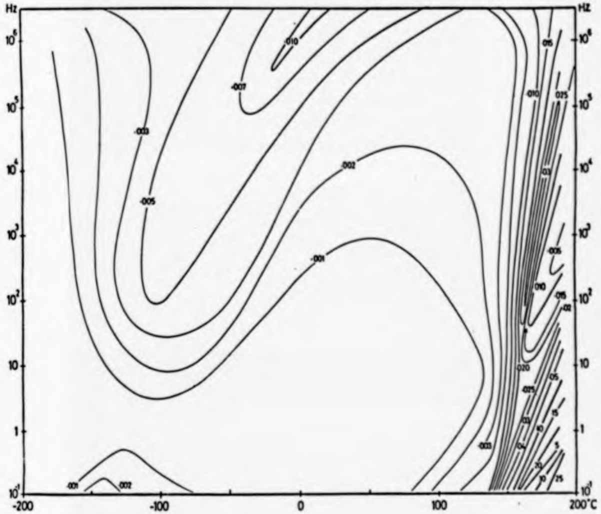

α-process in polycarbonate. Between -110 °C at 3 Hz and 15 °C at 3 MHz, is an extensive multi-component β-process. At low frequencies and temperatures above 150°C, very high losses result from Maxwell-Wagner-Sillars type relaxations.

It is only after such preliminary analysis that more detailed theoretical modelling or deconvolutions are practical. It is apparent that, at any level of analysis, measurements should cover the widest possible frequency and temperature range.

1.8 CONCLUDING REMARKS

Dielectric relaxation may be described, at least to first order, by the Debye relation. A number of empirical equations representing non-Debye behaviour have been described. Those equations with at least two variable parameters, describing respectively the high and low frequency behaviour, give the closest data fits.

The broadening of loss-peaks has led to the development of models involving dipole interactions with the surroundings. Quite different theories ranging from dipole-dipole interactions to defect diffusion can give approximations to experimental behaviour.

In order to approve theoretical models, it is necessary to get detailed descriptions of actual relaxation behaviour. Temperature dependence and activation energy determination, as well as broadband frequency measurements are therefore crucial. Investigating the effects of dipole concentration on relaxation time may help to take proper account of dipole-dipole interactions.

CHAPTER 2

Measurement of the electrical impedance of dielectrics

2.1 INTRODUCTION

The importance of the wideband measurement of permittivity was mentioned in chapter 1. A number of measurement techniques have been developed (28), of which measurements of sample impedance cover the widest frequency range. However, at present, individual techniques cover typically only 4 or 5 decades in frequency. The development of a single method which could cover more than 12 decades in frequency promises a number of benefits and avoids some of the difficulties associated with the use of multiple techniques.

The use of more than one measuring technique often requires a change of sample size and, hence, of sample. When measurements are performed on heterogeneous samples or samples sensitive to pretreatment (for example, polycarbonate (29)), inconsistencies between samples may lead to significant mismatches in the data. Such mismatches are avoided if a single sample is used for all measurements.

The use of a single sample cell helps to ensure that the sample environment is consistent at all frequencies. Stray impedances, spatial effects, temperature, contact pressure, atmosphere and external stimuli can all be maintained with greater ease.

Although sample cells have been constructed for use with multiple technqiues, for example Baker (30), feed and take-off impedances, as well as other circuit conditions such as d.c. bias and signal voltage level across the sample, may alter significantly following a change of technique.

A single method is more convenient for the user and is more suited to automation than a combination of techniques.

Inevitably, any method with an extended bandwidth will involve compromises which may not need to be made in narrowband or single frequency techniques. It is, therefore, expected that the former is unlikely to compete in terms of ultimate accuracy with more specialised measurement schemes.

Direct electrical measurements of impedance extend from d.c. to microwave frequencies (28), (31), (32), (33). Traditionally, above about 100 MHz, where the measurement wavelength becomes comparable with typical sample dimensions, distributed impedance techniques, which include transmission line measurements (34), (35), cavity resonance (36), (37) and microwave bridges (38), (39), have been used. Although modern devices, such as the network analyser and the transient recorder, have extended the lower frequency limit, the use of distributed impedance techniques below about 1 MHz offers no advantage over lumped methods except where sample access requires a transmission line (35), or when the sample itself is in cable form (40). It is in the frequency range below about 300 MHz, where, for most samples, the lumped impedance approximation is valid, that the potential exists for wideband operation over at least 12 decades.

This chapter describes, in principle, various lumped impedance measurement configurations and, in particular, examines the potential of each for the development as the central element of a wideband spectrometer operating from frequencies of less than 10^{-4} Hz to frequencies approaching the lumped impedance limit.

In the following discussions, the sample is assumed to be in the form of a two-terminal capacitor, although, where appropriate, the suitability of methods for three-terminal measurements is stated.

The term VLF is used here and elsewhere to denote frequencies at or below 0.1Hz.

2.2 THE ACTIVE CURRENT-TO-VOLTAGE CONVERTER

An arrangement for measuring sample impedance using an active current-to-voltage (I-V) converter is shown in Figure 2.1. The sample forms the input impedance of a virtual earth amplifier. For a voltage $V_{IN}(t)$ at the input, assuming that the amplifier has infinite gain and infinite input impedance, the output voltage $V_O(t)$ is given by:

$$V_O(t) = -V_{in}(t).\ Zf/Zs \tag{2.1}$$

where Zs and Zf are the sample and feedback impedances respectively. Zf is usually made primarily capacitative so that it scales similarly in impedance to the sample with changing frequency.

For frequency domain measurements, the excitation $V_{IN}(t)$ would be a sinusoid, and the resultant $V_O(t)$ would be correlated with a reference signal to determine its magnitude and phase and hence to determine the sample impedance. The process would be repeated for a number of different frequencies over the range of interest. The functions of excitation and correlation are conveniently provided by a frequency response analyser (FRA), for example Solartron Instruments 1255 (41), although a transient recorder can be used for detection (42). The I-V converter is also the most common circuit used in d.c. transient measurements based on the method of Hamon (43). The excitation $V_{IN}(t)$ is then a known or measured transient, commonly a voltage step; the output $V_O(t)$ feeds a transient recorder. The sample impedance is determined, over a frequency range, by subsequent Fourier analysis. The initial high speed transitent, which is often of large magnitude and outside of the detector bandwidth, has been reduced by impressing an equal and opposite excitation across an air capacitor, of similar capacitance to the

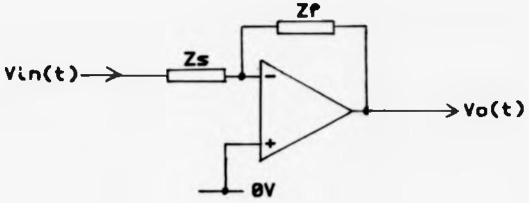

Fig. 2.1 Active Current-to-Voltage Converter

sample, and also connected to the virtual earth point (44), (45). Another method uses "unorthodox stimuli" to reduce the intial transient (46).

It may be generally stated that, using transient techniques, the lower proportion of excitation energy in each part of the measurement frequency spectrum results in a lower signal-to-noise ratio than in the equivalent frequency domain method with a reasonable point density. This is particularly true of step excitation at higher frequencies, since the magnitude of the Fourier components fall linearly with increasing frequency. For this reason, high voltage transients are often used, for example (44), although problems may arise with sample linearity. It is also easier to separate a single frequency component from noise than it is to separate an unknown transient. Since the microcomputer has become a common laboratory instrument, the construction of a time domain spectrometer is far simpler than its frequency domain equivalent. One other advantage of time domain measurements is the time taken for measurements, a whole spectrum taking between three and ten periods of the lowest frequency required. Further discussion of the relative merits of frequency and time domain methods has been presented, for example (47) and (48).

Since the sample is d.c. coupled to the amplifier, the I-V converter can be used at very low frequency (VLF). The limit occurs when the sample current, which can be very small, is masked by the amplifier bias current or by flicker noise at the high impedance input.

Equation 2.1 assumes that the amplifier has infinite gain. In reality, the gain will be both finite and a function of frequency, in which case:

$$V_O(t) = -V_{IN}(t).\frac{Z_f}{Z_s}\frac{1}{\left(1 + \frac{Z_s+Z_f}{A(\omega)Z_s}\right)} \qquad (2.2)$$

where $A(\omega)$ is the amplifier gain. If, for example, Z_f is equal to Z_s and $|A(\omega)|$ is only 100, then from equation 2.2 there will be a 2% error in the I-V conversion. Although corrections can be made, in practice, an open-loop gain of at least 100 is required with a phase shift of less than 45° if only to avoid saturation of the input stages. With multi-stage operational amplifiers, it is possible to achieve gains far in excess of this requirement at medium and low frequencies. However, above 10 MHz, suitable amplifiers are not available. A further complication is that the sample with its mounting and connecting leads is in the gain determining circuit, which may be a particular problem at high frequency.

A modern application of the I-V converter is the 'Chelsea Dielectric Interface' (49), which, when combined with the Solartron 1255 FRA, covers the frequency range 10^{-5} Hz - 10^{7} Hz. The peak loss angle resolution is 4×10^{-5} rads although this rises to 10^{-3} above 1 MHz. The Solartron 1255 FRA has a quoted phase accuracy of 3×10^{-3} rads up to 1 MHz, rising to 6.9×10^{-2} rads at 20 MHz, for integration times greater than 200 mS and when inputs exceed 10% of full scale.

Active I-V converters are especially useful in measurements on electrochemical and semiconductor systems, for example (50) and (51), where d.c. bias level is important. Any offset in Vin or at the non-inverting input of Figure 2.1 will always appear across the sample.

The connection of the sample to a virtual earth particularly facilitates the use of three-terminal specimens, see for example (44), (52).

Similar measurements can also be made using a passive I-V converter, that is a known impedance in series with the sample across which a voltage is developed, for example (28), (53). Although higher voltages and frequencies can be reached, the loss of signal through potential division, increased sensitivity to detector input impedance and extra difficulty in adding bias make the passive circuit generally less attractive.

2.3 LUMPED IMPEDANCE RESONANCE

Measurement techniques based on the method of Hartshorn and Ward (54), in which the sample forms part of a resonant circuit, are suitable for low loss specimens (loss angle $<10^{-2}$ rads) between 1 kHz and 300 MHz, for example (55), (56), (57). Although both series and parallel arrangements are used, the latter have the advantage that the components of the resonant circuit can share a common ground which simplifies construction and correction for strays. The circuit used by Benadda et al (58), covering 100 kHz-300 MHz, is shown in figure 2.2. In this case, the resonant frequency is determined with the sample in position and at the same time, the voltages V_1 and V_2 are recorded. With the sample removed, the variable capacitor C is adjusted until a resonance is obtained at the same frequency as before; V_{12} and V_2 are again recorded. The sample capacitance is given directly by the change in C whilst the sample resistance is given by:

$$R_s = \frac{1}{j\omega C_1\left(\frac{V_{1s}}{V_{2s}} - \frac{V_{10}}{V_{20}}\right)} \tag{2.3}$$

where V_{1s}, V_{2s} and V_{10}, V_{20} are the voltages recorded in the sample and no sample situations respectively.

It is also possible to measure the resonant frequency with and then without the sample; such systems are easier to calibrate but

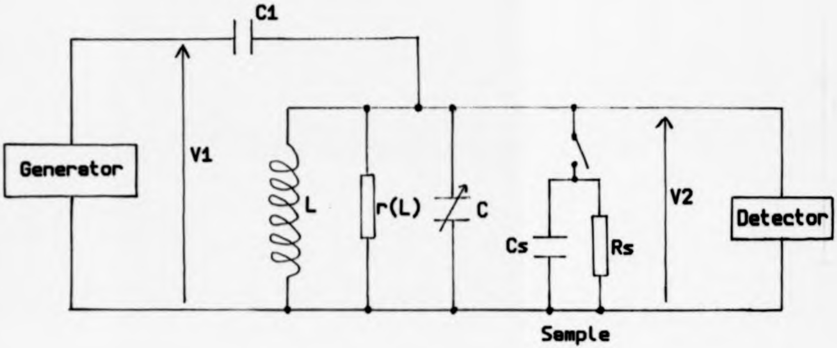

Fig. 2.2 Lumped Impedance Resonance Scheme of Benadda et al.

more susceptible to the effects of impedance artefacts than those operating at one resonant frequency.

With very low loss materials, a loss-angle resolution below 1μrad has been reported by Reddish et al (56). Measurements of capacitance have been made to 0.2% (57). The maximum frequency is limited by distributive effects. Problems with suitable inductors set the lower frequency limit. Although negative impedance converters (59) could be used to simulate large inductors, it is expected that the measurement process would become awkward and lengthy much below 10 Hz. Although at the highest frequencies, two terminal samples must still be used, improvements in active guard circuits has enabled the use of three terminal samples up to at least 4 MHz (60).

2.4 LUMPED IMPEDANCE BRIDGES

2.4.1 Introduction

Lumped impedance bridges have no feedback at the measurement frequency and therefore are unconditionally stable and as such possess wideband potential. A very wide range of impedance measuring bridges has been developed. In order to explore the general benefits and drawbacks without exhaustive detail, bridges suitable for dielectric measurements are divided into three classes: 4-arm, 3-arm and 2-arm bridges.

2.4.2 4-arm bridges

The arrangement of a 4-arm bridge is shown in Figure 2.3. The source V remains fixed in amplitude whilst the impedances are altered until the detector output is zero, which occurs when:

$$\frac{Z_1}{Z_2} = \frac{Z_4}{Z_3} \tag{2.4}$$

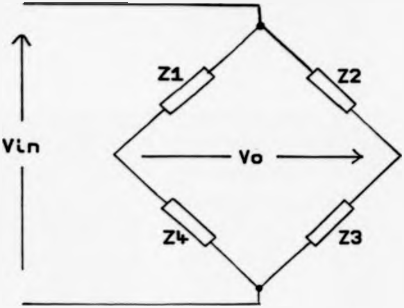

Fig. 2.3 Common Form of 4-Arm Bridge

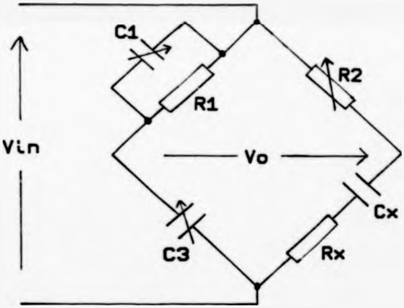

Fig. 2.4 Schering Bridge

If, for instance, Z_1 represents the complex sample impedance, at least one of the other impedances must also be complex. At least two components of impedance must be alterable and these are normally arranged such that the real and imaginary components of the sample impedance can be balanced independently, thereby simplifying the balancing procedure.

An example is the Schering bridge (61) a form of which is shown in Figure 2.4. The resistor R_z is switched to select the impedance range, whilst balance is achieved by adjusting the variable capacitors C_1 and C_3. At balance:

$$R_x = \frac{C_1}{C_3} R_2 \quad \text{and} \quad C_x = C_3 \frac{R_1}{R_2}. \tag{2.5}$$

Variable capacitors are used rather than variable resistors because they can be more perfectly constructed. The Schering bridge is normally used in the frequency range 30 Hz-300 kHz, limited at high frequency by stray capacitance. The low frequency limit depends on the sample loss and whether isolating transformers are used. Measurements to 0.01% can be made over a narrow capacitance range.

The Schering bridge can be used with relatively high drive signals, for example (62), or with d.c. bias (63). Three terminal samples cannot be used without the addition of a second pair of balance arms (Wagner earth), thereby complicating the balance procedure.

Other 4-arm bridges have been developed for specialised purposes, such as the measurement of highly conducting materials.

2.4.3 3-arm bridges

The common form of 3-arm bridges is shown in Figure 2.5. Three voltage sources each drive an arm of the bridge at the measurement frequency. The arm formed by the sample is fed from the reference or

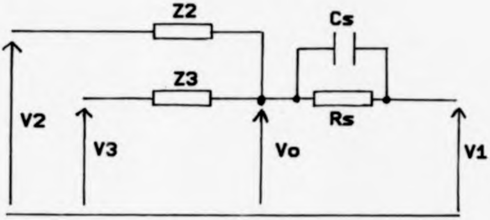

Fig. 2.5 Common Form of 3-Arm Bridge

zero phase channel whilst the impedances Z_2 and Z_3 are fed from quadrature and antiphase signals respectively. Normally Z_2 and Z_3 would be of the same impedance type as the sample so that all impedances scale similarly with frequency. At balance:

$$C_s = \frac{V_3}{j\omega Z_3 V_1} \text{ and } R_s = \frac{Z_2 V_1}{V_2} \tag{2.6}$$

In the 3-arm bridge of Thompson (64), Z_2 and Z_3 are variable air capacitors and V_1, V_2 and V_3 are fixed amplitude sources. The antiphase signal is provided by a transformer with a centre-tapped secondary, whilst the quadrature signal is obtained using an integrating amplifier with adjustable feedback for variable frequency operation. Loss angle measurements between 1 and 10^{-4} rads can be made over the frequency range 30 Hz-1 MHz. A computer-controlled version in which Z_2 and Z_3 are switchable, but primarily fixed, and in which V_2 and V_3 are variable, has been demonstrated by Van Roggen (65). A major source of error is through maladjustment of the primary phases, which is a particular problem at high frequency. The low frequency limit for a d.c.-coupled 3-arm bridge will depend on detector input impedance and noise, and can be as low as 10^{-5} Hz.

An automated 3-arm bridge based on multiplying digital-to-analogue converters has been developed by Cavicchi and Silsbee (66). The optimum capacitance resolution is about 0.1%, whilst loss angle errors of about 10^{-3} are achieved. The high frequency limit of 30 kHz is determined by op-amp performance, whilst the low frequency limit of 40 Hz is the result of detector flicker noise.

Since these bridges are always balanced to earth, earthed guard rings may be added without alteration of the balance conditions.

2.4.4 2-arm bridges

The class of 2-arm bridges may be sub-divided into three types; unbalanced, partially balanced and balanced. Examples of the unbalanced bridge include the dielectric spectrometer of Edmonds and Smith (67) and the computer controlled method of Hayward et al (47). The common form is shown in Figure 2.6. The reference arm is fed from a voltage source in antiphase with the sample arm voltage source. In this way, some or all of the real part of the sample response can be backed-off to preserve the detector dynamic range. (A similar technique has been used in time domain measurements, see for example Hyde (44).) The sample impedance is then calculated from the amplitude and phase of the out-of-balance signal. By using the virtual earth detector, Hayward et al have removed the effects of impedance to ground at the point of detection, which is normally a problem with unbalanced bridges, at some cost to bandwidth. Since both bridge arms contain impedances of a similar type, the frequency range is effectively limited by the VLF behaviour of the detector and the high frequency errors in both the phase-splitter and the phase-sensitive detector. Edmonds and Smith detected loss angles below 10^{-3} rads from 1 Hz to 1 MHz, whilst Hayward et al measured below 10^{-4} rads between 10^{-3} Hz and 10^{4} Hz.

The wideband bridge of Pratt and Smith (68), shown schematically in Figure 2.7, is a type of partially balanced 2-arm bridge. Operation involves a capacitative substitution and a partial resistive substitution. With the sample switched in, the capacitor C_1 is adjusted to minimise the detector output and the remaining out-of-balance signal is recorded using a quadrature phase-sensitive detector. With the sample switched out, C_1 is re-adjusted until the bridge is completely balanced; the change between the two settings of C_1 being equal to the sample capacitance. Various values of R_1,

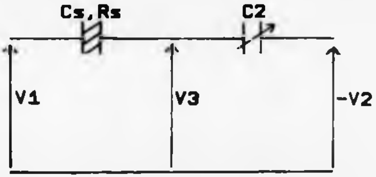

Fig. 2.6 Unbalanced 2-Arm Bridge

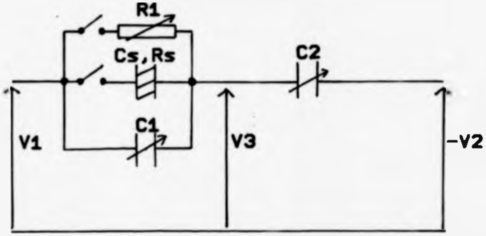

Fig. 2.7 Partially-Balanced 2-Arm Bridge (Pratt and Smith)

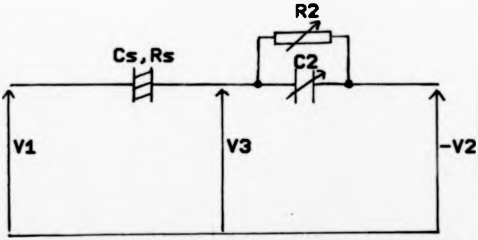

Fig. 2.8 Variable Impedance Balanced 2-Arm Bridge

which consists of a switched bank of fixed resistors, are then switched in until the quadrature output of the phase-sensitive detector is similar, but not necessarily equal, to that with the sample switched in. Thus the method involves balancing to determine the real part of the sample impedance whilst the imaginary part is determined by comparing the out-of-balance signal with that due to standard components. Loss tangents between 1×10^{-5} and 10 can be detected. The frequency range is from 30 mHz to 10 MHz with some degradation in performance at the extremes. Extension of the lower frequency limit is unlikely as, even if suitably high resistor values could be obtained and switched successfully, the method would be very time consuming. The high frequency limit is due to a combination of stray capacitance and distributive effects resulting from the spatial extent of the apparatus.

A form of partially balanced, transformer-fed 2-arm bridge has been presented by Lynch (69). For the measurement of large sample conductances, the sample is switched in to an initially balanced bridge. Capacitative adjustments are made to minimise the detector output magnitude. The minimum magnitude, due to the sample conductance, is recorded. With the sample switched out, a calibrated capacitative change from the initial balance condition is made such that the detector output magnitude is the same as recorded with the sample in position. From the changes in capacitance, the sample capacitance and conductance can be determined. For low loss samples, the minimum detector output is recorded with and without the sample, after capacitative adjustments only. The detector response to a calibrated change in arm capacitance is determined to complete the measurement, from which the sample conductance can be computed if the detector law is known. Refinements of the method are included.

Measurements of dielectric loss to within a few microradians have been recorded. The technqiue is suggested as a useful extension of bridge methods in the range of 1 MHz to 100 MHz where difficulties would otherwise arise in the effecting of calibrated variable resistors or equivalents.

There are two types of balanced 2-arm bridge, the variable impedance and the variable voltage bridges. A variable impedance 2-arm bridge suitable for dielectric measurements is shown in Figure 2.8. The voltage sources V_1 and V_2 are in antiphase. A balance occurs when:

$$C_s = C_2 \left| \frac{V_2}{V_1} \right| \text{ and } R_s = R_2 \left| \frac{V_1}{V_2} \right| \qquad (2.7)$$

An example is a form of the transformer ratio arm bridge (63), (70), Figure 2.9, in which the voltage sources V_1 and V_2 of Figure 2.8 consist of the closely coupled secondary windings of a transformer, the primary of which is fed with a signal at the measurment frequency. The amplitudes of V_1 and V_2, and hence the impedance range, can often be set by adjusting the ratio of the transformer secondaries. By using low-leakage toroidal transformers, the transformer ratio can be made accurate to 1 part in 10^7. Various modifications and improvements have been made, for example, by feeding R_2 and C_2 from separate taps, very high effective resistor values can be realised (28). The use of coaxial techniques (71) and active shielding (72) ensure a loss angle resolution of at least 1 µrad. Capacitances can be measured to at least one part in 10^4. The major sources of error are flux leakage and loading effects of unbalanced arms. A typical transformer ratio bridge might cover the frequency range 10 Hz- to 1 MHz, although high frequency versions can reach 300 MHz (73). The effective transformer ratio is difficult to determine at higher frequencies as stray capacitances become significant. Below about 10 Hz transformers are ineffective.

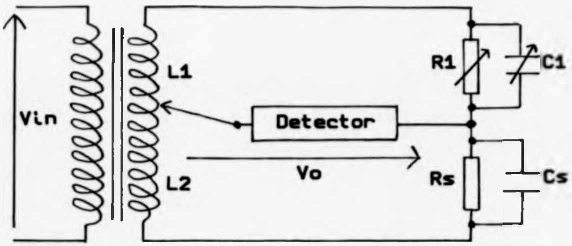

Fig. 2.9 Transformer-Ratio Arm Bridge

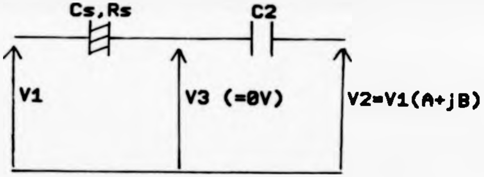

Fig. 2.10 Voltage Balanced,Fixed Impedance
2-Arm Bridge

Transformer bridges are widely used in dielectric measurement because of their high accuracy, fairly wide frequency range and ready adaptation to three terminal samples.

The circuit of a voltage balanced, fixed impedance 2-arm bridge is shown in Figure 2.10. In order to achieve a balance, both the relative amplitude and phase of the voltage sources V_1 and V_2 must be adjusted appropriately. If the real and imaginary components of the ratio between V_2 and V_1 are A and B respectively, then, at balance:

$$C_s = -A\,C_2 \quad \text{and} \quad R_s = \frac{1}{B\omega C_2} \qquad (2.8)$$

The bridge structure has a superior wideband potential for five major reasons. Firstly, the impedances are primarily capacitative, no other type of component can be constructed nearer to its ideal, particularly at high frequency. Secondly, since the impedances are not variable, they can be made small to minimise wavelength effects. Thirdly, the bridge components will scale in impedance similarly with frequency. Fourthly, the symmetry of the structure minimises path length differences which would otherwise lead to phase errors.
Lastly, stray impedances between any point and the common ground do not affect the balance position. The arrangement is, therefore, suitable for use with three-terminal samples where the guard terminal is at ground potential.

The difficulty with any voltage balanced bridge is in ensuring that the voltage sources produce the required amplitudes and phases. If suitable sources can be made, then the high frequency limit is likely to be near the onset of distributive impedance effects at around 100MHz. As is the case with other d.c.-coupled bridges, the VLF limit is determined chiefly by the detector and the integrity of the balance capacitor.

Many of the advantages of the 2-arm voltage balanced capacitance bridge are shared by its 3-arm counterpart. The former is preferred for three reasons. Firstly, the most important parameter in dielectric measurements is the loss angle. (The loss tangent contains complete information about the form of the dielectric response, shows distinctive loss peaks rather than changes in gradient as for ϵ' and can normally be measured to a precision not easily reflected in measurements of ϵ'.) In the 3-arm bridge, there are two balance impedances whose ratio must be exactly known in order to compute the loss-angle; whereas in the 2-arm bridge, even if the balance capacitor value is not known or is in error, the loss-angle is determined directly from the drive voltages. Secondly, the triangular symmetry necessary for high frequency operation in the 3-arm bridge is more difficult to implement. Thirdly, if the balance capacitors are similar in each bridge arrangement, then the 3-arm bridge will be less sensitive because an extra loading will be seen at the balance point.

2.5 CONCLUDING REMARKS

An appropriate scheme for making VLF measurements must be d.c.-coupled and rely on lumped impedance techniques. The highest frequency at which lumped impedance techniques are appropriate depends on the spatial extent and symmetry of the arrangement.

Lumped impedance resonance methods are impractical below 10 Hz. Active current-to-voltage converters cannot be made to operate at the lumped impedance high frequency limit with readily available components. Lumped impedance bridges are unconditionally stable and potentially capable of higher frequency operation.

Balanced bridges have greater symmetry and are less prone to the effects of stray impedances than unbalanced bridges. Since capacitors are the only passive components which can be made truly wideband, and since dielectric samples are primarily capacitive, the optimum arrangement for measuring sample impedance is the voltage-balanced capacitor bridge. The 2-arm voltage-balanced capacitor bridge is potentially more sensitive and easier to construct than its 3-arm counterpart, and is thus the preferred central element of a subgigahertz dielectric spectrometer.

CHAPTER 3

Design Criteria And Operational Principles Of The Spectrometer

3.1 INTRODUCTION

In chapter 2 it was concluded that the optimum arrangement for a wideband lumped impedance dielectric spectrometer is the voltage balanced capacitance bridge. In this chapter, after adopting certain design criteria, the operational principles and electrical form of such a spectrometer are discussed. The development is traced from the basic sample bridge to a system comprised of three two-arm capacitance bridges; the sample, reference and standard bridges. These are shown in simplified overview in Figure 3.1. The reference bridge, consisting of two variable capacitors, C_5 and C_6, provides a means of checking signal phases. The standard bridge enables a comparison between the balance capacitor C_2 and a standard capacitor C_4.

3.2 DESIGN CRITERIA

The dielectric response of solids is known to cover enormous ranges of both temperature and frequency. These design specifications are therefore forced to be a compromise between the desire for greatest coverage and practical considerations.

The chosen operating temperature range is from -180 °C to 600 °C. The lower limit can just be reached by cooling with readily available liquid nitrogen. The upper limit is set conveniently below ordinary brazing temperatures and the onset of the serious degradation of workshop materials in air, whilst being sufficient to exceed the glass transition temperatures of most polymers.

The wideband potential of the balanced capacitor bridge has

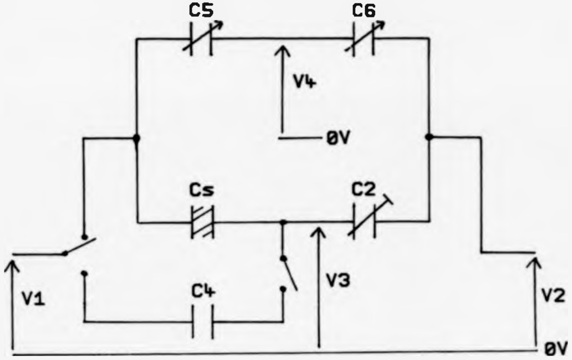

Sample Bridge : Cs and C2

Reference Bridge : C5 and C6

Standard Bridge : C2 and C4

Fig. 3.1

Basic 3-Bridge Arrangement of the Spectrometer been discussed in chapter 2. A frequency range of 10^{-5} Hz to 10^{8} Hz is proposed. The low frequency limit, corresponding to less than one cycle per day, is set by considerations of measurement time and system stability. Beyond the high frequency limit, which corresponds to a free space wavelength of 3m, distributive effects start to become significant.

A general precision of 0.1% in impedance and a loss tangent range of 10^{-3} to 10 are included in the specification; thereby permitting a wide range of moderately low to high loss materials to be studied.

3.3 THE SAMPLE BRIDGE

3.3.1 The bridge transfer function

Figure 3.2 shows the equivalent circuit of an ideal balanced capacitor bridge but with the detector input impedance represented by a capacitance C_3 and a parallel conductance G_3. The bridge transfer function, describing the behaviour of the detector input voltage V_3 in terms of the drive-arm voltages V and V(A+jB), may be written as:

$$V_3 = V\frac{((G_s-B\omega C_2)(G_s+G_3) + \omega^2(C_s+C_2+C_3)(C_s+AC_2) - j((G_s-B\omega C_2)\omega(C_s+C_2+C_3) + (G_s+G_3)\omega(C_s+AC_2)))}{(G_s+G_3)^2 + \omega^2(C_s+C_2+C_3)^2} \qquad (3.1)$$

The balance ($V_3=0$) occurs when: $A = -C_s/C_2$ and $B = G_s/\omega C_2$ as is the case without C_3 and G_3. By defining A_{bal} and B_{bal} as those values of A, B at balance and V_{3R} and V_{3I} as the real and imaginary components of V_3 respectively, then we may write:

$$V_{3R} = L_R(A_{bal}-A) + k_R(B_{bal}-B)$$

and

$$V_{3I} = L_I(A_{bal}-A) + k_I(B_{bal}-B)$$

where

$$L_R = \frac{-V.\ \omega^2\ C_2(C_s+C_2+C_3)}{(G_s+G_3)^2+\omega^2(C_s+C_2+C_3)^2}$$

and

$$k_R = \frac{-V.\ \omega\ C_2(G_s+G_3)}{(G_s+G_3)^2+\omega^2(C_s+C_2+C_3)^2}$$

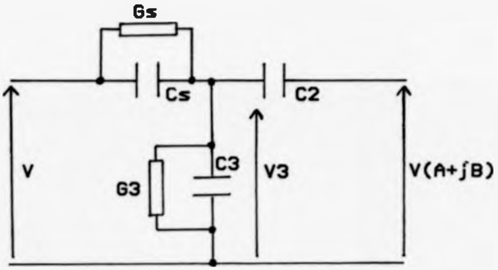

Fig. 3.2

Equivalent Circuit of Balanced Capacitor Bridge and $L_I = k_R$, $k_I = L_R$.

Thus for fixed V, V_{3R} and V_{3I} are described by simple linear equations in A and B. Consequently the component of V_3 at any phase ϕ may be described by an equation of the form:

$$V_{3\phi} = L_\phi(A_{bal}-A) + k_\phi(B_{bal}-B) \qquad (3.2)$$

This will be of importance both in the bridge balancing algorithm and the choice of detector. Since C_3 and G_3 occur as linear terms in the numerator of equation (3.1) and as squared terms in the denominator, the bridge sensitivity will fall with increasing detector input admittance. Hence C_3 and G_3 should be kept as small as possible and at most comparable with the sample and balance admittances.

3.3.2 The effect of arm feed impedances

The equivalent circuit for a practical implementation of the sample bridge is shown in Figure 3.3. The feed impedances $(R+j\omega L)$ represent a combination of the output impedances of the circuits acting as voltage sources in series with the series inductance and resistance of the connecting wires to the bridge. The capacitance C_g represents strays to ground at the bridge ends of the drive arms.

To examine the effect of the series feed impedance, we firstly assume that the values of L and R are the same in each arm and for simplicity ignore both C_g and G_s. In this case, at balance:

$$A + jB = \frac{-(R+j(\omega L-1/\omega C_2))}{(R+j(\omega L-1/\omega C_s))}$$

hence

$$A + jB = \frac{-(R+j(\omega L-1/\omega C_2))\ (R-j(\omega L-1/\omega C_s))}{R^2 + (\omega L-1/\omega C_s)^2}$$

from which, for R and L small compared to the bridge impedances

$$A \simeq \frac{C_s}{C_2} - \omega^2 L C_s \left\{1-\frac{C_s}{C_2}\right\} \qquad (3.3a)$$

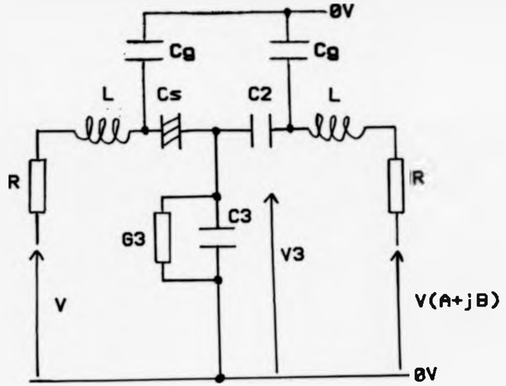

Fig. 3.3 Equivalent Circuit Showing Bridge Arm Feed Impedances

and

$$B \simeq - R\omega C_s \left\{1- \frac{C_s}{C_2}\right\} \qquad (3.3b)$$

Whereas for zero feed impedance $A = -C_s/C_2$ and $B = 0$. Thus for $C_s = C_2$ the effect of feed impedances is small. When the sample and balance impedances are not matched, then the error in each balance component is roughly proportional to the ratio of the relevant component of feed impedance to the sample impedance. It is therefore advisable to make the sample and balance impedances as similar as possible and to ensure that the series feed impedances are much smaller than the bridge impedances.

The effect of Cg may be slightly beneficial as the effective drive arm impedance, as seen by the sample and balance capacitor, will be reduced. If, however, the strays in each arm are not equal then a further error will be introduced.

3.3.3 Ground connections and feeder types

Hitherto, the representative of the 2-arm capacitor bridge has consisted of two voltage sources feeding through various impedances to the bridge drive arms whilst sharing a common ground with the detector. In reality, the ground connections will have a non-zero impedance and, since any net current flow through the sample and balance capacitors from one voltage source to the other must return through the ground connections, voltage differences will exist along these connections. Figure 3.4 illustrates the effect by showing ground connection impedances Zg_1, Zg_2 in addition to arm feed impedances Zf_1, Zf_2. A nominal ground has been chosen at the sample arm return. Balance occurs when the detector current through the impedances Zd is zero, that is when:

$$V2=-V1(C_s/C_2+j\omega C_s(Zf_2-Zg_2))/(1+j\omega C_s(Zf_1-Zg_1))$$

Departures from the ideal balance condition $V_2=-V_1(C_s/C_2)$ can

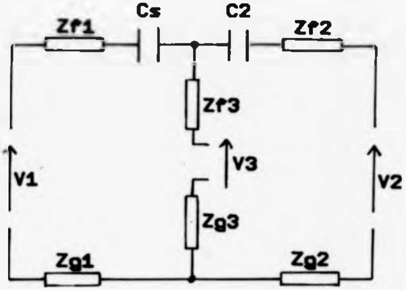

Fig. 3.4 Representation of 2-arm Capacitor Bridge Showing Feed and Ground Impedances

be minimised by taking the following steps. Firstly, the impedances Zf_1, Zf_2, Zg_1, Zg_2 should each be made much less than $1/j\omega C_s$. Secondly, by using a form of balanced feeder where $Zf_1 = Zg_1$ and $Zf_2 = Zg_2$. Thirdly, since for most measurements C_s/C_2 will be close to unity, the impedances $(Zf_2 - Zg_2)$ and $(Zf_1 - Zg_1)$ should be similar. Thus the bridge balance will be closest to the ideal when similar, low impedance, balanced feeders are used on both drive arms of the bridge. Care must also be taken to ensure that the detector feeder "ground" is taken at a point such that the symmetry between $(Zf_2 - Zg_2)$ and $(Zf_1 - Zg_1)$ is maintained. If the bridge is to be operated at high frequencies, a symmetrical arrangement of feeders and ground connections will ensure that the transit times due to each drive arm feeder are similar and that departures from the lumped approximation will be similar in equivalent impedances on either side of the bridge.

At high frequencies, the inductance of open feeder wires results in unacceptably high values of Zf_1, Zf_2, Zg_1, Zg_2. Low impedance feeders can be realised under such conditions by the use of transmission lines. Co-axial lines, which are commonly used in high accuracy bridges (see for example Kibble and Rayner (71)), give a number of advantages. By varying the radius ratio (b/a) of the inner and outer conductors, a range of characteristic impedances (Z_0) can be produced where:

$$Z_0 = \frac{1}{2\pi} \left(\frac{\mu}{\varepsilon}\right)^{\frac{1}{2}} \log_e \left(\frac{b}{a}\right)$$

Since the voltage on the outer conductor is likely to remain near ground potential at all frequencies, and since the outer surrounds the inner conductor, a good measure of electrical screening is afforded which reduces unwanted displacement coupling between feeders and from external sources. Outside the outer conductor, the magnetic field results from the sum of the currents flowing in the inner and outer conductors. If these are equal and opposite, then the resulting magnetic field is zero. Similarly, if the external circuit is so arranged that the currents flowing in inner and outer must be equal and opposite, inductive coupling from other sources will, in general, cause no net current change in the external circuit. Thus unwanted mutual inductance coupling between the bridge arms and from external sources can be reduced.

3.3.4 Choice of impedance values

In contrast to most lumped impedance dielectric techniques, which operate on samples with a capacitance $\geq$ 10 pF, a nominal sample capacitance of 3 pF has been adopted for the reasons discussed below. The sample is assumed to be primarily capacitative.

In order to qualify as lumped components, the sample, balance capacitor and their connections must be physically small compared to the smallest signal wavelength. In order to satisfy this requirement and to effect sample temperature variation, it is necessary to enclose both sample and balance capacitor in a variable temperature enclosure or sample cell. To isolate the bridge drive amplifiers, that is the voltage sources, and the detector amplifier from the temperature extremes of the sample cell, each can only be connected to the cell by a suitable length of feeder (see chapter 4 for more details).

The series impedance of the drive arm feeders and the output impedance of the bridge drive amplifiers together cannot easily be made less than about 5 Ω at 10^8 Hz. For reasons stated in the previous section, the sample impedance ought to be many times greater than this. A 3pF specimen at 10^8 Hz presents an impedance of 531 Ω.

The capacitance to ground due to the detector feeder, combined with stray capacitance to ground at the balance point and the input capacitance of the detector amplifier itself, are unlikely to total less than 5 pF. This corresponds to the capacitance C_3 in equation (3.1) suggesting that, if the sample capacitance is made much smaller than 5pF, then the bridge sensitivity would be seriously degraded.

Having chosen a working sample capacitance, the specification of the other bridge impedances can be considered more closely. In section 3.3.2 it was shown that errors introduced by feed impedances can be reduced by matching the balance and sample capacitances. The balance capacitance ought also to be less lossy than a sample with the lowest detectable loss angle (10^{-3} rads), at the lowest operating frequency, (10^{-5} Hz). Thus a balance capacitor of 3pF would require a parallel resistance somewhat greater than 5×10^{15} Ω. To avoid degradation of sensitivity with falling frequency, the resistive component of the detector input impedance ought to be of a similarly high value.

3.3.5 Consideration of sample arrangement

It was mentioned in chapter 2 that the voltage balanced 2-arm bridge can be used with either two or three-terminal samples. The latter having the advantage that the electrode edge capacitance, which is difficult to estimate accurately, does not appear significantly between the measurement electrodes and therefore in any direct calculation of sample permittivity. However, the design philosophy adopted is specifically for two-terminal samples. In this way, the impedance measuring performance of the prototype spectrometer could be assessed without additional complexity in the sample cell.

As a result of uncertainties in the effective sample area of a two-terminal sample, high accuracy measurements of sample permittivity cannot easily be made. Nevertheless, by designing the sample cell such that both stray capacitances across the sample and "access" or series capacitances between the electrodes and the unelectroded surface of the sample are minimised, the measured sample impedance will differ from the direct, or parallel-plate, impedance essentially by a scaling factor only and with no difference in tan δ. (If the sample has a high surface conductivity, however, problems will arise for which a three-terminal arrangement is the only practical way to restrict the effective sample area.) The application of the above points to the design of the actual sample cell is discussed in section 4.2.1.

To obtain true permittivity data over a frequency range, it will be necessary to normalise such data by comparing with either textbook data at a specific frequency, or by performing a separate single frequency measurement using apparatus capable of absolute accuracy. In the latter case a measurement of sample dimensions will normally be required.

In the absence of normalisation, the positions, in frequency and temperature, and the relative intensities of the measured loss processes within a material are unaltered. The relationships of section 1.4 still apply and can therefore be used to discriminate between conduction and relaxation processes. Although, for many applications, absolute permittivity is important, the usefulness of much of the published data of, for instance, Pratt and Smith (27)(29)(74), lies not in absolute quotations of permittivity, but rather in the broadband behaviour of loss processes at different temperatures and after various treatments.

3.4 THE GENERATION OF DRIVE-ARM SIGNALS

3.4.1 Introduction

The accuracy and range of the voltage-balanced bridge depends on an ability to generate signals of known amplitude and phase. Two separate schemes have been devised, the first covering the range of 15 kHz to 100 MHz and the second 10^{-5} Hz to 20 kHz.

3.4.2 High Frequency Systems

The principal components of the high frequency generation system are shown in Figure 3.5. Two variable frequency oscillators are phase-locked in quadrature. With the addition of a phase-splitter, signals at the relative phases of 0°, 90° and 180° are produced. The 0°, or reference phase, signal is connected through a variable attenuator into one input of a summing amplfier, or summer-driver, which feeds the sample arm of the bridge. The other two phases are also connected to variable attenuators; the outputs of which are summed in a second summer-driver feeding the balance arm. Thus if a_0, a_{90} and a_{180} are the respective amplitudes of the 0°, 90° and 180° components reaching the inputs of the summer-drivers, then the signal feeding the balance arm is:

$$V_2 = V_1\ (A+jB) = -g(a_{90}{}^2+a_{180}{}^2)^{\frac{1}{2}}\ \sin(\omega t-\arctan\ (a_{90}/a_{180})) \qquad (3.4)$$

where g is the summer-driver gain. For identical summer-drivers, the ratios A and B of the real and imaginary components to the sample

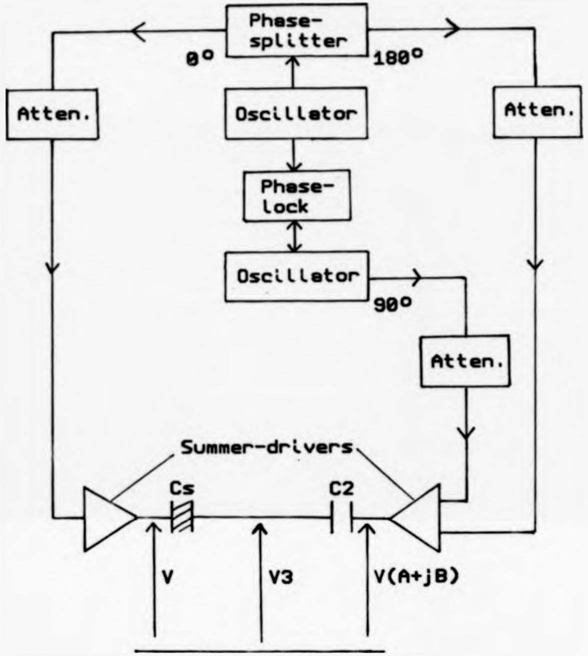

Fig 3.5 Generation Scheme for Bridge Drive Signals at High Frequency

drive amplitude will be simply

$$A = -\frac{a_{180}}{a_0} \qquad B = \frac{a_{90}}{a_0} \qquad (3.5)$$

Thus, by a suitable admixture of components, set by the attenuators, a wide range of amplitudes and phases can be constructed at the bridge arms.

In order to balance the bridge when the sample loss tangent is 10^{-3}, a_{90} would have to be 1000 times lower than a_{180}. To handle such losses, and allowing for impedance mismatches between sample and balance capacitor, the 90° attenuator ought to be capable of a division of at least several thousand. For loss tangents as high as 10 the 90° attenuator is set near to unity whilst the 180° attenuator would divide by approximately 10. In practice, with the effect of impedance mismatches, both the 0° and 180° attenuators ought to be capable of attenuations of at least 50. To guarantee a bridge balance to 0.1%, minimum increments of attenuation of a similar precision are required.

The lower frequency limit of 15 kHz is set at a convenient cross-over point between the high and low frequency systems. The method is extendable below this as long as oscillators can be made and phase-locked in quadrature.

3.4.3 Low Frequency System

The principal components of the low frequency generation system are shown in Figure 3.6. A digital clock circuit feeds a binary counter, the outputs of which address a block of Random Access Memory (RAM). Data lines from the RAM feed a pair of digital-to-analogue converters (DACs). By suitable programming of the data in the RAM, sinewaves, with the periodicity of the addressing sequence and of presettable amplitude and phase, can be produced at each DAC output.

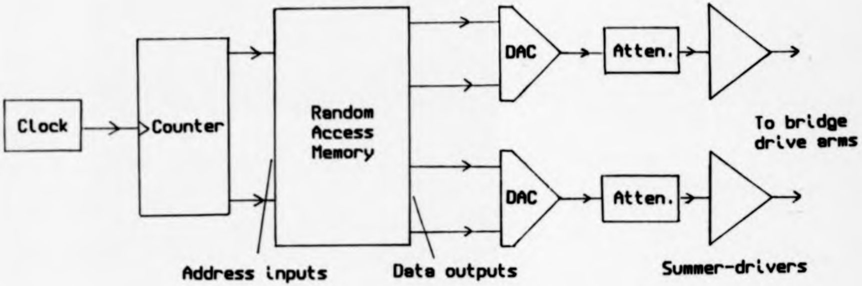

Fig. 3.6 **Low Frequency Waveform Generation Scheme**

The DAC outputs are then connected through variable attenuators, for coarse amplitude control, one to each summer driver. The attenuator range must be at least 10:1 to cater for impedance mismatches.

In order to achieve a bridge balance to 0.1%, both the relative amplitude and phase need to be programmable to at least that precision. To encode a waveform to 0.1% precision requires at least 10 bit (1024 steps) resolution. To adjust the phase of a 20kHz signal by 0.1% a time resolution of 50 ns is required.

Because the low frequency generator can be used, with suitable programming, to generate not only sinewaves but also other waveshapes, it is referred to as the Waveform Synthesiser.

3.5 THE REFERENCE BRIDGE

3.5.1 The principle of the reference bridge

At high frequency, all of the elements between the oscillators and the bridge, including the quadrature lock circuit, can introduce phase errors. At the higher output frequencies of the waveform synthesiser, significant phase errors can be introduced by the operational amplifiers and glitch filters associated with the DACs. In order to maintain accuracy steps must be taken to correct these errors.

The reference bridge consists of two variable, pure capacitances (loss tangent $<<10^{-3}$) electrically in parallel and spatially close to the sample bridge, (Figure 3.1). Because of the proximity of the reference bridge to the sample bridge, and because similar capacitance values and feeders are used, it is assumed that, if the phases of signals are correct at the reference bridge, then they will also be correct at the sample bridge. Since a pure capacitance bridge can only be balanced when the two arm drive signals are in exact antiphase, the reference bridge provides an independent means of discriminating phase misalignments, as is demonstrated in the following sections.

3.5.2 High frequency phase alignment

It is insufficient to merely detect phase errors, a means of correcting them must also be provided. At high frequency, therefore, small phase shifters are inserted into each of the three signal paths just before the attenuators. With the addition of on/off switches before each phase shifter, the following steps can be taken to ensure correct phasing at the reference bridge, and hence at the sample bridge.

(i) With the 90° source switched out, the desired amplitudes of the nominally 0° and 180° signals are fed to the summer-drivers.

(ii) The variable capacitors are adjusted to give a minimum reading at the output of the reference bridge detector.

(iii) If the minimum reading in (ii) is not zero then the relative phase of the signals is adjusted using the small phase shifters.

(iv) Steps (ii) and (iii) are repeated until the detector output is zero, at which point the drive signals must be in perfect phase opposition.

(v) The values of the two capacitors are noted and the nominally 90° signal is switched in at an appropriate amplitude.

(vi) The variable capacitors are again adjusted to give a minimum reading at the detector output.

(vii) If the capacitance values at this minimum are not the same as without the 90° component, then the phase of the 90° signal is adjusted.

(viii)Steps (vi) and (vii) are repeated until the minimum positions with and without the 90° signal are the same. The 90° signal now contains no in-phase component.

It will be noticed that the reference bridge is operated in steps (v)-(viii) in an unbalanced mode. In this case the detector input impedance is important; a non-capacitative input would cause a phase shift from drive arm to balance point, enabling even a perfectly phased 90° signal to interact with the other phases. In practice, the parallel resistance of the detector input ought to cause less than 10^{-3} rad phase shift at 20 kHz. With the variable capacitors set at 5 pF, and ignoring the beneficial effect, in this instance, of the detector input capacitance, a detector input resistance in excess of $10^9\ \Omega$ is required.

For quadrature signals greater than a few percent of the in-phase signals, a significant potentiometric error is inherent in steps (v) to (viii) above. Varying the capacitance ratio will affect directly the amplitude of the 90° component shifting the minimum position. This effect can be completely removed by replacing the steps (vi), (vii) and (viii) by the following.

(ix) For each new capacitance ratio, both the 0° and 180° signals are switched out, and the detector output due to the nominally 90° signal is measured. Then with all signals switched in, the detector output is read, from which the 90° only reading is subtracted. The capacitors are adjusted until this difference measurement is at a minimum. When the minimum occurs at the same position for just 0° and 180° signals, then the phasing is correct.

Thus the relative phases of all components can be correctly set at high frequencies.

3.5.3 Determination of high frequency amplitude ratios

For the determination of sample capacitance and resistance, it is not essential to know the exact amplitudes of the bridge drive components, but rather their relative values. With dissimilarities between the two oscillators, uncertainties in exact attenuation values and differences is summer-driver gain, as was the case with phase determination, the only meaningful measurements are at the bridge arms.

Determining the relative amplitudes of the 0° and 180° components is straightforward. In the phasing procedure described above, the reference bridge is balanced without the 90° signal. The required ratio is simply found from the capacitance ratio of the variable capacitors at balance.

To determine the relative amplitude of the 90° component, the following procedure may be adopted:

(i) With the 0° and 90° signals switched out, the detector output due to the 180° signal is recorded.

(ii) With the 0° and 180° signals switched out, the 90° attenuator is adjusted until the reference bridge detector reads the same as it did in step (i). The attenuator setting is recorded. The 90° signal magnitude at the summer-driver output is now the same as it was for the 180° signal.

(iii) With all signals switched out, the difference between the 90° attenuator setting in (ii) and that of the original unknown amplitude is compared by measurement at d.c. Thus the 90° amplitude can be compared directly to the 180° amplitude and, hence, to the 0° amplitude. No assumption is made of detector linearity, or otherwise, since identical amplitudes are used. An assumption is made that the attenuation ratio between the two settings of the 90° attenuator is the same at high frequencies as at d.c. This is expected to hold at least to 1% up to the highest frequencies, for most settings, provided GHz bandwidth attenuators are used.

3.5.4 Use with the Waveform Synthesiser

The waveform synthesiser has an in-built capability to make precise small or large changes in amplitude and phase. The need is therefore not for variability but for calibration. The reference bridge is used, at a given frequency, to provide a baseline correction for both amplitude ratio and phase.

A known capacitance ratio, usually unity, is set on the reference bridge and a balance is sought by varying the amplitudes and phases of the DAC output signals. At balance, the summer-driver outputs, derived from the DACs, must be in exact phase opposition and have the same amplitude ratio as the capacitance ratio set on the bridge: thus a baseline, for measurements on the sample bridge, is established.

Below about 100 Hz, a phase correction is not required. Instead of the above scheme, a d.c. measurement is made of the two DAC outputs to determine their amplitude ratio.

The baseline corrections described above are performed at high level, normally with the attenuation ratios between DAC and summer-drivers set to unity. If subsequent measurements on the sample bridge require changes in DAC outputs, then the DAC linearity is assumed to hold: this is reasonable as the effects of phase shift and attenuation, which the baseline correction is designed to correct, are due largely to amplitude independent roll-offs in filters and amplifiers. If the attenuators need to be changed, then a d.c. measurement is made of the actual attenuation, which, since high bandwidth components are used, is assumed to be the same for all frequencies below 20 kHz.

3.5.5 Determination of the capacitance ratio

Sections 3.5.3 and 3.5.4 assume that the capacitance ratio can be accurately known. This could be achieved by prior calibration or by assuming a position-capacitance law. The method adopted, however, is to balance the bridge at a convenient calibration frequency, and, from the amplitude ratio required for balance, to calculate the capacitance ratio. The calibration frequency must be one at which a d.c. measurement can be extrapolated to determine the exact amplitude ratio. By this method, day to day variations in capacitance can be accommodated and the need for a precise knowledge of capacitor position is obviated.

3.6 THE STANDARD BRIDGE

The calculation of sample capacitance and resistance clearly requires a value for the sample bridge balance capacitor. The balance capacitor is firstly variable by design, to match sample requirements, and secondly variable because it is placed in a variable temperature cell and therefore prone to expansion and contraction. In order to measure the balance capacitance, the configuration of Figure 3.7 is adopted, forming the standard bridge.

Through switch SW1, a standard capacitor C_4, situated outside the variable temperature cell, is connected to the balance point. By virtue of switch SW2, the waveform synthesiser output can be switched from the sample arm summer driver to another driver connected to the other terminal of C_4. Thus a bridge is formed between C_2 and C_4 which may be balanced, normally at the calibration frequency described in section 3.5.5, to determine the ratio C_2 C_4. If, therefore, the value of C_4 is known, the value of C_2 can be determined at any temperature.

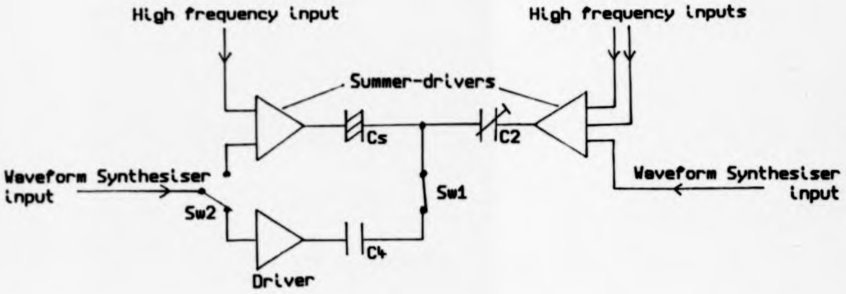

Fig 3.7 Configuration of the Standard Bridge

3.7 DETECTION

3.7.1 Null measurements

The minimum requirement of the detector of any balanced bridge is that it be capable of detecting a null. In practice, a reasonable dynamic range is essential in order to steer the balancing operation. With any wideband, high input impedance detector the input noise level is likely to exceed that of the balance signal. In order to distinguish the balance signal, some means of effectively narrowing the detector bandwidth about the signal frequency is required. Equation (3.2) shows that the balance signal, at any phase, is a linear function of the drive voltages. Although not essential, it would be beneficial to speed up the balancing operation by adopting a linear detector that is sensitive to phase.

The proposed scheme is shown in Figure 3.8. The balance signal is fed into an amplifier with a wide dynamic range, providing voltage gain, which in turn feeds one input each of a pair of two-input multipliers. The other multiplier inputs are fed by reference sinewaves each of amplitude A and at a frequency ω. One reference is at a phase ϕ and the other at a phase $90 + \phi$ with respect to the sample arm drive signal. If the balance signal, after amplification, has an amplitude a and a phase $\phi + \delta$ with respect to the sample arm drive signal, then the multiplier outputs M_ϕ and $M_{\phi+90}$ are given by:

$$M_\phi = Aa/2\ (\cos\delta - \cos(2\omega t + 2\phi + \delta))$$

$$(3.6)$$

$$M_{\phi+90} = Aa/2\ (\cos(2\omega t + 2\phi - \delta) - \sin\delta)$$

By integrating the multiplier output voltages over a time, which is long compared with the signal period or an integral number of half periods, the second harmonic terms can be removed leaving two d.c. outputs, in each case, linearly related to the balance signal

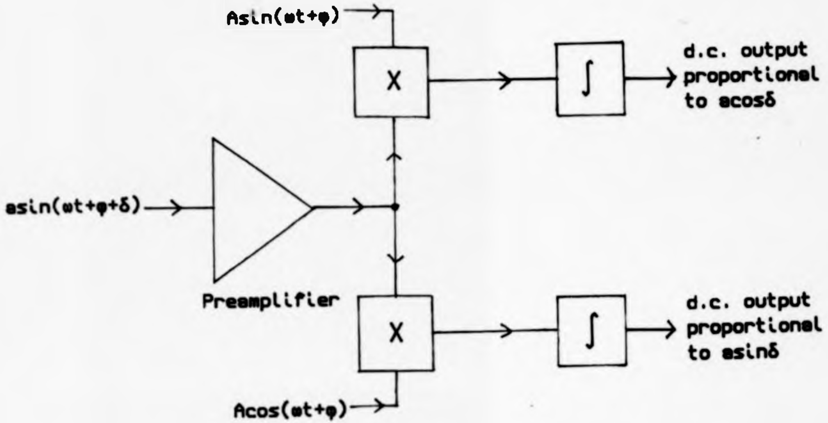

Fig 3.8 Correlation Detector

amplitude components at the phase of their respective references. Two multipliers are necessary to remove phase 'blind spots'. If noise is present at the multiplier inputs, then only those frequency components close to the reference frequency will cause low frequency or near d.c. terms in the output. In fact it can be shown, (for example Robinson (75)), that the effective noise bandwidth of a detector involving correlation with a reference signal is the same as the post-detection bandwidth. Thus the correlation scheme described is linear, works with small signals and can greatly improve the signal-to-noise ratio, whilst also giving phase information. In practice, the phase information will only give a rough indication as it will be difficult to ensure equal amplitude references in perfect quadrature.

For a balance precision of 0.1%, with bridge drive signals at a typical 1V r.m.s. amplitude, the minimum detectable signal ought to be about 1mV at the balance point. With impedance mismatches between the balance arms, bringing down the average level of drive signals, and the loss of signal by virtue of the detector input impedance, 100μV sensitivity would be more appropriate.

3.7.2 Off-null measurements

The reference bridge is operated both as a balanced bridge, where a detector of the type described above is appropriate, and as an unbalanced bridge. The reference bridge detector is also used to compare the magnitudes of 90° and 180° components. In the unbalanced and magnitude comparison modes, the signal levels are variable and generally much greater than in the balanced bridge situation. Detector linearity is not important in the unbalanced modes and phase sensitivity, especially when comparing magnitudes, is a positive disadvantage. For these reasons, a dual-detector scheme, as shown in Figure 3.9, is adopted for the reference bridge. A common gain stage

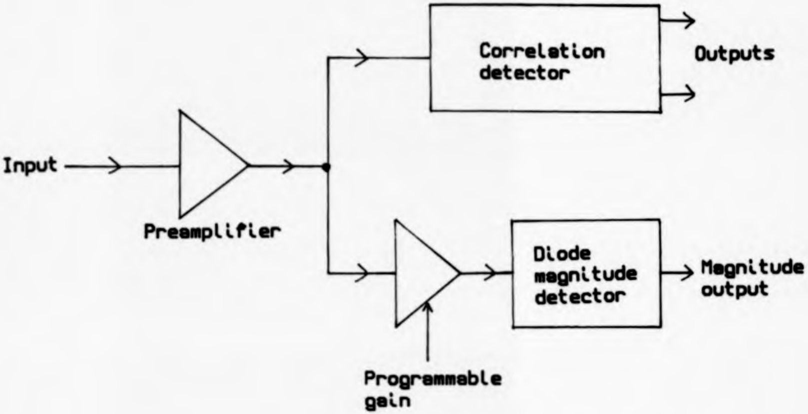

Fig 3.9 Dual Detector Scheme

feeds a correlation detector, as described in section 3.7.1, and a programmable gain stage which itself feeds a magnitude detector.

The simplest form of magnitude detector is used, based on the rectifying properties of a diode. If the signal voltage appears across a diode, then, for small signals ($\leq$ 300 mV), the average diode current will be approximately proportional to the mean square signal amplitude and for larger signals approximately proportional to the mean signal amplitude. The current in each case being nearly zero for half a cycle. By integrating the diode current, therefore, an output related to the signal magnitude can be obtained. If the input signal level is significantly greater than the noise level, as is most often the case in unbalanced measurements, then the diode current will be switched on and off by the signal and not by the noise. It can be shown that, in this case, similar reductions in effective input noise bandwidth and sensitivity to signal changes are obtained as with the correlation method: the signal effectively providing its own reference (see Robinson (75) or Wilmshurst (76)). In order to optimise the signal-to-noise performance, sufficient gain must be provided to ensure that the noise level before the diode exceeds its own noise and that the signal is strong enough to switch the diode efficiently, preferably in its linear region. To cater for wide range of input amplitudes, therefore, a programmable gain section is included.

3.8 DISCUSSION

3.8.1 Primary standards

The behaviour of most of the spectrometer components described so far is expected to remain reasonably constant during each single measurement. There are, however, behavioural aspects of some components which must always be constant; these requirements, or primary standards, are:

(i) The standard capacitor must have a fixed capacitative impedance at the calibration frequency.

(ii) The balance capacitor impedance must be frequency independent.

(iii) Signal phases at the reference bridge must be equivalent to those at the sample bridge.

(iv) The reference bridge capacitors must always be of the same impedance type, their ratio, once set, being frequency independent.

(v) The voltmeter used in the calibration and measurement procedures must be highly linear.

(vi) The waveform synthesiser DACs must be highly linear.

Special care is therefore paid to the construction of these components.

Accurate means of measuring temperature and frequency are also required.

3.8.2 Other sources of error

So far, only errors due to lack of resolution or stray impedances have been considered. Other potential sources of error are noise, harmonic distortion and signal pick-up.

The chief noise sources are the signal generators, the summer-drivers and the detector systems. Above 10kHz wideband noise results from a combination of Johnson noise, shot noise and extraneous interference. In view of the number of variables concerned it is difficult to predict rigorously a value, although a total r.m.s. noise voltage less than 10 $\mu V(H_z)^{-\frac{1}{2}}$ of detector input bandwidth is expected. Thus, with a coherent detector of output bandwidth 1Hz, there should be no difficulty in achieving the 100 μV sensitivity suggested in section 3.7.1. Below about 10 kHz, the noise level increases as a result of noise introduced by various control loops, although, as most of these will be associated with the high frequency oscillators, which will not be used at these frequencies, the effect is likely to be small. Potentially most serious is the occurrence of flicker noise. Since the flicker noise power in a transistor can be equivalent to that of the other noise sources in the device at a few kHz, and increases linearly with decreasing frequency, the probability of maintaining detector sensitivity at VLF, in the presence of such noise, is small. It is, therefore, essential that, in the design of every component operational at VLF, attempts are made to limit the presence and effects of flicker noise. The consequences of environmental noise, such as fluctuations in room temperature, can also be most serious at VLF, and must also be minimised.

Harmonic distortion in the drive signals may lead to unbalanced components at the balance point. Although coherence techniques make the detectors less sensitive to harmonics than the fundamental, the presence of distortion, like noise limits the amount of gain possible before detection.

Direct signal pick-up from generators to detectors is indistinguishable from bona fide balance signals and, therefore, has to be kept below the desired minimum detectable signal level.

3.8.3 Sample charging

Since the balance point of the sample bridge has a very high resistive impedance to earth, accumulation of charge from environmental sources or via injection from the summer-drivers can result. Two simple steps can be taken to reduce this:

(i) Maintain an average charge output of zero from the summer-drivers.

(ii) Provide a mechanism for discharging the balance point between measurements.

3.8.4 Overview

A more complete overview of the spectrometer is shown in Figure 3.10. The switch Sw3 enables a selection to be made between the standard capacitor and a short circuit for discharging the balance point. A d.c. monitor point, and charge control input are shown on the summer-drivers.

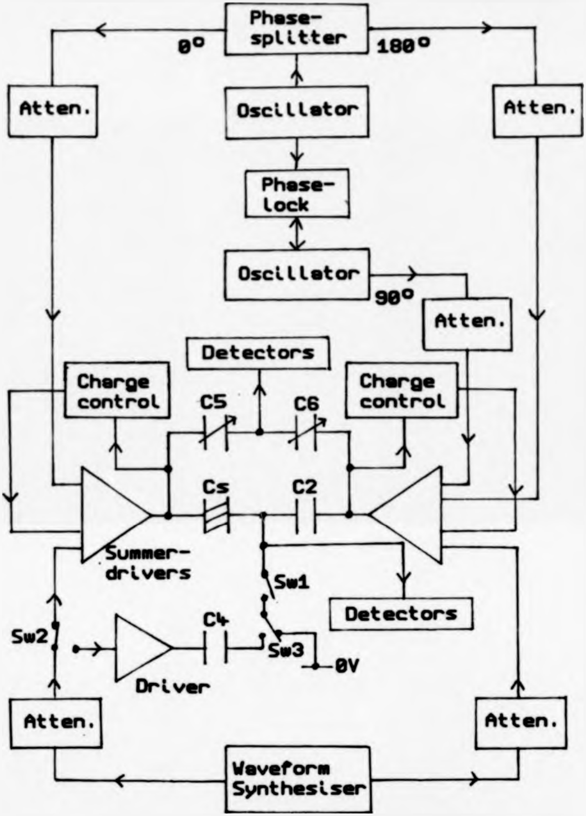

Fig. 3.10 Overview of the Spectrometer

CHAPTER 4

Practical Implementation of the Spectrometer

4.1 INTRODUCTION

This chapter describes the mechanical and electrical hardware used in the construction of the spectrometer. Beginning with the three bridges, the description moves outward to the generators and detectors and finally to the microcomputer interfacing. Space permits only a description of the salient features, rather than exact details of many of the components.

4.2 THE SAMPLE BRIDGE

4.2.1 Sample cell construction

In section 3.3.3 it was seen that the resistive components of both the sample bridge balance capacitor and the impedance between balance point and ground ought to be greater than 5×10^{15} Ω. Since conventional insulators either melt or contain too many activated charge carriers at 600 °C to be effective, dry air or nitrogen is chosen as the balance capacitor dielectric and both sample and balance capacitor are supported by a vacuum hold system.

The cell is bobbin-shaped, consisting of a hollow brass cylinder, 25 mm in length and 20mm in inner diameter, with top and bottom flanges for the screw-mounting of end-plates. A cross-sectional view through the cylindrical part is shown in Figure 4.1. Electrical access is provided by three short stainless steel co-axial feeders, the outers of which are brazed to the brass cylinder. The inner of the right hand feeder has a central vacuum duct which communicates with radial slots in the surface of the sample electrode, which protrudes from this inner, thereby holding

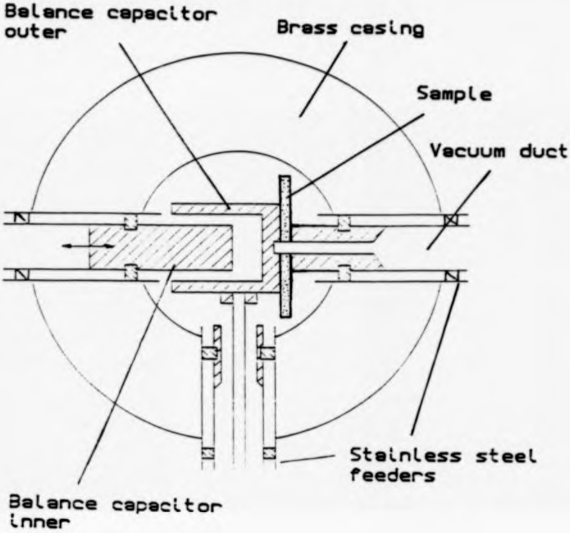

Fig. 4.1 Cross-section of sample cell

the sample in position. Through a small hole in the centre of the sample, the vacuum duct also communicates with radial slots in a flat surface closing one end of a hollow stainless steel cylinder, forming the outer of the balance capacitor. The inner of the balance capacitor is formed by an externally adjustable extension to the inner conductor of the left hand feeder. The inner of the third feeder is attached by a short screw thread to the outer cylinder of the balance capacitor, which is the bridge balance point, to provide a connection to the detector amplifier. The sample and balance arm feeders have a characteristic impedance of about 5 Ω, the inners being supported on ceramic rings. The detector feeder characteristic impedance is about 200 Ω. No inner support is provided except at the detector end which, being at room temperature, can be made to have a very high leakage resistance. A further steel tube is positioned between inner and outer to facilitate bootstrapping of the feeder capacitance at very low frequencies. The linear dimensions of the cell are less than one hundredth of the wavelength of the highest measurement frequency. The sample is approximately 14 mm x 20 mm and up to 2 mm thick.

It was stated in chapter 3 that, in its present form, the spectrometer is designed to measure the impedance of two-terminal samples, and that, at this stage, the absolute measurement of permittivity is not a primary concern. Nevertheless, the sample cell has been designed to minimise stray capacitive and fringing field effects, which might otherwise cause significant errors in loss tangent measurements.

The sample arm electrode diameter (6.35 mm) is smaller than that of the sample and the sample arm balance capacitor (10 mm), to ensure that any fringing field lines at the electrode outer edge pass mainly through the sample material. The outers of the stainless steel feeders are extended into the cell interior to reduce unwanted displacement coupling between electrodes. The extension of the sample arm inner feeder is adjustable, not only to account for different sample thicknesses, but also to enable positioning of the sample such that the outer of the sample arm feeder almost touches the sample surface, thereby reducing fringing fields due to the sides of the sample arm electrode. The hole in the sample, however, being up to 1 mm in diameter, and, therefore, about 2.5% of the sample arm electrode area, will lead to a loss tangent measurement reduced by a factor of similar magnitude, at all frequencies, if a correction is not made.

The benefits of coaxial feeders and symmetrical arrangements were mentioned in section 3.3.3. It was stated that the magnetic coupling to and from a coaxial feeder depended on the current balance between the inner and outer circuits. Ideally, at balance, the current flowing through the sample and balance capacitor, from one dirve arm inner to the other, is returned completely through the drive arm outers and the sample cell body.

The effect of mutual inductance coupling between the two drive arms is minimised by the use of extremely low impedance feeders. As a result of the inductance of alternative current return paths, the majority of the returned current is expected to flow through the outers of the 5 Ω feeders until the d.c. resistance becomes significant at frequencies below about 5 MHz. Any resultant voltage induced in the drive arms will be reduced significantly by the low feeder impedance in parallel with an impedance resulting from the drive amplifiers. Since, at balance, the current flowing through both drive arms is the same, any induced voltages in each arm will be of similar magnitude, and, in consequence, will be balanced out to the extent of the impedance matching between sample and balance capacitor.

A more serious problem could arise from mutual inductance coupling between both drive arms and the detector circuitry. The effect is reduced, as above, by the use of a coaxial detector feeder. Most importantly, the detector feeder is positioned orthogonally with respect to the other feeders, thereby preventing direct magnetic field interaction, and for reasons of symmetry.

In order to control the atmosphere, two additional 5mm diameter steel tubes (not shown) feed into the cell bisecting the angles between the detector and drive arm feeders. Two turns of copper pipe are wrapped around and brazed onto the outside of the cell through which hot or cold gas can be passed for temperature variation. Thermocouples are attached to the end plates.

The cell is supported, through its various feeders, by an outer brass casing. This can be seen in Figure 4.2 with the lid removed to show the sample cell. The mountings are arranged so as to move freely in radial directions to cater for expansion and contraction. The outer walls are maintained at approximately 35 °C by water pumped through circular copper pipes soldered into grooves at the top and bottom of the casing. Convection in the space between the sample cell and the outer casing is reduced by loosely-packed glass wool.

4.2.2 Temperature control system

A schematic diagram of the gas flow temperature control system is shown in Figure 4.3. The gas flow is derived from a dewar containing liquid nitrogen. A Eurotherm 818S three-term controller, (not shown), adjusts the power input to a heating coil in the dewar to maintain a preset boil-off pressure. A system of pipes, including

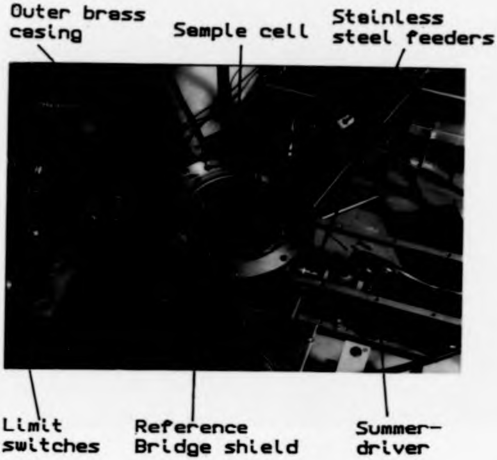

Fig. 4.2 View of Sample Cell and Surrounding Structure

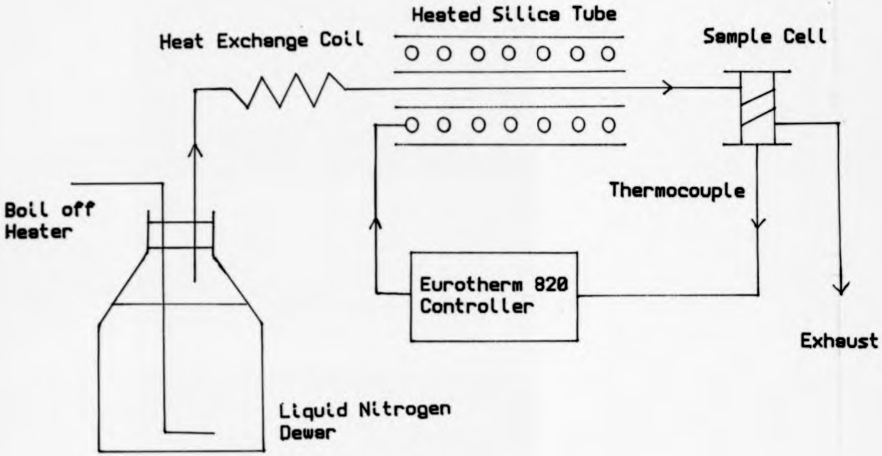

Fig. 4.3 Temperature Control Scheme

a pressure sensor and relief valve and various taps (not shown), connects to a heat exchange coil which may be used to pre-heat or cool the nitrogen. The gas then flows through the inner of a co-axial pair of silica tubes, about 800 mm in length, between which a nichrome wire heating element is wound, the whole unit being insulated and then enclosed circumferentially by a brass cylinder. The connections to the silica tube, approximately 10 mm in diameter, are made using spring loaded butt-joints and in-line bellows to allow for expansion and contraction. The pipework connecting to the sample cell is heavily insulated. The final stainless steel tube is surrounded by an evacuated jacket as it passes through the water-cooled brass casing, before joining the copper pipe wrapped around the cell. Although more energy may be passed through the copper coil surrounding the cell at high rates of gas flow, the efficiency of heat transfer is reduced by the shortened interaction time. Thus the sample temperature depends relatively weakly on the flow rate.

A Eurotherm 820 three-term controller monitors the output of a thermocouple at the sample cell and adjusts appropriately the power to the heating element. The demand temperature and boil-off pressure are programmed via bidirectional serial links from the system microcomputer.

4.3 REFERENCE BRIDGE

Air is also chosen as the dielectric for the reference bridge. The drive electrodes consist of brass cylinders, of about 10.6mm outer diameter, moveable along the axis of an outer brass cylinder which is 58 mm in length and 15mm in inner diameter. A cross-section is shown in Figure 4.4. A short wire connected to a point on the circumference of the outer cylinder and halfway along its length feeds the input to the detector amplifier. The outer cylinder is

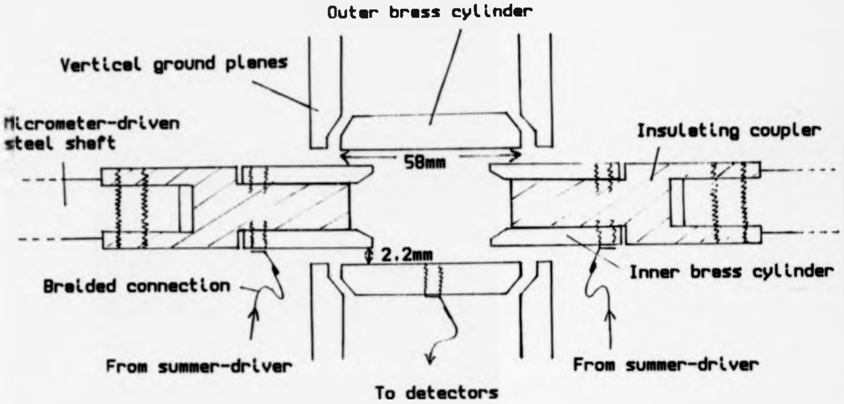

Fig. 4.4 Cross-Section of Reference Bridge

mounted on PTFE supports at either end. The inner cylinders are attached to a steel shaft, via an insulating coupler, which is mounted on two linear bearings and is spring loaded. A steel ball set in the end of each shaft mates with a flat-ended micrometer-head which pushes the shaft, working against the spring loading. Each micrometer-head has a 25 mm throw in 50 turns and is driven by a 1.8° stepper motor giving 10^4 programmable positions. A plate attached to each steel shaft actuates limit switches, see Figure 4.2, providing coarse positional information to the controlling circuitry. A further cam, on a drive wheel connected to the stepper motor shaft, closes a switch once per revolution at a precise motor position. Once in position, the stepper motors can be locked by simultaneously activating all of the windings.

The whole mechanism is mounted close to the sample cell casing and on the same aluminium baseplate. Shielding plates are fitted around the reference bridge as can be seen in Figure 4.1. Coupling from the summer-drivers is firstly through 5 Ω feeders (similar to those on the sample bridge), and then by short lengths of braid, to allow for movement.

A capacitance ratio of about 10:1 can be achieved. The maximum capacitance between an inner and the outer is about 5 pF.

4.4 STANDARD BRIDGE

Figure 4.5 shows the housing of the sample bridge detector head amplifier, which, like those of the summer-drivers, is an earthed brass box which butts up against the sample cell outer casing. The inner conductor of the detector feeder extends into the box until it rests on the cylindrical perspex support shown. At the sample cell end of the box, the conductor passes between the two spring-loaded jaws of a solenoid operated switch, which can contact the conductor without displacing it. Wires from each jaw feed the

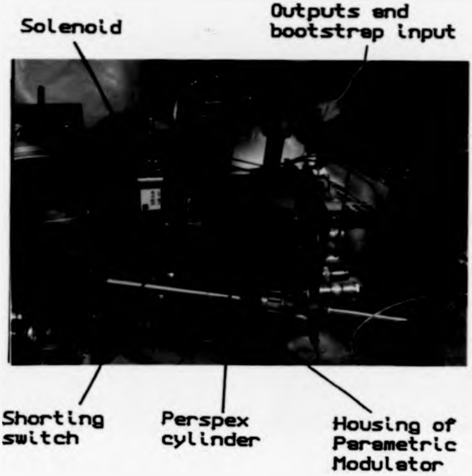

Fig. 4.5 Side View of Sample Bridge Detector Head Amplifier Housing

common contact of a changeover relay. The relay selects between a 100 Ω resistance to ground, for discharging the balance point, and one side of the standard capacitor. The relay and capacitor, which are not shown, fit into the space immediately in front of the switch. A commercial 3.3 pF silver mica capacitor is used. Since, at the calibration frequency (175 Hz) the impedance of the bridge is high, the other terminal of the standard capacitor is driven simply by a 50 Ω termination across the signal feeder. The circuit is shown in figure 4.6.

4.5 THE HIGH FREQUENCY SIGNAL GENERATORS

4.5.1 Oscillators

The oscillators are based on the circuit of Figure 4.7. Two high current VMOS transistors are connected as source followers; the first is biased in its most linear region. The second transistor is biased such that, with increasing source voltage, there is an increasing encroachment of the pinch-off region; thereby causing a gentle monotonic fall in gain with increasing signal amplitude. The variable attenuator network provides positive feedback into a tap on the inductor of the parallel tuned circuit, the inductor acting as an autotransformer providing the voltage gain.

Thus the fast non-linearity, essential for stable oscillations, (Robinson (75)) is provided by the second stage, whilst the first stage simply buffers the relatively undistorted output of the resonant circuit. The oscillators are operated at high level (± 8 V) providing a good signal-to-noise ratio. Long term stability is provided by an integrating loop, which measures the output of a temperature-stabilised, self-coherent amplitude detector and sets appropriately the gain of the attenuator network. Below 10 MHz, attenuation is provided by a VMOS transistor at the stem of a resistive-T network. For other frequencies, a PIN diode network is

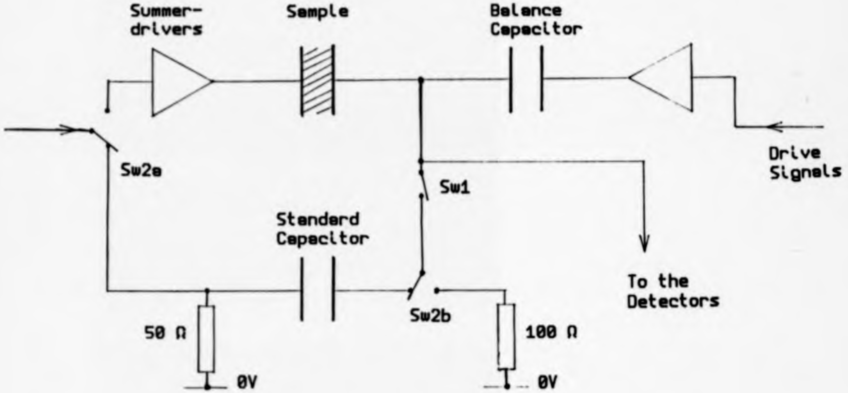

Fig. 4.6 Connection of the Standard Bridge

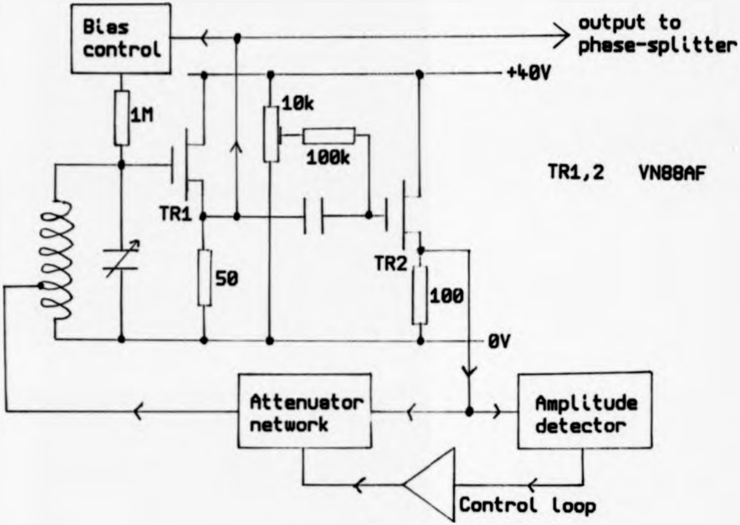

Fig. 4.7 Basic Oscillator Circuit

used except at frequencies around 100MHz, where instead, the non-linearity of the second stage is adjusted, which has less of an effect on the oscillation frequency than impedance variation.

Relays enable the selection of one of seven inductors for the resonant circuit. Further frequency variation is effected by varying the tuning capacitor in three ways; by adjusting the reverse voltage across a varicap diode, loosely coupled to the tuned circuit to avoid excessive non-linearity, by a motorised 150 pF air-spaced variable capacitor, and by switching the elements of a binary-scaled bank of polystyrene capacitors.

The tuned circuit configuration used around 100 MHz has a slight deviation, as shown in figure 4.8. An approximately quarter-wave length of miniature 50 Ω co-ax is connected across a tuned circuit normally resonant below 90 MHz. If the line were left open-circuited then its impedance at the tuned circuit would be given by:

$$Z_{line} = -j\, Z_0 \cot(2\pi l/\lambda) \qquad (4.1)$$

(see Bleaney and Bleaney (70)), where Z_0 = 50 Ω and l is the length. For l greater than a quarter wavelength then Z_{line} is inductive and increases with line length until a half-wavelength is reached. Thus the inductance of the tuned circuit is reduced and hence its resonant frequency is increased. From equation (4.1) an open-circuited line less than a quarter wavelength long looks capacitive; similarly a capacitive termination can look like an extra length of open-circuited line. By terminating the 50 Ω line with the 150 pF variable capacitor, the effective line length can be varied almost to a half- wavelength. Thus the effective inductance of the tuned circuit can be varied remotely. An enhanced selectivity is obtained over a normal parallel tuned circuit, since, in moving off resonance,

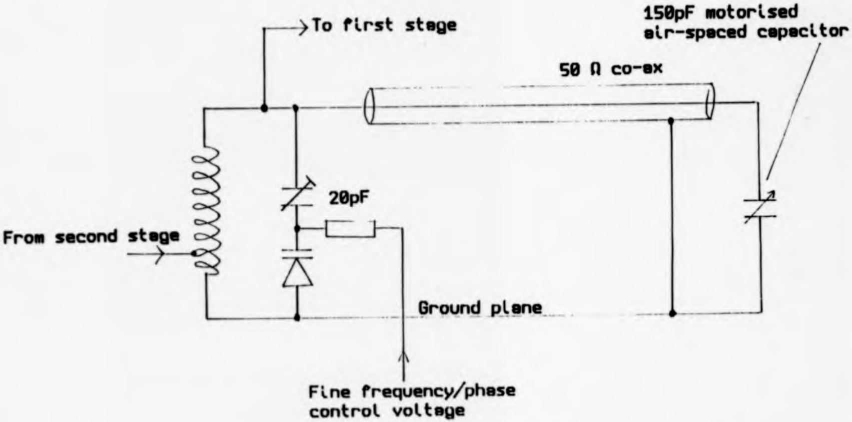

Fig. 4.8 100MHz Oscillator Tuned Circuit Configuration

the inductance changes, due to a wavelength change, to further de-tune the circuit. The arrangement adopted provides tuning from 110 MHz to 80 MHz.

The oscillators are built on aluminium baseplates, to the layout shown in Figure 4.9. Three upright sections help to define the feedback path and provide heat sinking.

4.5.2 Frequency counter

An output from the second stage of each oscillator drives one input of a 2-channel frequency counter. A transistor limiter on each input feeds both a direct TTL interface and an ECL divide-by-100 integrated circuit with a TTL compatible output. Further TTL gating and dividers provide appropriate frequency division before feeding a 4-digit decimal counter chip which interfaces with both a LED display and the system microcomputer. The counter period is provided by a programmable crystal oscillator. Maximum resolution is one part in 9999.

4.5.3 Quadrature-lock unit

The quadrature-lock unit consists of a temperature-stabilised phase detector, shown in Figure 4.10, which feeds a control loop reacting upon the tuning varicap of the 90° oscillator.

The circuit of the phase detector is shown in Figure 4.11. An output from the 0° oscillator switches the upper pair of transistors in the long tail arrangement. The quadrature oscillator controls the current-source tail. When the oscillator frequencies are close, the difference between the two collector voltages is proportional to the cosine of the phase angle between the two outputs. The quadrature input can be switched out and a 12-bit DAC adjusted to zero the detector. Small phase shifts, largely independent of frequency, can then be made by offsetting the DAC.

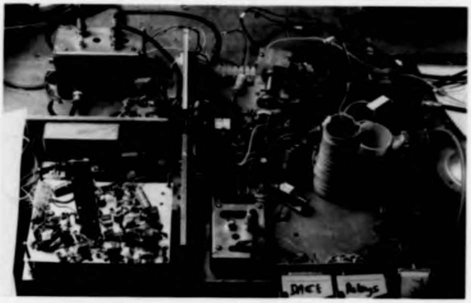

Fig. 4.9 Photograph Showing Oscillator Layout

Fig. 4.10 Photograph Showing Quadrature Phase Detector

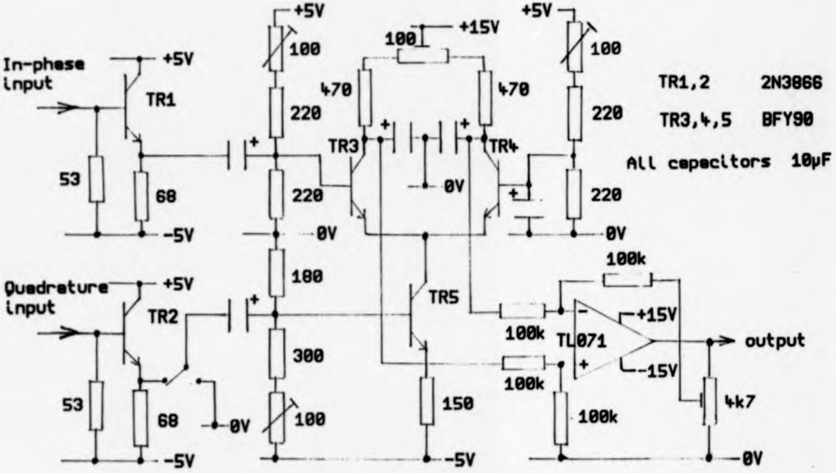

Fig. 4.11 Quadrature Phase Detector

The control loop is integrating, with switchable gain to cater for the wide range of loop conditions between 15 kHz and 100 MHz.

4.5.4 Phase splitters

Although only one phase splitter is strictly necessary, for reasons of symmetry, one is fitted to each oscillator. The unit can be seen in the left foreground of Figure 4.9.

The circuit diagram is shown in Figure 4.12. A conventional, unity gain bipolar phase splitter stage (TR1) feeds two follower pairs, each providing low impedance outputs. The output amplitudes are controlled by integrating loops, fed by diode peak detectors on each output and operating on the attenuator networks formed by TR4 and TR5. Further loops maintain the d.c. outputs at zero. Small differential phase-shifts are provided by the varicap diode. An extra wire loop between the non-inverting output of the splitter stage and the first of its followers (TR3) counter-balances the base-collector transit time of TR1.

4.5.5 Delay lines

A binary-scaled, relay-switched bank of five co-axial lengths provides delays of up to 2 ns. An off switch is also included to re-direct the oscillator outputs to a dummy load. A number of small capacitors, with one lead grounded locally, are used to 'pad' the switches to minimise impedance discontinuities.

4.5.6 Attenuators

For simplicity, identical attenuators are used for the three primary phases. Three Wavetek 5000 series turret attenuators per channel provide attenuation up to 80 dB in 0.1 dB steps. Each turret is driven through a 10:1 reduction gearbox by a 7.5° stepper motor.

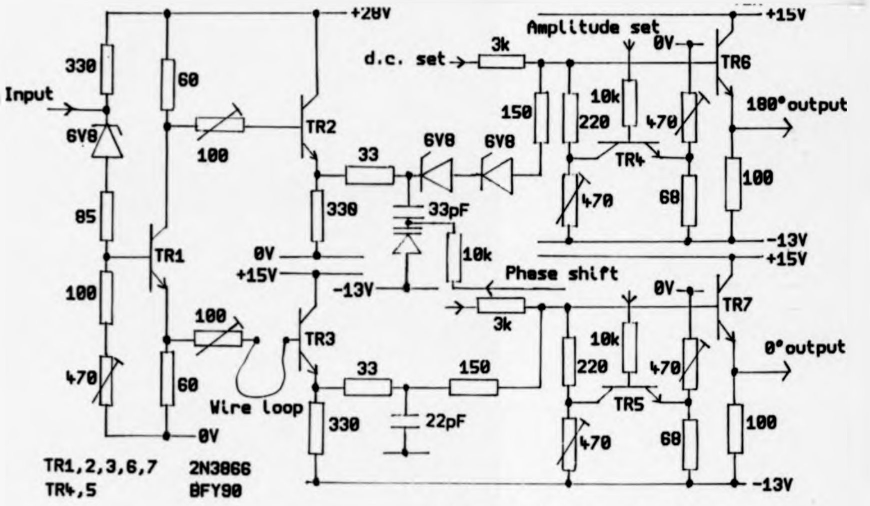

Fig. 4.12 Phase-Splitter

4.6 LOW FREQUENCY SIGNAL GENERATORS

4.6.1 Waveform Synthesiser

Although the principles are simple, the waveform synthesiser circuitry is complex through repetition, involving in excess of 150 integrated circuits. The Synthesiser is housed in two perspex boxes; the first, shown in Figure 4.13, contains the timing and RAM boards and two complementary output 8-bit DACs, whilst the second, shown in Figure 4.14, contains three 12-bit DACs.

A circuit plan is shown in Figure 4.15. A suitable clock frequency, between 1 Hz and 20 MHz and derived from a 20 MHz crystal oscillator, is selected through the programmable divide-by-n counter. The clock then feeds a synchronous divide-by-20 counter which has four outputs α,β,γ and ϕ. By latching 5-digit codes, each of α,β and γ can be programmed to be low for any one only of the twenty states of the counter. ϕ, which is low only if the count is below sixteen, is used to clock a 12-bit programmable stop and start counter, which simultaneously addresses three banks of RAM each 2K x 16 bits. The RAM data outputs from the previous clock cycle are latched by the same edge of ϕ as clocks the counter, and then again at the 12-bit DAC inputs by either α,β or γ. By this means, although the RAM and DACs are never accessed more frequently than once per microsecond, a time resolution twenty times smaller, that is 50 nS, can be achieved. Not shown is an additional uncalibrated phase adjustment in which 0, 1, 2 or 3 further gate delays of nominally 12 nS can be interposed in each of the α,β and γ channels for ultra-fine time (phase) shifts.

The upper fourteen bits of data are allocated for signal encoding, although, at present, only twelve are used, providing an adequate 4096 levels. The two least significant bits are reserved as 'EVENT' lines and are used to trigger the detectors. The central

Fig. 4.13 Photograph Showing Waveform Synthesiser RAM and Timing Boards

Fig. 4.14 Photograph Showing Waveform Synthesiser 12-Bit DACs

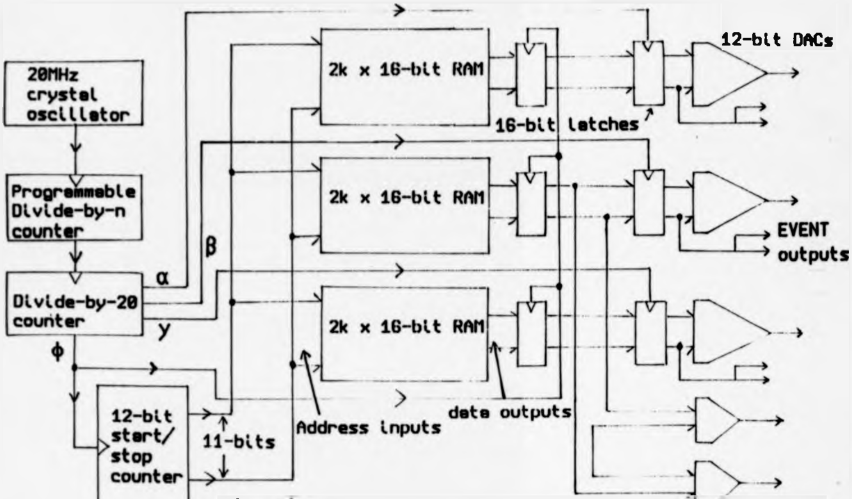

Fig. 4.15 Plan of Waveform Synthesiser

data channel can be used either to feed a 12-bit DAC or two 8-bit DACs. In the latter case, which is normal, the 8-bit DACs provide an orthogonal pair of sinewaves to feed the detector correlators.

Separate buses, not shown, permit computer access to the RAM (as 12K x 8 bits) and to all the timing latches. The generator can be turned on synchronously and off both synchronously and asynchronously with respect to the sample drive EVENT lines. Thus integral numbers of cycles can be ensured at the summer-drivers, rather than part cycles, to avoid sample charging.

The 12-bit DAC circuits are primary reference components, therefore special precautions were taken in their design. All of the 12-bit DACs share the same voltage reference, so that any fluctuations in the reference voltage does not affect the output voltage ratios. The wideband op-amps used with the DACs have a small voltage offset and output noise. To minimise the effect of these and other noise sources, the waveforms are generated at high voltage (± 8V) then resistively divided to feed a 50Ω load. Passive glitch filters are included ($\tau \approx 1\ \mu s$). The perspex box containing the DACs is sealed against dust and draught and is temperature stabilised.

4.6.2 Low frequency attenuators

The low frequency attenuators are constructed from binary-scaled series of relay-switched π-networks, each presenting 50 Ω. Up to 63 dB is provided in 1 dB steps. Since the reference, or no attenuation, condition is most important, an extra relay is included to bypass all of the networks. High stability metal film resistors are used. Each complete unit is shielded in a metal case.

4.7 SUMMER-DRIVERS

The basic summer-driver circuit is shown in Figure 4.16. The emitter of TR5 is an a.c. virtual earth into which are summed the currents from four current sources controlled by the signal inputs.

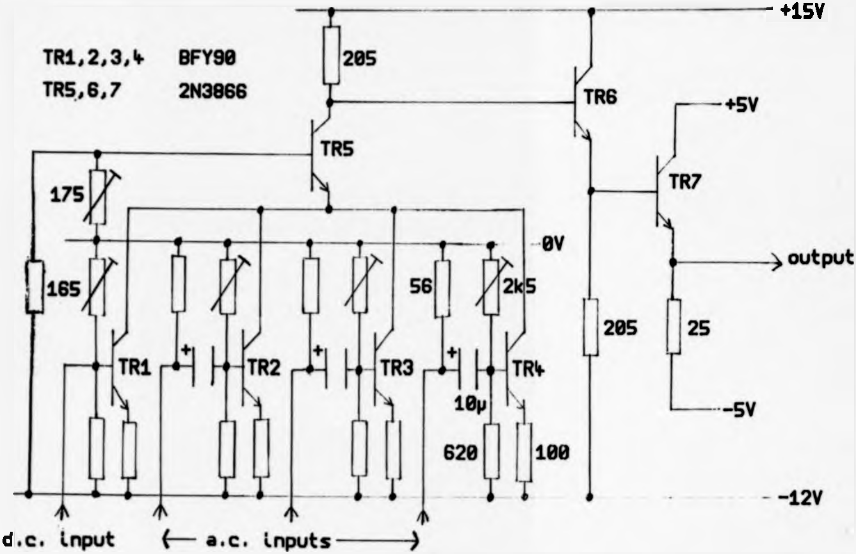

Fig. 4.16 Basic Summer-driver

Since most of the emitter current of TR5 flows in the collector circuit, the collector voltage is closely proportional to the sum of the input signal voltages. The voltage gain from any input to this point is about 2.7 and inverting. Interchannel cross-coupling is especially reduced since the summation point voltage is almost stationary and the output current compliance of the current sources is high. Extraneous cross-coupling is minimised by mounting the current sources on a semi-circular copper clad board. The main conduction paths between the inputs are then restricted by cutting radial slots in the grounded copper surface. The transistor screens are also grounded. Two successive follower stages together provide an output impedance of less than 3 Ω at all frequencies. Three of the inputs are a.c. coupled, the fourth being for VLF and d.c. charge control signals. The amplitude response from input to output is flat to about 105 MHz.

The basic summer-drivers are mounted inside brass boxes as can be seen in Figure 4.17. The outputs feed through braided connections to the sample and reference bridge feeders. The input signals enter through BNC connectors at the bottom of the end-plate, beneath various monitor outputs.

A more complete plan of the summer-driver system is shown in Figure 4.18. The oscillators connect directly to the current source inputs, whilst LF, VLF and charge control signals are summed beforehand using remote op-amps. There are two modes of operation. Above 500 Hz, a time constant on the final output provides a measure of the average d.c. level, a suitable d.c. correction signal is then summed with the signal. At 500 Hz and below, the basic summer-driver becomes part of a unity gain but heavily fed-back amplifier, the output reproducing the LF or VLF input, which have low d.c.-offsets. The mode is selected using relays.

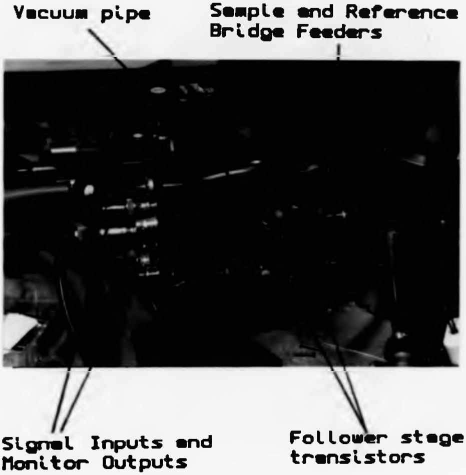

Fig. 4.17 Side View of Sample Arm Summer-Driver Housing

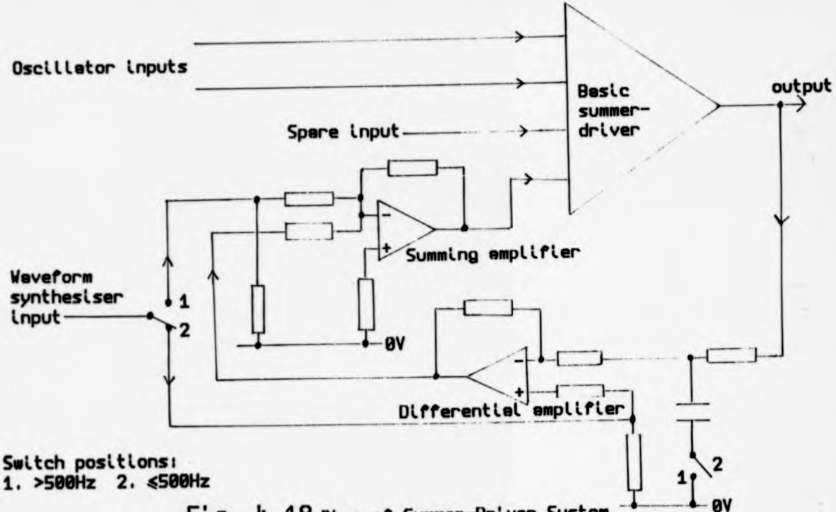

Switch positions:
1. >500Hz 2. ≤500Hz

Fig. 4.18 Plan of Summer-Driver System

4.8 THE DETECTOR SYSTEM

4.81 Introduction

The detectors may be sub-divided into four sections; the wideband head amplifier, the high frequency detectors, the medium frequency detectors and the VLF detection system. Care has been taken to avoid ground loops between different detector modules through the use of balanced or coaxial interconnects and copious supply line decoupling.

4.8.2 Wideband head amplifier

Figure 4.19 is a circuit diagram of the sample bridge detector head amplifier; that part within the dashed box represents the somewhat simpler reference bridge head amplifier.

A high frequency enhancement MOSFET, connected as a source follower, drives a bipolar current source tail. An emitter follower provides both 50 Ω and filtered outputs. Using a high load resistance, the gain of a source follower can be made near to unity; a gain of about 0.9 is achieved, however, even with an active load, because of the loading effect of the output stage combined with the finite drain resistance. The amplitude response of the circuit falls by 3 dB at about 100 MHz.

At the reference bridge, the bootstrapped 10^{10} Ω resistor on the MOSFET gate appears at the balance point, satisfying the design requirements of section 3.5.2. Since the sample bridge is used at VLF, the additional components are required. The variable capacitor C_7 acts at VLF as a parametric converter, transforming slowly changing signals, by capacitance variation and hence through charge conservation, into an amplitude modulated voltage at the frequency of the capacitance variation. The construction of C_7 is shown in Figure 4.20. The inner of the balance point detector feeder is supported on

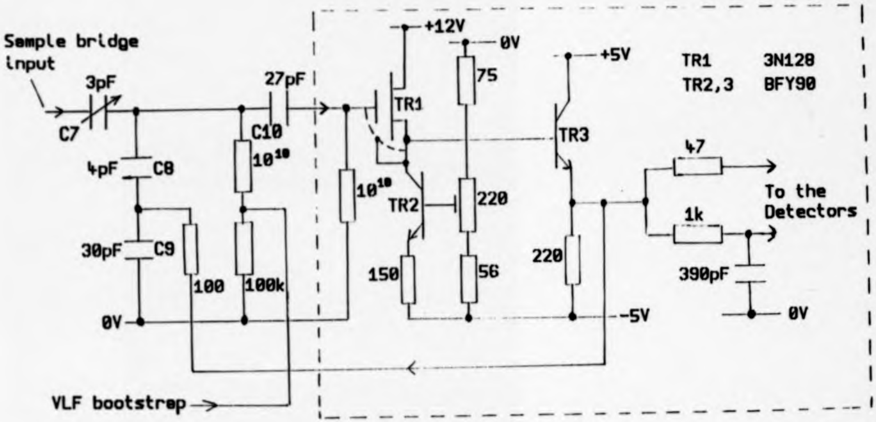

Fig. 4.19 Wideband Head Amplifier

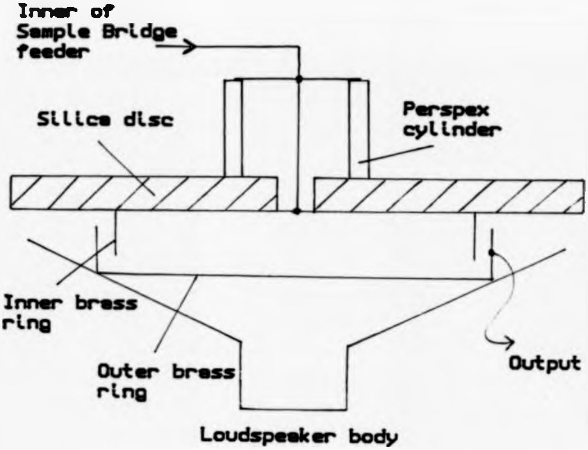

Fig. 4.20 Parametric Modulator

a perspex cylinder, itself mounted on a silica disc, which together provide the high d.c. input resistance (> $5 \times 10^{15}\Omega$) required. A small wire connects the inner through a hole in the silica disc to a brass ring fixed to the underside of the disc; this forms the input plate of C_7. The other plate consists of a slightly larger brass ring mounted on the cone of a small loudspeaker. By applying a signal to the loudspeaker coil, preferably near its mechanical resonance (≈ 220 Hz), the capacitance can be modulated at the excitation frequency as the degree of overlap between the brass rings is changed. Leads from the outer ring connect to the head amplifier via the coupling capacitor C_{10}. The capacitance C_8 represents the strays from the outer brass ring to the loudspeaker body, which has a capacitance C_9 to ground by virtue of its mounting. The loudspeaker body is driven through the 100 Ω resistor, to reduce the effect of C_8 and C_9 by bootstrapping, at all but the highest frequencies. The resistor R_1 provides a connection for a VLF bootstrap which is described in section 4.8.5. The inclusion of the polystyrene coupling capacitor C_{10} has two important effects. Firstly, since the head amplifier is not used directly for VLF, it provides a d.c. break. This is especially important, if, for whatever reason, the balance point has charged up to a voltage beyond the dynamic capability of the amplifier. Secondly, the picoamp leakage current in the MOSFET varies exponentially with temperature, causing mV changes on the gate, which would otherwise significantly back-react on the modulated capacitor causing VLF noise.

The loudpeaker and other components of the modulator are mounted inside the same box as the head amplifier, as can be seen in Figure 4.5.

4.8.3 High frequency detectors

The high frequency detectors are always used in conjunction with the oscillators, i.e. 15 kHz – 100 MHz. A block diagram is shown in Figure 4.21. A co-axial relay selecting switch between the reference and sample bridge head amplifiers saves much duplication.

A signal from the 50 Ω output of the selected head amplifier is received into 50 Ω and amplified by a commercial low-noise wideband amplifier. Two more such amplifiers follow, providing a total gain of about 250, before feeding a pair of double-balanced modulators. A pair of nominally orthogonal reference signals also feed the modulators. The outputs are filtered, using a one second time constant, to separate the d.c. components. Diode magnitude detectors are positioned at the output of each amplifying stage, allowing a choice of gain for optimum performance.

The detectors are built on ground planes in a shielded box which is positioned close to the head amplifiers to minise pick-up.

4.8.4 Low frequency detectors

The low frequency detector scheme is shown in Figure 4.22. High pass filters block any components below about 0.1 Hz fed from the filtered outputs of the two head amplifiers. Wideband op-amps provide an initial gain of about 25. Since the rest of the system is d.c.-coupled, these first stages are temperature stabilised to minimise offset drifts. An analogue switch unit enables the selection of either head amplifier, the demodulated VLF balance signal or ground, as a reference. After an optional gain boost stage, the selected signal feeds a pair of orthogonal correlators, constructed using temperature-stabilised four-quadrant multipliers. Op-amp integrators follow, their inputs gated and controlled by a programmable counter clocked by a once-per-cycle EVENT from the waveform synthesiser. Thus the gate can be opened, and, after a predetermined number of cycles, closed, leaving a steady d.c. output, bereft of troublesome second harmonics, which can be read at leisure.

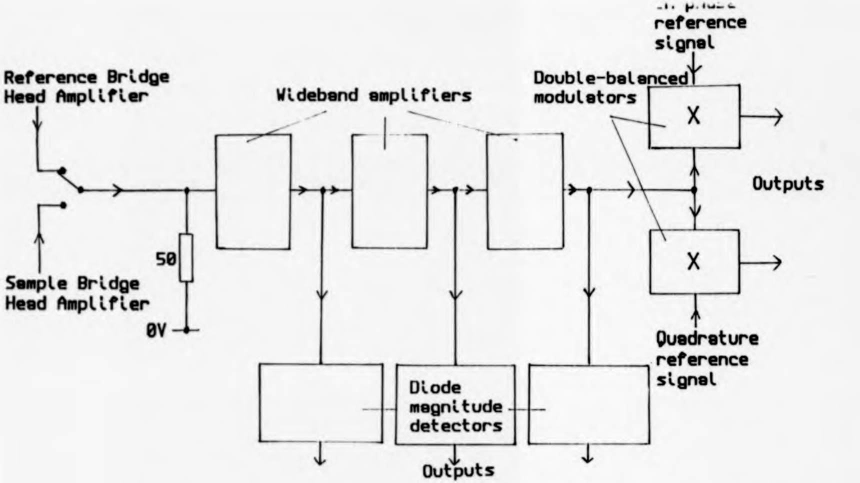

Fig. 4.21 High Frequency Detector System

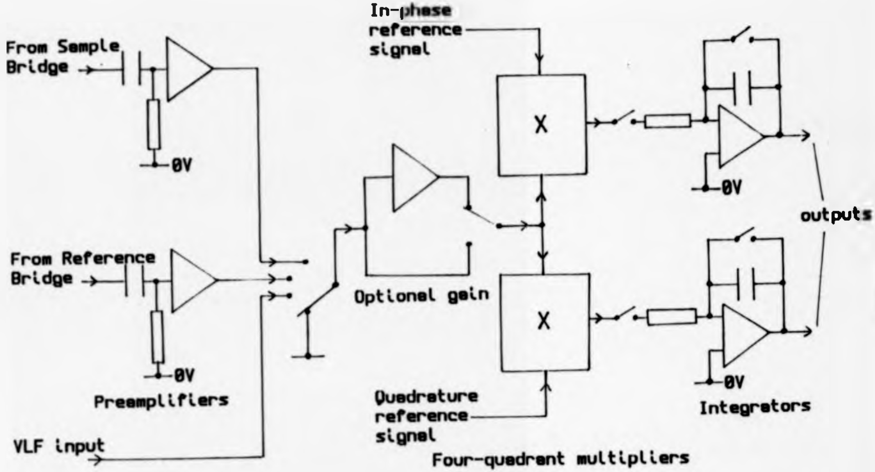

Fig. 4.22 Low Frequency Detector System

4.8.5 VLF detector system

Figure 4.23 shows schematically the hardware of the VLF detector system in the context of the other elements of the spectrometer active at VLF. The 220 Hz modulated signal is fed from the sample bridge head amplifier into a high gain narrow band amplifier. The VLF signal is recovered by multiplying the amplifier output with a suitably-phased 220 Hz reference signal. The multiplier output is filtered and then fed to an inverting op-amp integrator which has unity gain at 1Hz increasing to 10^5 at 10^{-5} Hz. The filtered integrator output is then fed back to the modulator by means of the 10^{10} Ω resistor. Thus, by negative feedback, the circuit arranges for there to be no 220 Hz signal generated at the modulator by making the voltage at the detector side of the modulated capacitor equal to that on the bridge side. Since the error signal at the integrator output closely resemble the input signal, the 10^{10} Ω resistor is heavily bootstrapped.

The modulator does not appear to generate flicker noise. Apart from the sample, which is unavoidable, the elements most capable of contributing flicker noise are the d.c. coupled components after the multiplier. Because of the feedback loop, the integrator output will contain the VLF noise at its input but suppressed by the considerable gain of the narrow band amplifier. The multiplier is temperature stabilised.

Outside the feedback loop, the integrator output is filtered and then fed to an integrating sampler. A pair of low drift op-amp integrators sample the signal alternately; one integrating whilst the other is read and then reset. An EVENT line from the waveform synthesiser provides a square wave repeating an integral number of times within each waveform cycle; a high level enabling one integrator, a low level enabling the other. Between 8 and 2040

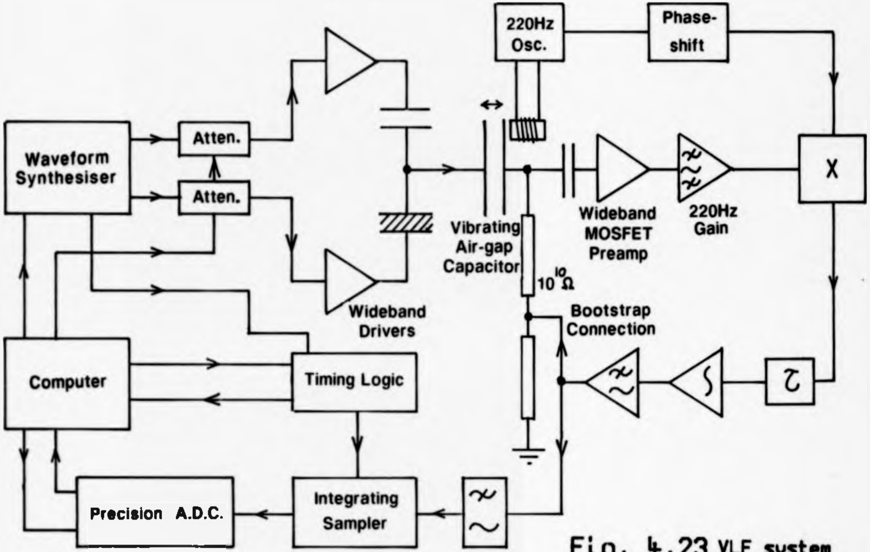

Fig. 4.23 VLF system

samples per cycle are made, with integration times varying from 1 to 50 seconds, depending on signal frequency. For long integration times, 12-bit DACs are used to back-off the integrator inputs by a voltage near to the previous reading; thus large standing voltages, which might cause overloading, are not integrated. With this scheme, no sample time is lost, providing a better signal-to-noise ratio than, for instance, a high speed 'combing' sampler, which would also unnecessarily occupy the system microcomputer. A mathematical correlation is performed on the sampler output data in the microcomputer providing signal amplitude and phase information.

Between 5 Hz and 0.1 Hz, although the parametric system is used, the frequencies are too high for the integrating sampler. The filtered integrator output is instead connected through to the hardware correlators described in section 4.84.

4.9 D.C. Voltmeter

A single d.c. voltmeter is used for the calibration of attenuators, reading of detector outputs and direct thermocouple measurements. A block diagram is shown in Figure 4.24. One of sixteen identical relay-switched inputs feeds an RS7650 chopper-stabilised operational amplifier (77) with relay programmable gains of 0.1, 1, 10 and 100. The input offset voltage of the RS7650 is maintained at about 1 μV by the use of an internal nulling amplifier, which, on one phase of a 'chopping' clock is itself nulled, and, on the other phase, is used to null the input offset of the main amplifier. The chopping frequency is set at 200Hz. A passive filter follows the amplifier to reduce chopping clock distortion and noise.

Analogue to digital conversion is provided by a Siliconix 7135 4½ digit panel meter device, see (78). The conversion cycle consists

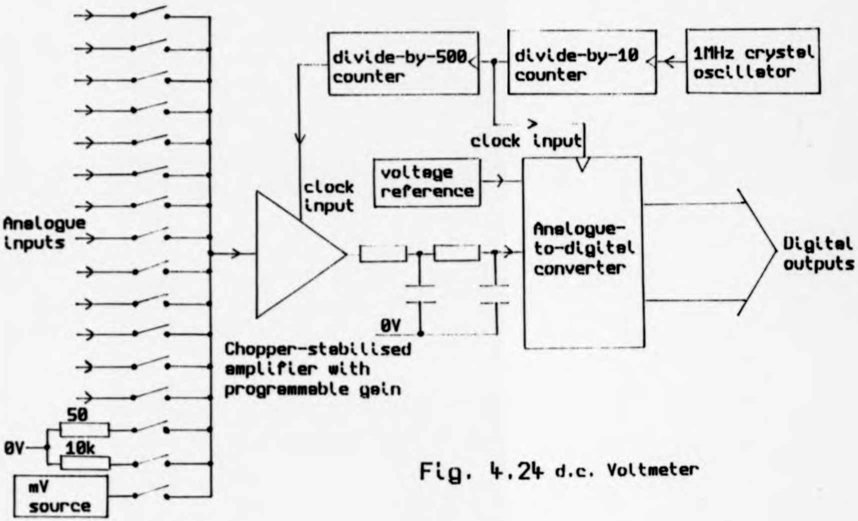

Fig. 4.24 d.c. Voltmeter

of four main phases:

i) Auto zero

ii) Signal integrate - the input voltage is integrated for 10,000 counts of the external clock

iii) Signal deintegrate - the time taken for the integrator capacitor to discharge, at a constant rate, is measured in terms of up to 20,000 cycles of the external clock

iv) Reset.

An external clock frequency of 100 kHz is chosen so that the signal integration time is an exact multiple of the period of any mains frequency harmonic. The total measurement time is then 400 ms. The chopper-stabilised amplifier clock is derived from the same oscillator to ensure that any chopping frequency harmonics will integrate to zero.

A bandgap device provides an absolute voltage reference. The input ranges are ± 20 µV, 200 µV, 2 V and 20 V each with a resolution of 1 part (that is 1 count) in 20000. With suitable interfacing, the sequenced BCD output can be read into the system microcomputer.

For most applications of the voltmeter, the long term absolute accuracy is less important than the linearity, for instance when a ratio of two readings is involved. However, for thermocouple measurements, absolute values to within several microvolts are important. For such purposes, one of the inputs is permanently connected to a calibrated millivolt source. Two zero references, one through 50 Ω and the other through 10 kΩ are also provided.

4.10 MICROCOMPUTER SYSTEM AND INTERFACING

4.10.1 System structure and philosophy

Figure 4.25 shows schematically the connections of the controlling computer to the other elements of the spectrometer. A

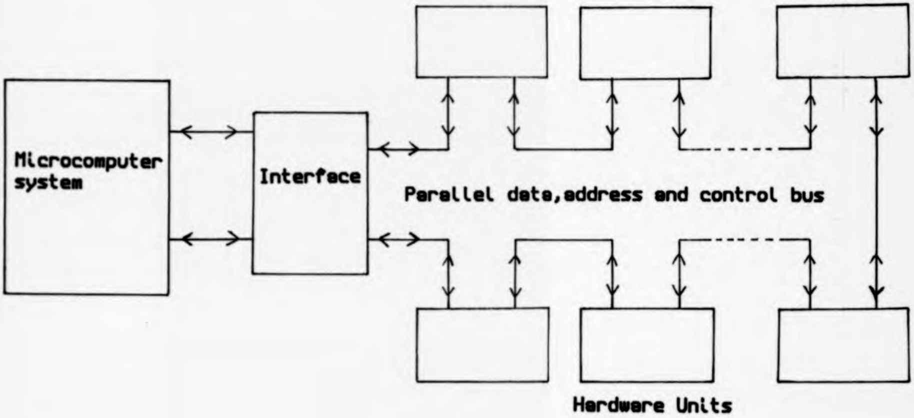

Fig. 4.25 Microcomputer Interfacing Scheme

microcomputer, supported by display and storage facilities, connects through an interface and bus system to a number of hardware units. Each hardware unit represents a specialised element such as a signal generator or detector.

Simplicity and flexibility are the design aims of the interfacing and interconnection scheme. A parallel bus is employed to simplify decoding at the hardware units; it is also faster than the equivalent serial implementation. Up to 32 different units can be addressed. There are no hardware interrupts; all bus exchanges, which can only involve the computer interface and one unit at a time, are initiated by the computer. All hardware units have in-built memory or latches so that they remain in the state dictated on the last occasion of their selection by the computer. Since bus time implies computer time, long sequential operations, such as moving stepper motors, are performed under local timing in the hardware unit. In this case, the unit would receive a short, high level instruction, then execute it, being re-available for instruction only when the task is completed. With this combination of central controller and distributed, partially autonomous units, a relatively simple microcomputer can often achieve as much as a complex multi-tasking machine.

4.10.2 System microcomputer

A BBC model B microcomputer, manufactured by Acorn Computers, Cambridge, UK, acts as the central controller, satisfying requirements by having extensive I/O facilities, a flexible machine operating system, particularly suited to the integration of high level and assembly languages, and by being extremely well documented.

A number of modifications are made to the basic machine. Extra RAM has been added to increase the capacity from 32K to 80K bytes. A ROM board has been fitted to enhance the firmware capacity by almost 200K bytes. An adaptation of the disc drive output enables the use of four double-sided floppy disc drives.

4.10.3 Interface and bus system

The computer interface consists of five bidirectional 8-bit ports and five output only, yet readable, 8-bit ports, each directly decoded from the microprocessor address bus, which is accessed through the '1MHz bus' port of the computer. Thus each port can be written to and read just as if it were a memory location inside the computer itself. The formulation of the bus system from these ports is shown in Figure 4.26. Some ports are not used at present.

Port 1 provides a 5-bit address to select the appropriate unit from up to 32, whilst also providing a 3-bit address to select from 8 locations within that unit. Since some of the spectrometer elements require more than 8 ports, and, therefore, more than one of the 32 addresses, the minimum unit, of which there can be 32, is designated a hardware-sub-unit, from which hardware units can be constructed.

Ports 2 and 3 provide a 16-bit address bus, which, at present, is used only with the waveform synthesiser.

Port 5 forms the 8-bit bidirectional data bus going to all of the hardware-sub-units.

Port 6 is used to generate various timing signals, such as data latching and bus direction controls.

Additional hardware timing is used to prevent bus contention. All bidirectional ports are automatically made inputs when the computer undergoes a soft or hard reset.

4.10.4 Hardware-Sub-Units

For ease of construction and for regularity, a printed circuit board arrangement has developed providing the 8 x 8-bit ports for a hardware-sub-unit. An example is shown in Figure 4.27 where 8 x

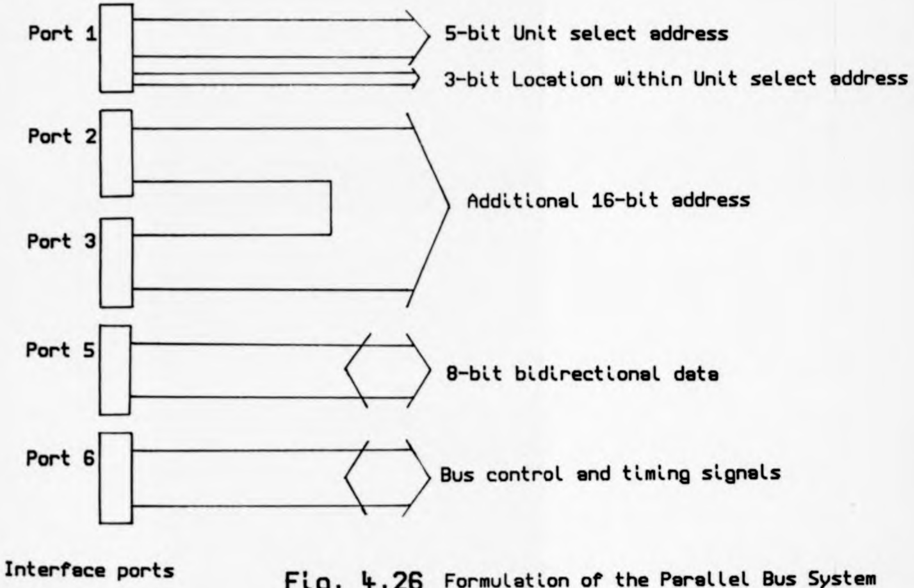

Fig. 4.26 Formulation of the Parallel Bus System

Fig. 4.27 Photograph of Typical Hardware-Sub-Unit (HSU)

8-bit DACs are driven. Data can be written to, or read from, each port through a 26-way IDC ribbon cable connection to the computer interface.

CHAPTER 5

Software Structure and Algorithms

5.1 INTRODUCTION

The comparatively small amount of RAM in the BBC model B has necessitated the partitioning of the spectrometer operating software. Although apparently a disadvantage, this has resulted in a forced hierarchy of routines particularly suited to the task. A structure has emerged consisting of three main software strata, machine level, BASIC level 1 and BASIC level 2.

5.2 SOFTWARE STRUCTURE

Figure 5.1 shows a memory map of the modified microcomputer. A particular feature of the Machine Operating System (MOS) is that it can support up to sixteen language, file or utility ROMs, known as sideways ROMs, which can be accessed one at a time within the address range (hex) 8000 - C000.

The machine level commands, which interface directly with the hardware units, are written in assembly language and are stored and RUN from sideways ROMs. BASIC level 1 routines are utilities written in BASIC and stored in sideways ROMs yet RUN in memory areas A and C of Figure 5.1. Only one BASIC level 2 program can be resident in the computer at any time, written in BASIC and situated in memory area F. The user normally interacts directly with BASIC level 2 which can then call either of the lower level routines. BASIC level 1 routines may call machine level routines, which are self-contained.

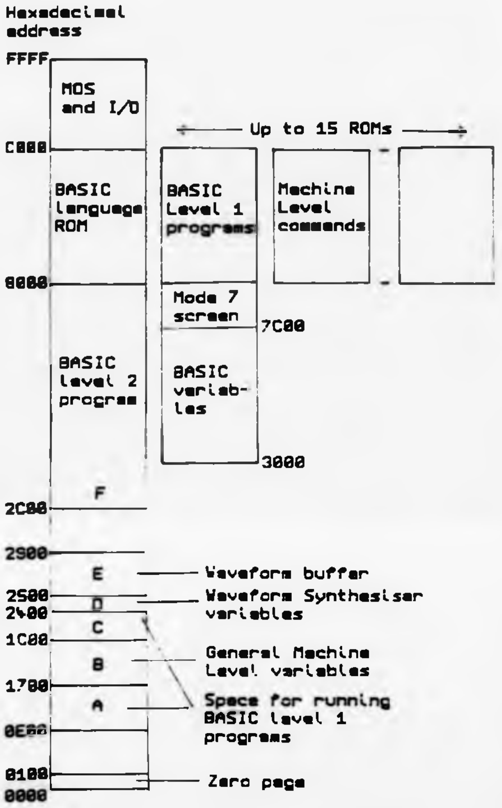

Fig. 5.1 Memory Map of the Microcomputer

5.3 MACHINE LEVEL ROUTINES

5.3.1 Introduction

When the BBC BASIC interpreter encounters a command prefixed by an asterisk, it passes control to the machine operating system, which which, if it cannot recognise the command, consults the sideways ROMs. By suitable programming, the sideways ROMs can enable the interpretation and execution of a complete new set of specialised commands tailored to the user's requirements. A list of such commands developed for the spectrometer is shown in Table 5.1. Brief descriptions of the main sections are given below.

5.3.2 Hardware Access

The commands listed in the Hardware Access section of Table 5.1 enable communication with most of the spectrometer elements. Simple input parameters are converted into appropriate data, address and timing signals. A record is maintained in memory area B of Figure 5.1 of various system parameters such as motor positions or gain settings. Where appropriate, BUSY flags are monitored before accessing a hardware unit. Failure to respond within a given time, detected using an interrupt-driven timer, results in an error signal. Data is returned in an easily digestible format to the calling program through a parameter block.

5.3.3 Waveform Synthesiser

The most complex routines performed at machine level control the waveform synthesiser: only assembled machine code can handle the large data transfers in a reasonable time. There are three major routines, these set the frequency, load the waveform and shift phase.

The principle of the frequency set routine is shown in the flow diagram of Figure 5.2. Since the maximum RAM addressing frequency is

TABLE 5.1 MACHINE LEVEL COMMANDS

Hardware Access	
***CAPSTEP x,y**	set reference bridge micrometers
***EUROTHERM X(,y)**	send mnemonic and data OR poll 3-term controller
***MADSET x,y,z**	set channel, gain, zero reference on dc voltmeter
***MADREAD**	read dc voltmeter
***RFATT x,y,z**	set 3 RF attenuators
***LFATT x,y**	set 2 LF/VLF attenuators
***FREQ x**	read frequency of channel x
***HSU x,y(,z)**	set OR read Hardware-sub-unit port
Waveform Synthesiser	
***CLEAR**	reset generator and microcomputer registers
***RAMFREQ x**	set frequency
***WAVELOAD f,ch,**	load waveform: specify file, channel, phase units
x,y,z	amplitude, bit precision (default EVENTS loaded)
***WAVESHIFT ch,x**	shift waveform: specify channel, phase units
***DELTAPHI, x,y,z**	specify number of gate delays in each channel
***ORTHOGANALISE**	creates orthogonal pair from 8-bit waveform
x,y,z	specify: channel, address, samples per cycle
***WAVEGO,*WAVESTOP,*ONESHOT**	synchronous start/stop
***WAVEOFF**	asynchronous stop
***DOWNLOAD,*UPLOAD,*PRELOAD**	direct load commands
***RAMSHIFT,*STARTSTOP,*EVENT,*LATCH**	access to low level routines
Databases	
***TYPE-T,*TYPE-K**	access to thermocouple microvolts vs temperature database with deg/10 interpolate
***ATTENUATION**	access to LF attenuation vs setting database (only a guideline)
Timing	
***WAIT t**	wait for given time in centiseconds
***OUTTIME t**	set time-out
***INTIME**	cancel time-out
Screen Control	
***PSCREENON/OFF**	enter/leave split screen mode
***WINDON x**	enter window on split screen
Parameter transfer	
***PARAMBLOCK x**	set address for parameter exchange with high level software

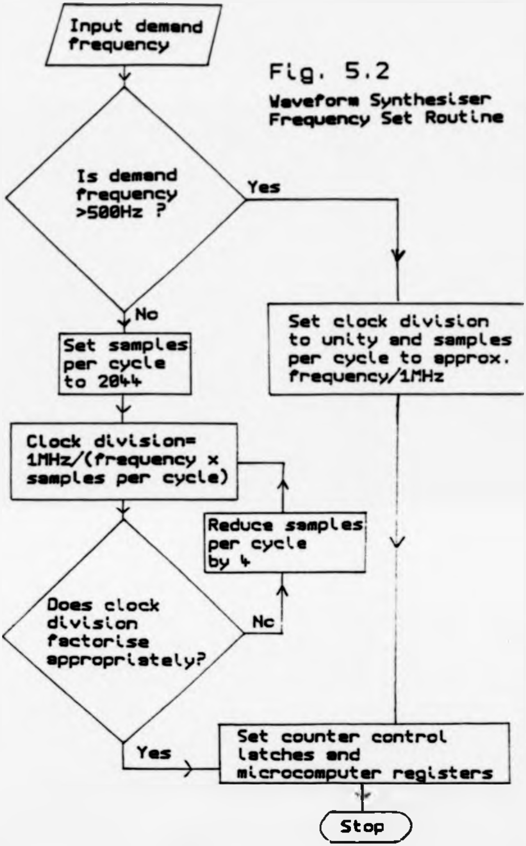

Fig. 5.2

Waveform Synthesiser Frequency Set Routine

1 MH_z and the maximum number of samples per cycle is 2044, the lowest frequency before extra clock division is required is about 500 Hz. For frequencies below this, a clock division must be found which can be achieved using a series of 4-bit divide-by-n counters. To ensure good waveform symmetry, and to simplify loading, only multiples of four samples per cycle are permitted.

Even machine code takes an inconveniently long time to compute thousands of values of a sine function since each requires a series expansion. In fact, it is not the instantaneous value of the sine function which is loaded but the integral over each particular sample period. It has proved far quicker to load the waveform information from a floppy disc. Memory space is conserved by saving only the first quadrant of the sinewave. The loading routine scales the data by an appropriate amplitude factor, and then, through reflection, loads each of four allotted RAM locations within the waveform synthesiser. The sinewave file is 192 k bytes in length, providing 16-bit data points for sinewaves with between 1024 and 2044 samples per cycle. Sinewaves with fewer samples per cycle are derived from these by averaging binary-scaled groups of points. Thus for 100 samples per cycle, as used at 10 kHz, data are derived from the 1600 samples file-entry.

Memory area D in Figure 5.1 is reserved for various waveform synthesiser parameters. A phase-table is set up storing the relative offsets of the three channels in phaseunits; there are twenty times as many phaseunits as samples in a cycle. Phase shifts are made by offsetting the clock signals α, β and γ described in section 4.6.1 and by shifting the order of data within the RAM. The phase shift routine updates the phase-table, computes the apportionment between α, β, γ offsets and RAM shifts and then implements these. Rather than download the whole RAM contents to the computer and then shift and reload, which would require a lot of computer memory, each byte is read and then stored at its new location, the previous contents of which are similarly re-located, and so on, until the complete sequence has been moved. Checksums performed before and after phaseshifts limit the propagation of errors due to data corruption. The smallest phase shifts, controlled by inserting gate delays in the α, β and γ signal paths, are controlled quite separately using the *DELTAPHI command.

5.3.4 ROM Databases

To relieve the burden of performing complex expansions, a look-up table containing the microvolt outputs of type-T and type-K thermocouples, for every degree (K) of their working ranges, is stored in a 16k-byte ROM. Also included is a routine giving one-tenth of a degree interpolation.

A database, derived from a complete d.c. calibration of the low frequency attenuators, avoids the trusting of nominal values when setting waveform amplitudes. After a bridge balance, however, the exact attenuation is remeasured.

5.3.5 Timing Functions

Timeout and wait functions are commonly used in the machine code routines which interact directly with the hardware units. The facility is extended to BASIC routines by the *WAIT, *OUTIME and *INTIME commands. The former is admittedly easy to implement in BBC BASIC, though with more instructions; timeout, however, being interrupt-driven, provides a means of escape from an otherwise endless loop if a time limit has been exceeded.

5.4 BASIC LEVEL 1 ROUTINES

5.4.1 Introduction

It was mentioned in section 5.2 that BASIC level 1 routines are RUN in memory areas A and C of Figure 5.1. Two sub-levels have been established: those routines RUN in area A are termed ROM-based procedures, since area A is only available when using the ROM filing system, and disc-based procedures, which may be loaded from disc into memory area C, although, at present, most are loaded from ROMs. ROM-based procedures may be up to 2.25k bytes in length, whereas disc-based procedures must not exceed 2k bytes. Strategically they are similar, the latter being used whenever disc drives must be accessed. There is, however, an important mode in which a disc-based procedure may call ROM-based procedures, which, after completion return control to the disc-based procedure. In this way quite complicated functions such as tuning the oscillators, can be performed.

The routines are entered by the customised commands:

```
*PROCdisc <filename>
*PROCROM <filename>
```

which load a routine and divert the BASIC interpreter to the first line which is indicated by either of:

```
*DEFPROCdisc
*DEFPROCROM.
```

Exit and return to the calling program are initiated by the commands:

```
*ENDPROCdisc
*ENDPROCROM.
```

The functional spread of BASIC level 1 routines is broad, as is indicated by the list of Table 5.2. Considerations of space forbid a

TABLE 5.2 EXAMPLES OF BASIC LEVEL 1 ROUTINES

	Disc Based	ROM based
SETTING UP		
Oscillator tuning:	osctune	osccoil,setcoil,
Phase-Splitter lock	split	
Phase-lock	lock	setlock,qdac0, caplock,varlock
		backset,beat
Back-off		fastdac,slowdac
Waveform Synthesiser	wsfreq	avbvset
Integration time		integ-t
Set up VLF sampler		VLFset
VLF lock-in	VLFlock	
CALIBRATION		
Measure DAC dc ratio		wsdcrat
Calibrate VLF sampler	VFLcal	
Calibrate LF attens.		LFattdc
Calibrate thermocouple	T-menu	cal0C,cal100C, cal-1N2
Calibrate dcnV		calmad
DATA ACQUISITION		
Read LF correlators		readLF
Read VLF correlators	VLFread	vread
Read temperature		T-read
DATA PROCESSING		
VLF correlation	VLFcorr	Vcorr
VLF ramp removal	VLFramp	vramp
find VLF balance	VLFcalc	
DISPLAY		
plot VLF signal	VLFplot	vbox
plot RAM waveform	qadplot	
DATA FILING		
catalogue data	cat	
store VLF waveform	VLFsave	
load VLF waveform	VLFload	

full description, however three representative routines are discussed below; the tuning of the oscillators, the measurement of the waveform synthesiser DAC d.c. ratio and VLF ramp-removal.

5.4.2 Oscillator Tuning

Tuning of the oscillators requires up to several level 1 routines; a disc-based procedure 'osctune' calls six ROM-based procedures. The flow chart describing osctune is shown in Figure 5.3.

Before tuning takes place, all of the tuning capacitors are set to their minimum positions. For the varicap diode this means simply setting the reverse volts to a maximum, and, for the switched capacitor bank, the relays must be opened. The motorised variable capacitor is free to rotate about 360°, without stops or position indicator, and is therefore more difficult to minimise. The routine 'minicap' is called which, by operating relays, selects the highest frequency coil with its transmission line connection to the motorised capacitor. The capacitor is then adjusted by moving the motor in one of two directions: one relay sends it clockwise at a constant speed, maintained by a control loop, the other anticlockwise. By measuring the oscillator frequency, the position of minimum capacitance can be found. Inevitably the motor will overshoot after which it is moved back slowly, by pulsing one of its control relays, to the correct position. When neither motor relay is activated, the voltage across the motor windings is actively maintained at zero, providing rapid braking.

Next, the database routine 'osccoil' is consulted to determine the appropriate coil setting which is then set using 'setcoil'.

The routine 'setbank' progressively works its way down the

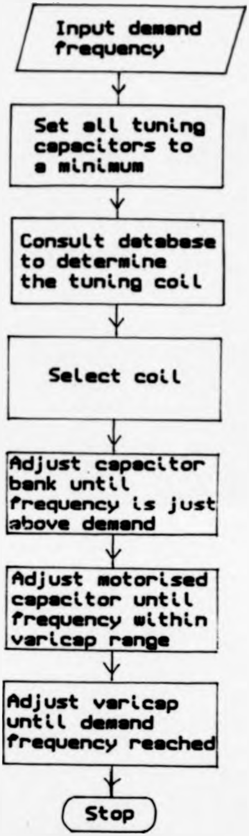

Fig. 5.3
Oscillator Tuning Procedure

binary-scaled capacitor bank, starting with the most significant bit (largest capacitance). If the frequency is above the demand, then the bit is retained, else it is rejected. This is an implementation of a 'successive approximation' procedure which is also used in the fast back-off routine, 'fastdac'.

The routine 'setcap' sets the frequency marginally above demand using the overshoot method described above. Final tuning is by 'varicap' which adjusts the tuning voltage in coarse steps until an overshoot occurs, and then re-traces with fine adjustments.

Normally the tuning procedure is repeated for both oscillators, then the phase-splitter amplitude-lock routine 'split' is activated followed by a phase-lock using 'lock'.

5.4.3 Measurement of Waveform Synthesiser DAC d.c. ratio

The only meaningful place to measure the d.c. ratio between the waveform synthesiser DACs is at the summer drivers. Since below 500 Hz the summer-drivers are operated in the unity gain mode, accurate measurements can be made at the inputs. The same points may be used for the d.c. measurements on the LF attenuators.

The meausuring scheme is outlined in the flow chart of Figure 5.4. Two cycles of a high amplitude (±2 V at the bridge) square wave are loaded into the waveform synthesiser, the output of which is enabled and fed through the LF attenuators, set at 0dB attenuation, to the summer drivers. The voltages on the positive and negative half-cycles of the sample arm summer-driver are measured on the first cycle, and those on the reference arm summer-driver on the second cycle. The DAC ratio is then calculated from the ratio of the differences between each pair of readings. In this way any voltage offsets are cancelled out and, because of the waveform symmetry, no

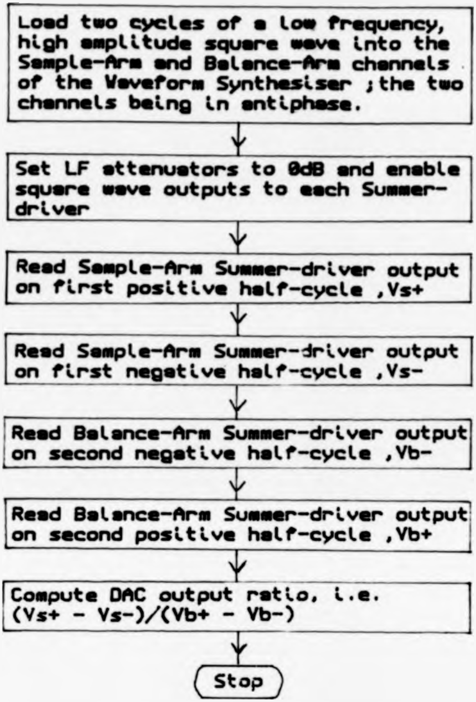

Load two cycles of a low frequency, high amplitude square wave into the Sample-Arm and Balance-Arm channels of the Waveform Synthesiser ;the two channels being in antiphase.

Set LF attenuators to 0dB and enable square wave outputs to each Summer-driver

Read Sample-Arm Summer-driver output on first positive half-cycle ,Vs+

Read Sample-Arm Summer-driver output on first negative half-cycle ,Vs-

Read Balance-Arm Summer-driver output on second negative half-cycle ,Vb-

Read Balance-Arm Summer-driver output on second positive half-cycle ,Vb+

Compute DAC output ratio, i.e. (Vs+ - Vs-)/(Vb+ - Vb-)

Fig. 5.4
Scheme for Measuring the d.c. ratio between Waveform Synthesiser DACs

net sample charging occurs. Each cycle takes about 20 seconds giving time for settling and averaging of readings.

The waveform synthesiser is also used for attenuator calibration, where again a polarity switch is performed. Care is taken in software to ensure that all d.c. inputs have settled or, at worst, are varying randomly.

5.4.4 VLF ramp-removal

At VLF, only a limited number of cycles of the balance signal can be recorded in a reasonable time. Long time transients and voltage changes due to charge accumulation at the balance point often appear as ramp functions which are superposed on the true balance signal. When performing a software correlation on such signals, the ramp function will contribute as if it were a sawtooth function with the periodicity of the reference signal, leading to serious errors in the analysis. To prevent this, a simple pre-treatment is performed on the data.

The timing signals for the VLF integrating sampler are arranged such that the number of data points per cycle is always a multiple of eight. Therefore, the data can easily be separated into quadrants with an equal proportion of data points from each of the interlaced integrators which, though calibrated, may be slightly imbalanced. Now if the integrals over the quadrants in order are I_0, I_1, I_2 and I_3 and if:

$$g = (I_1 + I_3) - (I_0 + I_2)$$

then for a pure sinewave of any phase and superposed about any d.c. level, g will be zero through antisymmetry. However, if the cycle time is t and a ramp of gradient m is present, then:

$$g = \frac{mt}{8}$$

Thus the gradient can be discovered and the ramp subtracted from the data before correlation. Normally the ramp removal is performed on a cycle by cycle basis, the d.c. level being subtracted at the same time. An example of a measured signal before and after ramp removal is shown in Figure 5.5.

It is possible that genuine harmonic distortion could be mistaken for a ramp and therefore cause error. This is unlikely since, at VLF, the generator output is especially pure, having many samples per cycle, and the summer-drivers have very heavy feedback, leading to high linearity. Harmonic distortion is not observed in practice.

At frequencies below about 5 mHz, where in excess of 200 integrated samples per cycle are taken, the data are compressed, by averaging a number of points prior to calculation, in order to preserve memory space and minimise computer time.

5.5 BASIC LEVEL 2 ROUTINES

5.5.1 Introduction

Four BASIC level 2 routines provide the user with menu-style access to functions ranging from discharging the balance point to an automatic scan of the sample impedance over a particular frequency range. The most important routines, however, are those which balance the bridges in the various frequency regimes, and, since space is limited, it is these that are discussed below.

5.5.2 High Frequency Balancing Algorithm

At frequencies above 20 kHz, the phase uncertainties at the detectors and the relatively poor quality of the correlators compared to those used at low frequency, have led to the acceptance of magnitude information only. Each step of the balancing operation,

Fig. 5.5a 0.1Hz signal as measured

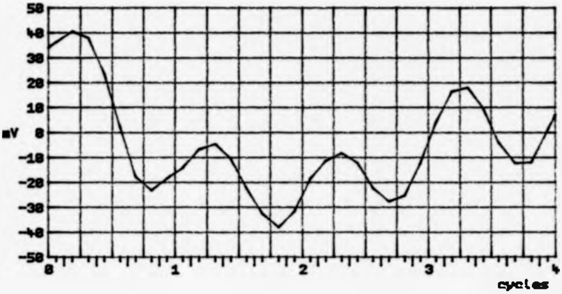

Fig. 5.5b 0.1Hz signal after ramp-removal

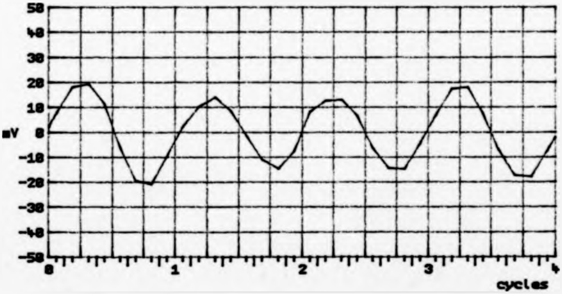

where a minimum or zero is required, is based on a three point calculation as illustrated by Figure 5.6. Adjustments are made in a direction which minimises the magnitude until the gradient changes direction. It is assumed that the gradient G has the same magnitude either side of the minimum, that being either:

$$\frac{m_2 - m_1}{x_2 - x_1} \quad \text{or} \quad \frac{m_3 - m_2}{x_3 - x_2}$$

whichever is larger. The minimum is then found at:

$$x_{min} = \frac{(m_1 + Gx_1) - (m_3 - Gx_3)}{2G} \tag{5.1}$$

x_{min} may represent either a capacitance setting or signal amplitude. By this means it is not absolutely essential to go to the minimum, usually a measurement within 1% of the minimum is sufficient to extrapolate a 0.1% reading.

Using the techniques outlined in Chapter 2, the following overall procedure is adopted:

i) the approximately set 0° and 180° amplitudes are adjusted to give a minimum on the sample bridge detector.

ii) the reference bridge is then used to set the phases of these 0° and 180° signals exactly.

iii) the 90° signal is added at a sufficient amplitude to coherently switch the reference bridge detector, and its phase is correctly set.

iv) the 180° amplitude is re-adjusted to find the real sample bridge minimum.

v) the 90° amplitude is adjusted to find the imaginary sample bridge minimum. If this amplitude is much different from that used in (iii) then re-phasing may be necessary.

vi) the 0-180° ratio is determined by measuring the reference bridge capacitance ratio set at 175 Hz.

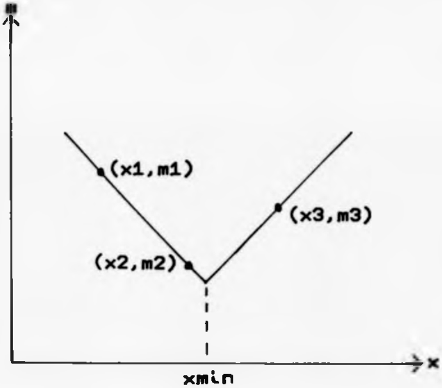

Fig. 5.6 Minimum from 3 Points

vii) the 90°:180° ratio is determined by the diode/d.c. method described in section 3.5.3.

5.5.3 Low frequency balancing algorithm

Between 20 kHz and 0.1 Hz, as a result of equation 3.2, the correlator outputs V_1 and V_2 may be described by the linear equations:

$$V_1 = (A-A_{bal})\, k_1 + (B-B_{bal})L_1 \qquad (5.2a)$$

$$V_2 = (A-A_{bal})\, k_2 + (B-B_{bal})L_2 \qquad (5.2b)$$

where A is the real part of the bridge drive voltage ratio and B the imaginary part, A_{bal} and B_{bal} are the respective values at balance. K_1, L_1, K_2 and L_2 are functions of all bridge impedances and relevant detector parameters and the sample arm drive voltage. In order to evaluate the six unknowns, A_{bal}, B_{bal}, K_1, L_1, K_2 and L_2, it is necessary to take readings of V_1 and V_2 for three different pairs of A and B which are denoted (A_C,B_C), (A_N,B_N) and (A_E,B_E) with the restriction that,

if $\mathbf{N} = (A_N,B_N) - (A_C,B_C)$

and $\mathbf{E} = (A_E,B_E) - (A_C,B_C)$

then $\mathbf{N}\mathbf{x}\mathbf{E} \neq 0$

ie the vectors **N** and **E** must not be zero or either parallel or antiparallel. The subscripts C, N and E denote 'Centre', 'North' and 'East' and the procedure is referred to as the C-N-E routine.

If V_{1C}, V_{1N} and V_{1E} are the values of V_1 obtained in each case then:

$$V_{1N}-V_{1C} = (A_N-A_C)K_1 + (B_N-B_C)L_1 \qquad (5.3a)$$

$$V_{1E}-V_{1C} = (A_E-A_C)K_1 + (B_N-B_C)L_1 \qquad (5.3b)$$

that is two linear equations in K_1 and L_1 which are readily solved. K_2 and L_2 are similarly obtained from V_{2C}, V_{2N} and V_{2E}. By substituting these values into equations 5.2a and 5.2b for any one of the C, N or E cases, typically the one nearest balance, we have a means of solving for A_{bal} and B_{bal}. Thus the balance point can be predicted from three off-balance readings. It is usual then to attempt actual balance. Even if this is not exactly possible, each new reading of V_1 and V_2 can be used to produce a refined estimate of the true balance position using the known, K_1, L_1,K_2 and L_2 values.

Normally, because of restricted detector dynamic range, an initial C-N-E routine is performed at low drive amplitude in order to estimate roughly the balance point. A second C-N-E routine at high amplitude, centred on the rough estimate, then provides a more precise estimate of balance. A number of further iterations confirm the measurement. It is sometimes beneficial to increase the detector gain near to balance, before performing the second routine. In practice, it is convenient to make N and E parallel respectively with increasing A and B. In this way, with a restricted dynamic range at the detector, the maximum excitation of K and L responses can be applied alternately.

After a bridge balance, the attenuators are calibrated and the exact amplitudes and phases are determined. A similar procedure is adopted for all three bridges. Where a baseline correction is required, the reference bridge is balanced before the sample bridge.

5.5.4 VLF balancing algorithm

At VLF, the correlation is performed in software. Equations 5.2a and 5.2b still apply but with the simplification that:

$K_1 = L_2$ and $K_2 = -L_1$

because the two 'correlators' are identical with perfectly orthogonal references. In this case, only two sets of conditions (A_C,B_C) and (A_V,B_V) are required with the proviso that:

$V = (A_V,B_V) - (A_C,B_C) \neq 0$

(The subscript 'V' is for 'vector'). We then have

$$V_{1V}-V_{1C} = (A_V-A_C)K_1 + (B_V-B_C)L_1 \quad (5.4a)$$

$$V_{2V}-V_{2C} = -(A_V-A_C)L_1 + (B_V-B_C)K_1 \qquad (5.4b)$$

which are readily solved for K_1 and L_1; A_{bal} and B_{bal} are computed as before. Normally a balance is attempted with iterations as required. Since the VLF detector has a very wide dynamic range, the routine is only performed once, that being at high drive amplitude. The balance point waveforms at each stage are recorded on floppy disc for future examination, examples of which can be seen in Figure 5.7.

Because of the effects of transients, a number of 'pre-cycles' can be selected before data points are recorded. After these, the balance point signal is monitored for a programmable number of 'post-cycles'.

5.6 TASKS

A fourth software stratum has been developed which allows the user to pre-record a set of level 2 menu entries, known as TASKS. Thus any particular measurement itinerary can be pre-programmed, with temperature changes and recalibrations, or whatever, as often as required. Libraries of TASKS are stored on floppy disc.

5.7 DATA STORAGE AND FURTHER ANALYSIS

A data filing system has been adopted based on a row-column addressable matrix of real variables and a single column of character strings.

A file may contain up to 30 sections, some for real variables others for strings, and all with individual headings and descriptive strings. A single measurement of sample impedance has allocated to it one row with 50 column entries for variables and one 255 character string for comments.

Additional programs have been written for manipulating files of this structure including cubic-spline fitting and data plotting. Future programs will also operate on this format.

Fig. 5.7a VLF balance: Centre

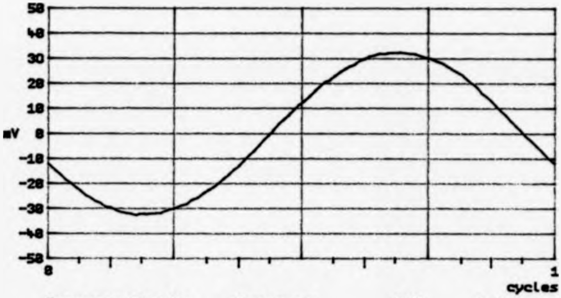

Frequency 1E-2 Hz   Sample arm   2 V   0 degrees
Temperature 300 K   Balance arm   1 V   180 degrees
Pre-cycles 1   Detector o/p 3.25E-2 V   201.00 degrees

Fig. 5.7b VLF balance : Vector

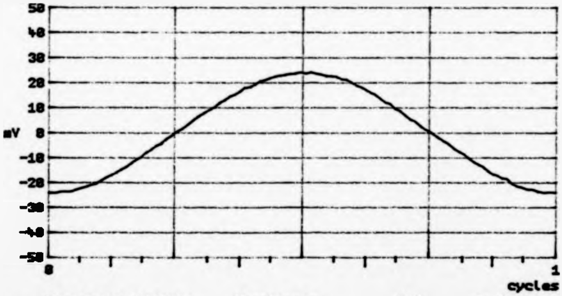

Frequency 1E-2 Hz   Sample arm   2 V   0 degrees
Temperature 300 K   Balance arm   0.820 V   101.75 degrees
Pre-cycles 1   Detector o/p 2.30E-2 V   200.24 degrees

Fig. 5.7c VLF balance : First iteration

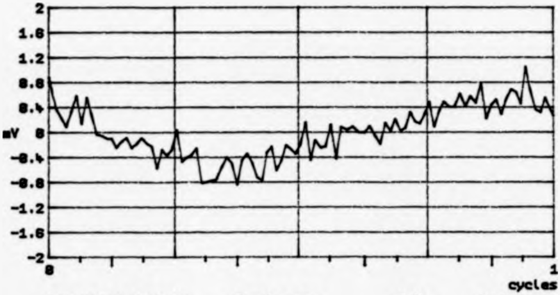

Frequency 1E-2 Hz   Sample arm   2 V   0 degrees

Temperature 300 K   Balance arm   0.820 V   170.21 degrees

Pre-cycles 1   Detector o/p   5E-4 V   134.44 degrees

Fig. 5.7d VLF balance : Second iteration

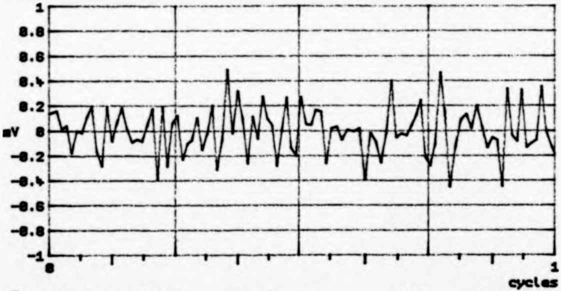

Frequency 1E-2 Hz   Sample arm   2 V   0 degrees

Temperature 300 K   Balance arm   0.827 V   170.20 degrees

Pre-cycles 1   Detector o/p   0 V   313.48 degrees

CHAPTER 6

Spectrometer Performance

6.1 INTRODUCTION

Preliminary tests have been carried out to assess the spectrometer performance. The tests include isothermal investigations of the dielectric behaviour of poly(methylmethacrylate) (PMMA) at 35 °C and low density polythene (LDPE) at 30 °C over the frequency range of 3×10^{-4} Hz to 10^{8} Hz. Indications are given that the spectrometer can, in general, meet the design requirements although some modifications are suggested.

This chapter presents estimates of measurement precision, based on repeatability, over the high, low and very low frequency ranges. Attention is given to those components whose non-ideal behaviour has restricted the performance.

6.2 TEMPERATURE VARIATION

The sample cell temperature variation system has been tested successfully over the range -180 °C to +350 °C. At the lower temperatures, a gas flow rate of up to 200 litres/min is required, whilst above room temperature, a flow rate of 12 litres/min is sufficient. Following the optimisation of the loop control parameters, the temperature could be maintained to 0.1 °C by the Eurotherm 820 controller.

6.3 ELECTRICAL PERFORMANCE

6.3.1 Introduction and general comment on testing

The spectrometer is constructed from a number of interacting hardware and software units, each of which must function correctly for the proper operation of the whole system. In turn, many of the units described previously, for example the oscillators or the parametric system, are multi-stage circuits involving combinations of amplifiers and subsiduary control loops or interfaces which in themselves must function correctly. For this reason, functional testing has had to become part of construction and even an extension of the design process.

Certain common practices were adopted for the development of complex analogue circuits. Firstly, the minimum, or open-loop, arrangement was functionally tested by observation (usually by oscilloscope) of the response to test waveforms, d.c. conditions, or noise levels as appropriate. If circuit parameters needed to be altered to meet design requirements then adjustments were made. Inputs for external control, such as frequency or amplitude variation, were added. The input range for which the output response was monotonic with the control input, and of the right sense, was determined and optimised, in the normal manner (79), (80), to maximise control, minimise noise and reduce unwanted interaction between different loops.

Complex digital systems, such as the computer interface and waveform synthesiser, were tested initially using a multi-channel logic analyser. In this way, critical timing waveforms as well as basic functioning could be checked. Once connected to the computer, more complicated test routines were performed. Repetitive accessing of ports within units enabled convenient oscilloscope monitoring of waveforms to determine whether, for instance, extra bus terminations were required. By performing statistical tests, low noise immunity problems, due to, for example, the misalignment of supply voltages between communicating units or insufficient earthing, could be diagnosed.

The software is the most flexible component of the spectrometer. Routines were adapted, therefore, to maximise the hardware performance. Although much of the program structure could be written in advance, some aspects, such as integration and wait times, were optimised, through experimentation, leading to the most acceptable spectrometer performance.

The spectrometer implementation, as described, is, therefore, the result of much experimentation.

The interaction between units is in most cases more of an inter-dependence. For example, the detector systems will not function completely without synchronising signals from the respective signal generators. For this reason, and since much of the normal operating software involves self-calibration, the performance of spectrometer components has been measured, and is described in the following sections, in the context of the complete machine operating in the three frequency regimes: high, low and VLF. However, tests carried out on certain key components, notably the summer-drivers, the reference bridge and the detector head amplifiers, are described individually since these are used in more than one frequency regime and can be tested in relative isolation.

6.3.2 Summer-drivers

6.3.2.1 Introduction

Ideally, the summer-drivers should be linear, wideband amplifiers providing a good summation of inputs, with a low output impedance and low output offset voltage. A series of tests were performed to determine the characteristics of the circuits. Permanent monitor points, consisting of two 100 Ω resistors connected in series between the output and the ground plane, with a co-axial take-off between the junction of the resistors and the ground plane, facilitated both a.c. and d.c. measurements.

6.3.2.2 Output Impedance

A prototype summer-driver was constructed. It was upon this circuit that measurements of output impedance were made by measuring the change in amplitude of a test frequency signal at the summer-driver output due to the application of various test impedances. The impedance at which the amplitude would have fallen by half its unloaded value was then calculated. The output impedance was computed to be 1.8 Ω at around 10 MHz and below, rising to 3 Ω at 100 MHz.

6.3.2.3 Frequency Response

The frequency response of the basic summer-drivers was estimated by measuring the amplitude ratio between the output signal and an input signal derived from a variable frequency source. No resonances were observed and no fall in amplitude response could be discerned, at least using an oscilloscope, until about 105 MHz.

6.3.2.4 Summing Action and Linearity

The summing action was tested at the highest frequencies by feeding an identical signal into two inputs simultaneously and comparing the output amplitude with that due to one signal only of the same amplitude. Correct operation was confirmed at oscilloscope accuracy. However, more rigorous tests were performed at 175 Hz with no external feedback. The component of output voltage in phase opposition with one input was measured, using the low frequency correlators, for various amplitudes at that input. The process was repeated for various amplitude levels of a quadrature signal at a second input.

Figure 6.1 shows the output signal component in phase opposition with a single drive input at 175 Hz, all other inputs being zero, plotted as a function of the amplitude of the single drive input. The overall voltage gain is about -2. The mean

Fig. 6.1 Variation of Summer-driver Output Amplitude with Input Amplitude at 175 Hz

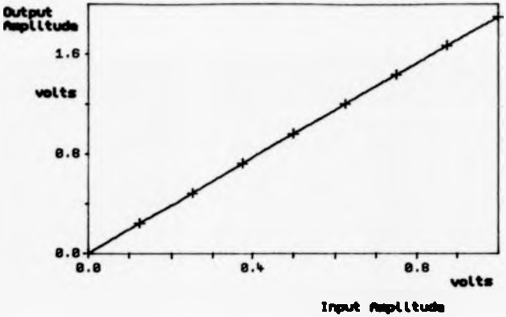

Fig. 6.2 Variation of Summer-driver Large-Signal, In-Phase Gain with Quadrature Input Amplitude at 175 Hz

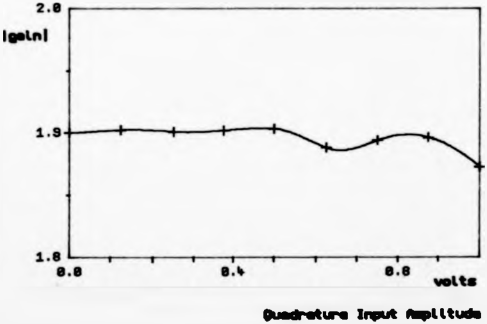

deviation from a straight line is less than 1%, which suggests that the total harmonic distortion due to the summer-drivers, at least at low frequencies, is of that order. Similar plots were found for the same function in the presence of the quadrature signal at a second input. The absolute voltage gain of the basic summer-driver, derived from gradient calculations, in response to the first input is plotted as a function of the amplitude at the second input in Figure 6.2. It can be seen that the gain from the output to a first input may vary by up to about 1.5% as the amplitude at the second input is altered. Thus, if the amplitudes of the two input signals are A_{sd} and B_{sd} respectively, the output of the summer driver Vsd can be represented approximately as:

$$V_{sd}=G_aA_{sd}(1-yB_{sd})+jG_bB_{sd}(1-yA_{sd}) \qquad (6.1)$$

where G_a and G_b are the gains for one input only and y is a factor no greater than about 0.015. Thus measurements of the quadrature component, without the other component, as suggested in section 3.5.3 may be subject to errors of up to about 1.5%, which if not corrected, will lead to a similarly erroneous value for the loss tangent.

At higher frequencies, it might be expected that y should increase. However, since the interchannel isolation relies heavily on the performance of transistors TR1, 2, 3, 4 of Figure 4.16, which have a quoted transition frequency of about 1.3 GHz (81), and since attempts have been made to restrict earth current flows and screen the transistors (see section 4.7), the circuit operation at 100 MHz is not dissimilar to that at much lower frequencies. Additive cross-coupling between inputs, due to, for instance, cable pick-up or earth currents, causes no error, only an equivalent change in Ga and Gb for that frequency, unless intermodulation occurs.

Although definitive measurements have not been made, observations of balance point waveforms suggest that the second harmonic distortion due to the summer-drivers above 10MHz rises to perhaps a few percent. The increased distortion is most probably a result of the capacitative loading on the final stage follower TR7.

Since, at the end of the balancing process of section 3.5, the real part of the sample bridge balance condition is always reflected in the reference bridge capacitance ratio, it is the measurement of this ratio and not any cross-coupling terms or non-linearity in the summer-drivers, which is important in the calculation of the sample capacitance. This ratio is measured, at 175 Hz, with the summer-drivers in mode 2 described in section 4.7, where no summation is required and where the negative feedback reduces distortion to insignificant levels. Provided that the high frequency detectors do not respond significantly to harmonics, therefore, distortion due to the summer-drivers is not a primary source of error in the determination of sample capacitance.

6.3.2.5 Output Offset Voltage

The d.c. output offset voltage of the summer-drivers could be maintained to within 0.5 mV of ground.

6.3.3 Reference Bridge

Although greater capacitance ratios can be supported, the normal operating ratio of the reference bridge is 5:1 since, by this choice, end effects can be largely avoided and a similar geometry is maintained over the capacitance range. Figure 6.3 shows the variation in capacitance ratio with the micrometer reading on one drive arm, whilst the other arm is set at 6000 microns: 0 corresponding to the fully wound in, or maximum capacitance, position. The capacitance ratio was determined by balancing at 175 Hz. Since the capacitance ratio is always determined by such a bridge balance, the linearity of capacitance variation is unimportant although it is reassurance of good design.

Fig. 6.3 Variation of Reference Bridge Arm Capacitance Ratio with Balance Arm Micrometer Position

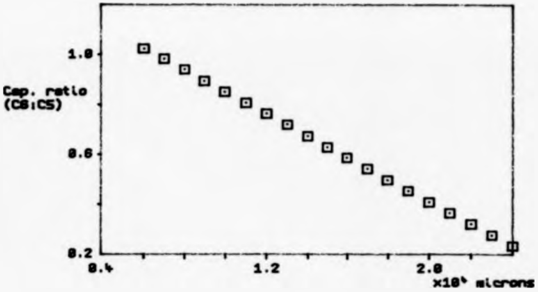

Fig. 6.4 Reference Bridge Head Amplifier Output Variation with Capacitance Ratio, for Balance Arm Drive Only, Showing Frequency Dependent Voltage Magnification Effect

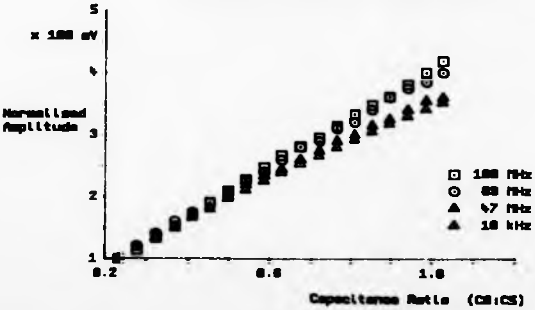

Measurements on the reference bridge above about 10 MHz yielded capacitance ratios in disagreement with those found at lower frequencies. The error was such that the measured ratio was always nearer to unity than expected. Since the effect seemed to increase more rapidly than a linear function with frequency, a series resonant model was proposed to describe the behaviour. It was suspected that the flexible braided connections to the arm capacitances were the major sources of inductance and that the resonance may be described by equation (6.2):

$$V_C = V_O/((1-\omega^2 LC)+j\omega CR) \qquad (6.2)$$

where V_C is the signal voltage across a bridge arm, V_O is the drive signal, L is the series inductance, R the series resistance of the feed wire and C is the combination of the arm capacitance and strays to ground. Equation (6.2) may also be written:

$$V_C=V_O/((1-\omega^2/\omega_O{}^2)+j\omega/Q\omega_O) \qquad (6.3)$$

where ω_O is the resonant frequency and Q is the selectivity of the tuned circuit.

An experiment was set up to investigate this behaviour. The reference bridge capacitance ratio $C_6:C_5$ (Figure 3.1) was set to 0.2. A fixed amplitude signal at 10 kHz was fed into one input of the balance arm summer-driver. The sample bridge summer-driver was given no input. The amplitude at the reference bridge head amplifier output was measured using the low frequency detectors, for different capacitance ratios $C_6:C_5$ obtained by increasing C_6. The process was repeated at frequencies up to 100 MHz. Above 10 kHz, the reference bridge head amplifier output was measured using an oscilloscope. The amplitude data were normalised to account for the frequency dependence of the head amplifier. Figure 6.4 shows the normalised amplitude as a function of capacitance ratio at various frequencies. A least squares fit was performed to determine whether the behaviour at particular capacitance ratios conformed sufficiently to equation (6.3) at any of a number of trial resonant frequencies and Q factors. At the four highest capacitance ratios, resonances at 252, 261, 271 and 286 MHz were found, each giving mean of square deviations of less than 1% at five frequencies with an average Q of 107. If the capacitance C in equation (6.2) is 4 pF, which might correspond reasonably with the capacitance ratio of unity, and the resonant of frequency is 252 MHz, then the inductance L would be about 100 nH.

Q-meter measurements on a similar length of braid gave a resonance at 78 MHz and a Q of 120 when placed in series with 40 pF. That is an inductance of 104 nH, confirming the resonance explanation.

When used as a balanced bridge, the effective resonance is expected to be at somewhat lower frequencies than indicated above. In the arrangement described in this section, the capacitance to ground, as seen by the drive arm impedance, involves the two drive arm capacitances in series, if the detector input capacitance is ignored. However, when both summer-drivers are active and the bridge is balanced, each arm drive impedance will effectively see a capacitance to ground involving its own arm capacitance only since the balance point is then a virtual ground at the measurement frequency.

Unless steps are taken to reduce or compensate for the arm feed resonance, then errors may result in values of sample capacitance calculated using the method described in section 3.5.

6.3.4 Wideband head amplifier

The frequency response of the wideband head amplifier circuit, shown within the dashed box of Figure 4.19, was investigated by feeding a signal from a 50 Ω source into the gate of the translator

TR1 and comparing the input signal amplitude with that at the end of a 50 Ω terminated line fed from the head amplifier output. The voltage gain was about 0.8, varying between different MOSFETS, and was flat to about 70 MHz.

Although the head amplifer gain partially determines the bridge sensitivity, since a balance is sought, no errors are introduced through frequency dependent variations in the gain.

6.3.5 Measurements of Spectrometer Performance

6.3.5.1 Introduction

The spectrometer performance was assessed using PMMA and LDPE samples.

The PMMA sample, 14 mm by 20 mm in cross-section, was cut from a smooth sheet 1.55 mm thick and of commercial origin. A 1 mm hole was drilled through the centre. After cleaning with acetone, and drying, the sample was positioned in the sample cell and the vacuum applied. No intermediate conductors or pastes were used. The sample capacitance at 1 kHZ was about 0.63 pF. Preliminary tests were carried out on a PMMA sample of 1.3 mm thickness. An apparent anomaly in the measured capacitance at around 10 kHz could only be explained by a variation in sample temperature. The subsequent addition of a nitrogen boil-off pressure regulator (section 4.2), and optimisation of temperature control loop parameters, facilitated a more definitive set of measurements on the 1.55 mm sample.

Two LPDE samples were used. Both were about 13 mm by 20 mm in cross-section and 1.26 mm thick. A 1 mm hole was drilled in the centre of each sample. The samples were cleaned with 1,1,1-trichloroethane. One of the samples was inserted with no further preparation, the resulting capacitance at 1 kHz was about 0.56pF. An area on the surface of the second sample, about 17 mm by 10 mm, and centred on the hole, was coated with a thin gold layer by sputtering, and subsequently with aluminium by evaporation, to increase the effective sample capacitance to about 2.9 pF at 1 kHz. In order to get a good vacuum seal, it was necessary to anneal the LDPE samples at 90 °C for at least 5 minutes.

Attempts to increase the effective electrode area of an LDPE sample using silver dag paint were abandoned after d.c. measurements across the surface revealed uneven contact. The direct evaporation of aluminium resulted in a weakly bonded layer of inconsistent contact resistance. The intention was to measure the impedance of the plated sample over the whole frequency range. However, having performed measurements between 0.1 Hz and 20 kHz, followed by measurements between 3×10^{-4} Hz and 0.1 Hz, mechanical stress had resulted in cracking of the plated surface. Subsequent measurements above about 500 Hz showed a variable electrode loss. The impedance of the unplated sample was measured between 5 kHz and 100 MHz to complete the data set.

6.3.5.2 High frequency performance

At frequencies between 20 kHz and 10 MHz, a minimum loss angle resolution of 5×10^{-4} rads could be achieved, which is within the design specification. Above 10 MHz, the minimum loss angle resolution increased progressively to about 2×10^{-3}rads at 100 MHz. The performance limit resulted particularly from the small operating capacitances of both sample and reference bridges and from harmonic effects.

An examination of the waveshape at the outputs of the oscillators and phase-splitters indicated the presence of second harmonics with an amplitude less than a few percent of the fundamental amplitude, over most of the frequency range. However, between 40-70 MHz, an increase in second harmonic content beyond this level resulted from a peculiarity in the VMOS transistor. Typically, the distortion at the summer-driver outputs, resulting from both oscillators and summer-drivers, was below a few percent.

The second harmonic at the bridge balance point caused two problems. The dynamic range of the detectors was reduced; often preventing the use of the correlators without the prior insertion of an attenuator between the head amplifier output and detector input. Both the magnitude detectors and the correlators responded, to a noticeable extent, to the harmonics. The r.m.s. noise level at the detector input was equivalent in magnitude to 1 mV of signal at the input, as measured by the magnitude detector. The correlator sensitivity was about 100 $\mu V(H_z)^{-\frac{1}{2}}$.

The effect of the reference bridge resonance phenomenon, described in section 6.3.3, was minimised by making the sample and balance capacitances as identical as possible and by operating the reference bridge with the minimum arm capacitances at frequencies above 10 MHz. The latter precaution moved the resonance to the highest possible frequencies, although the bridge sensitivity was reduced significantly. The alignment of the 0° and the 180° signals was estimated from the minimum detectable loss tangent to be within 0.05° below 10 MHz, rising to about 0.5° at 100 MHz. The phase alignment of the 90° signal was estimated to be within about 5°, resulting in an additional uncertainty of about 0.5% in the loss tangent.

The capacitances of the samples were about 0.5 pF above 20 kHz. The measurement resolution was about 1 fF or 0.2%. It is expected that, for 3 pF samples (the design choice) and with similar capacitances in the reference bridge arms, the capacitance resolution could be substantially improved.

The time taken for a single frequency measurement varied with frequency but was typically 30 minutes.

6.3.5.3 Low frequency performance

At frequencies between 0.1 Hz and 10 kHz, a minimum loss angle resolution of about 10^{-4} rads could be achieved, being below 3×10^{-5} rads for much of the range. The minimum resolution at 20 kHz was about 2×10^{-4} rads as a result of the reduced number of phase increments per cycle. The sample capacitance could be determined to about 0.05%.

Each element performed within, or better than, the design specification. The waveform distortion due to the waveform synthesizer was minimal after clock frequency glitches had been filtered out.

The detector sensitivity was about 50 $\mu V(H_z)^{-\frac{1}{2}}$ for most of the range.

The measurement time for a single frequency measurement varied between 15 and 20 minutes.

Measurements on the standard bridge were consistent to about 0.05%.

6.3.5.4 VLF performance

VLF measurements were made between 3×10^{-4} Hz and 0.1 Hz. Below 10^{-2}Hz, only one pre-cycle and one post-cycle were used. A balance to below 1 mV could normally be achieved by taking four measurements, that is eight cycles, from which a further iteration in software could produce readings with a loss angle resolution of 3×10^{-4} rads.

At frequencies below 10^{-2}Hz, accumulation of charge at the balance point gave rise to a continuous positive voltage ramp at the detector input, as can be seen in Figure 6.5. The ramp rate varied considerably from day to day. After ruling out charge injection from the circuitry, it was postulated that the charge accumulation was due to the collection of positive ions from the air. Two subsequent tests confirmed the postulate. By feeding a continuous flow of dry, oxygen free nitrogen through the sample cell, via the environmental control stainless steel feeders, and through the detector head amplifier housing, the rate of charge accumulation was significantly reduced, as can be seen in Figure 6.6. Further confirmation was obtained by placing a domestic negative ioniser in the vicinity of the detector. Within minutes a dramatic reversal of the ramp voltage was observed; this can be seen in Figure 6.7.

The conversion efficiency of the parametric modulator was below 10%. Attempts to improve the efficiency by increasing the loudspeaker drive current had two effects. For large increases in drive current, the modulated waveform became peculiarly distorted suggesting the excitation of other modes in the loudspeaker cone. For smaller increases in drive current, a general increase in modulator noise, particularly between 10 Hz and 0.1 Hz, occurred, possibly as a result of ions generated locally by the action of the cylindrical brass ring forming the bottom electrode, moving quickly through the surrounding air.

Attempts at the further optimisation of the integral feedback loop, providing the VLF bootstrap, by the addition of proportional and derivative terms only resulted in destabilisation. This was

Fig 6.5 Semple Bridge balence point voltage in the presence of air

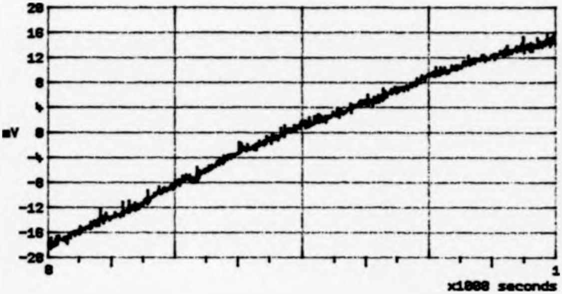

Fig. 6.6 Semple Bridge balence point voltage in the presence of dry nitrogen

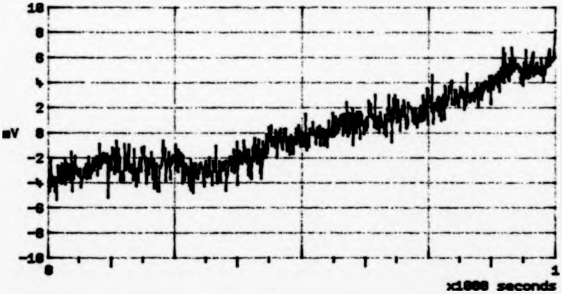

Fig. 6.7 Sample Bridge balance point voltage in the presence of a negative ion source

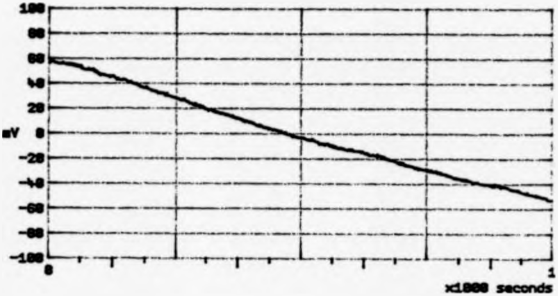

partially due to breakthrough of the second harmonic of the modulator frequency from the multiplier output, but, more significantly, a result of the modulator noise which was otherwise largely filtered out by the integrator time constant.

The bootstrapping of the detector feed impedance, at VLF, by feeding the integrator output to the second inner of the detector feeder, was abandoned. The second inner was sufficiently coupled to the signal inner that a separate positive feedback path was introduced which was sufficient to de-stabilise the loop.

Apart from charge accumulation at the balance point, the effects of which could be largely removed by software, the signal-to-noise ratio did not seem to worsen with decreasing frequency. Any increase in flicker noise, or loss of sensitivity must therefore have been offset by the increase in signal period and hence in measurement time. Thus, it is expected that as long as the detector dynamic range is not exceeded, operation at frequencies lower than 3×10^{-4} Hz, and probably below 10^{-5} Hz, ought to be possible.

The PMMA test sample has a measured capacitance of 0.930 pF and an equivalent parallel resistance of 1.44×10^{16} Ω at 3×10^{-4} Hz. At the same frequency, the capacitance of the plated LDPE sample was measured to be 2.951 pF with an equivalent parallel resistance of 4.02×10^{16} Ω. Measurements of such high resistances normally require the highest precision electrometers.

At the lowest frequencies (≤ 1 mHz), the balance point was often discharged prior to measurement. However, it was later discovered that, due to a mechanical maladjustment, the discharging operation sometimes altered the position of the outer of the balance capacitor. It became necessary, therefore, to re-balance the bridge at a higher frequency, to determine the actual sample impedance.

6.3.6 Dielectric properties of PMMA at 35°C

The real and imaginary parts of the relative permittivity of PMMA, as derived from measurements of the sample impedance, are shown plotted in Figures 6.8 and 6.9 respectively. A scaling factor, based on published measurements (82), has been used to convert capacitance to permittivity. The loss tangent (uncorrected) is shown in Figure 6.10. Figure 6.11 shows the loss tangent derived from a transformation of the sample capacitance using the method of Lynch (7).

The data below 10^7 Hz accord broadly with those reported by Pratt and Smith (83). The broad peak in $\tan\delta$, centred on 100 Hz, corresponds to the β-relaxation, which is widely thought to result from the motion of the ester side group interacting with the main polymer chain (84), (85) and (86). The molecular structure of PMMA is shown in Figure 6.12.

An additional process is superposed on the high frequency tail of the β-relaxation. Although PMMA is known to exhibit high frequency relaxation due to rotation of the two methyl groups (28), (87), the extremely low intensity and short relaxation times associated with these processes suggest that another agency is involved. PMMA may contain up to about 5% of trapped water, which, when bonded to the polymer matrix, may result in dielectric loss over a wide frequency range, although, at 35 °C, the relaxation time is most likely to be around 10^{-8} seconds (28). The common addition of polar additives, such as dibutyl phthalate (DBP) or hexachloroendomethylenetetrahydropthalic acid 1,2-propane diol (HET-1, 2-PD) will certainly result in modifications of the dielectric behaviour. (Sreehari Sastry et al. (88) have reported a considerable polarisation loss rising between 10 kHz and 100 kHz

Fig. 6.8 Frequency Dependence of ε' for PMMA at 35 °C

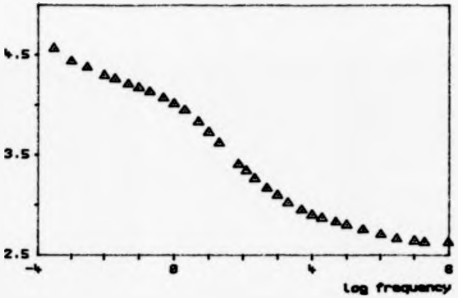

Fig. 6.9 Frequency Dependence of ε" for PMMA at 35 °C

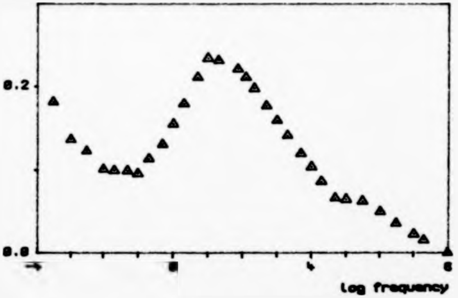

Fig. 6.10 Frequency Dependence of tanδ for PMMA at 35 °C

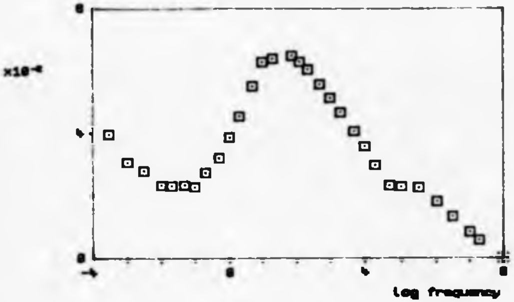

Fig. 6.11 Derivation of tanδ from ε' for PMMA at 35 °C

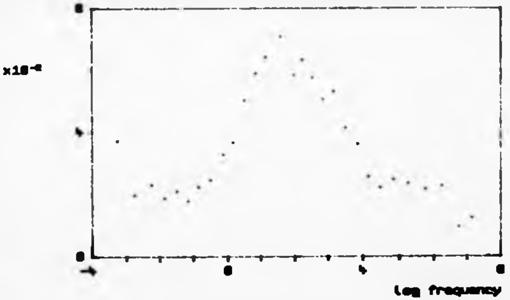

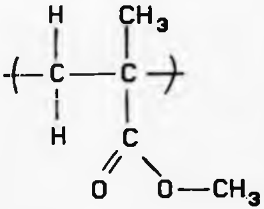

Fig. 6.12 Repeat Unit of Poly(methylmethacrylate) Structure

which is dependent on the concentration of MET-1, 2-PD in a PMMA blend.) A more definitive identification of the process could be made through a determination of the activation energy, and by cooperation with the manufacturer.

The increase in tanδ at VLF is thought to be due to a Maxwell-Wagner-Sillars type polarisation process, which, according to Pratt and Smith (83), results from small, ordered domains within a predominantly amorphous environment. Further evidence of domains in PMMA has been presented elsewhere (89), (90). Figure 6.11 indicates that the loss tangent rise at low frequency is in accordance with the change in ε', which is evidence for a very high d.c. resistivity.

It is interesting to compare the ε'' behaviour with that reported by Reddish (91) over the frequency range 10^{-4} Hz to 1 MHz and at 35°C. Figure 6.13 shows the variation of ε'' for both data sets; also shown is that derived from preliminary measurements on the 1.3 mm thick sample. The positions of the β-peak are similar in all cases, although the peak intensity measured using the spectrometer is lower and more similar to that found by Scheiber (92); the difference probably resulting from additive effects. (Toluene plasticiser is known to increase the β-intensity (28); whilst DBT can have the reverse effect (93).)

At VLF, measurements on the 1.3 mm thick sample show a sharp rise in ε'' with decreasing frequency. Analysis of the simultaneous behaviour of the sample capacitance indicates that a d.c. conduction process is largely, but not completely, responsible for the rising loss, contributing by about 1.4×10^{-4}/frequency at each point. The corresponding d.c. resistance is about $3.2 \times 10^{15}\ \Omega$, that is a resistivity of about $10^{13}\ \Omega$m, which is consistent with that reported by Pratt and Smith (83). Pratt and Smith have also shown that the additive triallyl cyanurate (TACN) and radiation induced cross-

Fig. 6.13 Comparison of Measurements of ε"
for PMMA at 35 °C

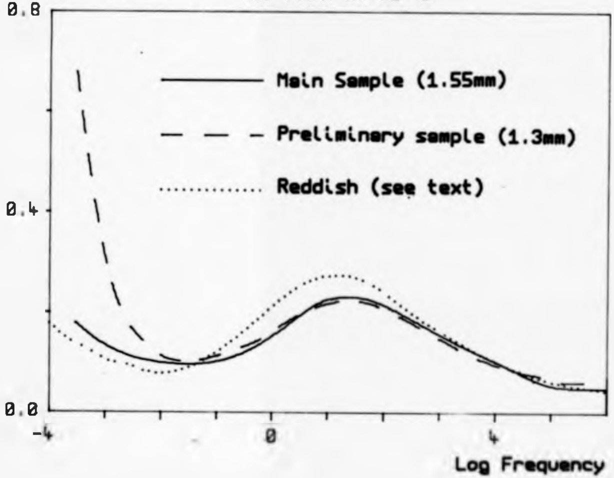

linking can increase the conductivity of PMMA (83). No d.c. correction has been performed on the data presented by Reddish and no real part is given, although it is apparent from comments made that the sample conductivity is low (91). Reddish states that "conduction is only encountered at low frequencies and high temperatures as a dominant mechanism" (91) and, that, in other frequency and temperature regions, "relaxation phenomena predominate" (94). The implication being that the rising loss presented by Reddish is due, at least in part, to a relaxation process.

The existence of long term processes in PMMA is also implied in the facts that it took Pratt and Smith several hours to measure the d.c. conductivity (95), and that data presented by Hall (82), and described as resistivity, show an increase even after 1000 seconds of measurement time. It is expected that both the low frequency polarisation and the d.c. conductivity will vary between samples, since influencing factors such as crystallinity, impurity concentration and additives differ between manufacturers and batches.

6.3.7 Dielectric properties of LDPE at 30°C

The real and imaginary parts of the relative permittivity of LDPE, as derived from measurements of sample impedance, are shown in Figures 6.14 and 6.15 respectively. A scaling factor was obtained from published data (82). The loss tangent (uncorrected) is shown in Figure 6.16. The figures are constructed from two sets of data, the first from 3×10^{-4} Hz to 5 kHz as measured on the plated sample, the second from 5 kHz to 100 MHz as measured on the unplated sample. The data sets were matched at 5 kHz to ensure that the transition from the low to high frequency regime at 20 kHz took place on one sample. The 20 kHz point for both samples has been plotted.

Fig. 6.14 Frequency Dependence of ε'
for LDPE at 30 °C

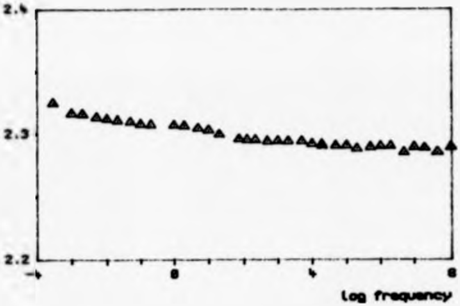

Fig. 6.15 Frequency Dependence of ε"
for LDPE at 30 °C

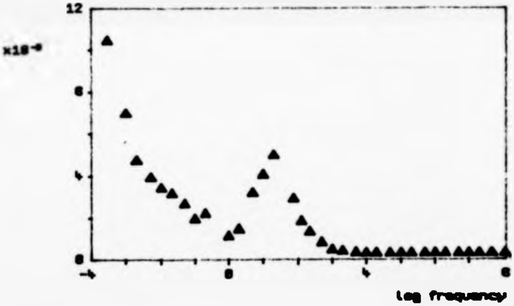

Fig. 6.16 Frequency Dependence of tanδ for LDPE at 30 °C

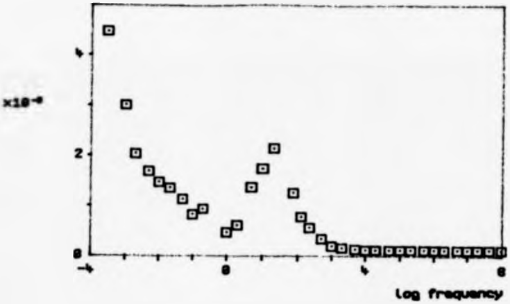

Fig. 6.17 Repeat Unit of Poly(ethylene) Structure

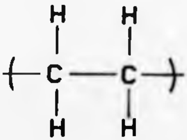

$$\left(-\mathrm{CH_2}-\mathrm{CH_2}- \right)$$

Above 20 kHz, the measured loss tangent values lie below 5 x 10^{-4} which is the sensitivity limit. Since it is impossible to justify any detail within this region, a mean value of 1.2 x 10^{-4} has been shown. At 40 MHz, the sensitivity falls to about 10^{-3} reaching about 2 x 10^{-3} at 100 MHz. The scatter in the real part is about 0.2% on a 0.53 pF sample.

The structure of polythene is shown in Figure 6.17. Although nominally apolar, permanent dipole moments are introduced through occasional methyl and ethyl groups, 1.5 and 14.4 respectively per 1000 carbon atoms in LDPE and through oxidation (28).

The fairly narrow peak centred on about 30 Hz in figures 6.14 and 6.15 is identified with the α-relaxation (28), (97). X-ray (98), NMR (99) and microscopic studies (100) have shown that polyethylene consists of a combination of amorphous and crystalline regions. The α-relaxation has been shown to result from relaxations in the crystallites (101), (102), (103) and is enhanced by oxidation associated with these regions (104). Tests performed prior to annealing indicated a loss peak at much the same frequency, although of about one third of the intensity. This is consistent with an increase in crystallinity following annealing (98), (105).

The rising loss at VLF is consistent with interfacial polarisation between crystalline and amorphous regions. Fourier transform measurements have shown that the peak intensity is strongly dependent on oxidation (28). No significant d.c. conductivity can be discerned from the measurements presented in Figures 6.13 and 6.14.

Although no precise form can be given, there is evidently a weak loss process between 10 kHz and 100 MHz. LDPE is known to exhibit β-relaxation, due to the rotation of alkyl groups (106), in this frequency region. The β-intensity depends strongly on oxidation levels (104). A γ-process is active between about 1 MHz and 10 GHz

(107), (108). The γ-process is the dominant mechanism, the loss tangent rising from 1 MHz to 100 MHz and reaching anywhere between 10^{-4} and 10^{-2}, depending on sample oxidation (108), (109). In view of the small change in the real component of Figure 6.14 between 10 kHz and 100 MHz, it is unlikely that the corresponding loss tangent exceeds 5×10^{-4}.

6.4 CONSIDERATION OF ABSOLUTE ACCURACY

6.4.1 Calculation of ε'

It has been stated previously that, at this stage of development, the absolute measurement of permittivity is not a primary objective. Nevertheless, the sample cell has been designed such that fringing fields pass mainly through the sample material enabling a simple scaling factor, determined at one frequency, to be used to convert sample capacitance to permittivity. However, the existence of a hole of about 3% of the effective sample area (if plating is not used) will result in a measured capacitance of which typically about 1%, depending on sample permittivity, is not due to the sample material.

If the measured capacitance, at which the scaling factor was determined, is C_{ref}, and the part of this not due to the sample is ΔC, then, at any other measured capacitance C_m, the permittivity calculated from the scaling factor will be in error by a factor:

$$(1-\Delta C/C_{ref})/(1-\Delta C/C_m) \qquad (6.4)$$

This may be insignificant for materials where the capacitance is fairly constant with frequency. For a sample capacitance which becomes twice that at which the scaling factor was determined, an error of about $\Delta C/2C_{ref}$, typically 0.5%, will occur in the calculated permittivity. Although this may still be unimportant, a correction can be made through an estimation of the capacitance ΔC. The capacitance due to the hole is readily calculable to within 10%, since the geometry is straightforward. Alternatively, if the loss tangent measured with the capacitance C_{ref} is $\tan\delta_{ref}$, and if the actual loss tangent at this frequency is $\tan\delta$, then:

$$\Delta C = C_{ref}(1-\tan\delta_{ref}/\tan\delta) \qquad (6.5)$$

If the measurement precision at high frequencies is equivalent to about 1fF in sample capacitance, or about 0.05% for a typical sample, and a similar precision is achieved over the low frequency range, then a scaling factor between sample capacitance and permittivity determined from a measurement at such a frequency should be accurate to 0.05% if the permittivity reference data is without error. Any subsequent measurement based on the scaling factor will be subject to this error, and the error due to its own uncertainty, combined with any error resulting from equation (6.4). If the latter is restricted to 0.1% by estimation of ΔC, then calculations of permittivity accurate to within 0.2% (typically 0.12%) should be possible over the low and high frequency regions and within 0.25% (typically 0.15%) over the VLF region. If a change in temperature requires a balance of the standard bridge, then an additional uncertainty of 0.05% will be introduced as a result of the standard bridge balance.

6.4.2 Calculation of tanδ

The measured value of tanδ will be typically 1% lower than it should be as a result of ΔC. Through an estimation of ΔC, the uncertainty ought to be reducible to 0.1%. At low frequencies and at VLF there is no other apparent systematic error, any error in tanδ results from the precision limit. At low frequencies this is typically 10^{-4} and at VLF about 3×10^{-4}.

At frequencies above 20 kHz, a basic uncertainty of 5×10^{-4} arises from the misalignment of 0° and 180° signals and the detector sensitivity. There is also an uncertainty in tanδ of about 0.5%

which is due to misalignment of the 90° signal. It was seen in section 6.3.2.4 that intermodulation effects in the summer-drivers may lead to an exaggeration of tanδ of up to about 1.5% unless corrections are made. There may also be an error estimated at 1% due to the measurement of actual attenuation described in section 3.5.3. At this stage, therefore, the uncertainty in tanδ above 20 kHz is maximally about 3.1% with an additional 5×10^{-4}.

6.5 IMPROVING THE SPECTROMETER PERFORMANCE

6.5.1 General

The sample bridge sensitivity will be improved, according to equation (3.1), if a higher sample capacitance is used. Measurement precision will, therefore, improve if the design 3 pF samples are used. If a lower maximum frequency is required, say 10 MHz, where there is not such a drive impedance limitation, higher capacitances may be beneficial, although once the detector input capacitance is exceeded, the sensitivity increases only slightly with bridge arm capacitance. There may also be a difficulty in constructing a suitable balance capacitor.

Adaptation of the spectrometer for three-terminal measurements is under consideration.

6.5.2 High frequency

The use of active summer-drivers will always result in harmonic distortion at the bridge even if improvements are made to the oscillators. The dynamic range of the detectors could be improved considerably by the use of discrete devices. The sensitivity of the detectors to harmonics can be reduced greatly by the use of passive tuned circuits.

The reference bridge arm feed inductance may be reduced by adding extra braid in parallel with the existing connection. A more effective solution would be to replace the braid by a flexible co-axial feeder, or at least a feeder with some capacitance distributed along its length. A length of insulated braid sandwiched between two nominally-earthed outer lengths is being considered.

It is expect that, by such means, the resonance problem can be essentially removed. If, however, any slight difficulty remains, a correction database could be established.

The uncertainty in the loss tangent resulting from non-linear effects in the summer-drivers may be reduced very significantly by an alteration to the method of comparing the 90° and 180° amplitudes outlined in section 3.6.3. The following procedure is suggested:

(i) With the reference bridge capacitors in the 0°, 180° balance position, all phases are switched in.

(ii) The magnitude at the balance point is recorded. This is due to the 90° component only, though still measured in the presence of the 180° signal at the balance arm summer-driver.

(iii) The 90° signal is removed, and the 180° signal is adjusted, in a convenient direction, to produce the same magnitude of out-of-balance signal at the detector.

(iv) The capacitors are moved to re-balance the reference bridge.

(v) Both the previous capacitance ratio and that after step (iv) are measured at 175 Hz and are represented by A1 and A2 respectively.

(vi) The 90°:180° ratio is now given by |A1-A2|/A1

No assumptions of detector or summer-driver linearity are made, neither is any d.c. measurement of high frequency attenuators involved. Thus the greatest sources of loss tangent uncertainty can be removed.

6.5.3 VLF

The effects of externally generated positive ions could be neutralised by feeding an equal number of negative ions into the sample cell and detector environment. Experiment has shown that it is possible to control the rate of charge accumulation through the negative ionisation of an incoming nitrogen flow. With the addition of a separate ion sensor and ioniser, an automatic feedback system could be established.

The parametric modulator efficiency can only be improved by increasing the depth of capacitance modulation. With the restricted upward movement of the loudspeaker, the most effective means of implementing a large fractional capacitance change is to replace the present cylindrical arrangement with a closely-spaced parallel plate geometry, where the capacitance is inversely proportional to the plate separation. However, the profile of the parallel plate is more likely to disturb the surrounding air resulting in a higher noise. A practical parallel plate modulator might therefore have to be operated in a vacuum.

If only VLF measurements are required, a slight increase in sensitivity, and a significant isolation from the effects of ion injection, could be gained by an increase in sample capacitance, although the sample cell and balance capacitor arrangement would need alteration.

6.6 CONCLUDING REMARKS

The spectrometer has been shown to be capable of measuring the impedance of dielectric samples over the frequency range of 3×10^{-4} Hz to 10^{8} Hz. A further extension of the lower frequency limit is expected. The temperature control system has been tested successfully over the temperature range of −180 °C to +350 °C.

The minimum loss angle resolution between 20 kHz and 10 MHz is 5×10^{-4} rads, and rises to about 2×10^{-3} rads at 100 MHz. A capacitance resolution of about 1 fF has been demonstrated over this range. A voltage magnification effect due to a resonance in the reference bridge drive arms has been identified, and a solution proposed which should improve the spectrometer performance at the highest frequencies. It has been suggested that the effectiveness of the detectors may be enhanced by the use of discrete devices and by tuning. The absolute accuracy of permittivity, derived from measurements over the high and low frequency ranges, with suitable scaling, is within 0.2%. An uncertainty of up to about 3.1% in the loss tangent above 20 kHz should be improved substantially by an enhancement of the measurement algorithm.

Between 0.1 Hz and 10 kHz, the minimum loss angle resolution is typically 10^{-4} rising to about 2×10^{-4} at 20 kHz. Within this frequency region, all components exceeded the design specification.

Between 3×10^{-4} Hz and 0.1 Hz, the minimum loss angle resolution is typically 3×10^{-4} rads for measurements taking only eight cycles. Measurements of capacitance can be made to 0.1%. No significant degradation is observed with decreasing frequency, suggesting that even lower frequencies may be reached. Improvements to the VLF system could be made by controlling the atmospheric ion content and by increasing the conversion efficiency of the parametric modulator. The effect of atmospheric ions would be less significant if a higher sample capacitance were used.

Measurements performed on samples of PMMA and LDPE are consistent, within the spectrometer precision and material variation, with published data.

CHAPTER 7

Summary and Conclusions

Dielectric relaxation occurs between very low and microwave frequencies. Dielectric measurements within this frequency range, and at various temperatures, provide information on molecular and segmental motion and on the morphology of materials. The existence of a large number of empirical and theoretical models indicates that dielectric relaxation processes are insufficiently understood and in need of further theoretical and experimental investigation.

Dielectric relaxations are often broadband in character. The response of dielectric materials commonly results from a convolution of relaxations and, therefore, can cover an extremely wide frequency range. Complete characterisations of such materials must, therefore, involve wideband measurements. Information about phase transitions and the identity of particular processes can be gained from dielectric measurements over a range of temperatures.

Single techniques for the measurement of permittivity cover typically only four or five decades in frequency. Studies of dielectric response, therefore, often require a change of measuring technique. The adoption of a single technique which could cover at least twelve decades in frequency would avoid some of the difficulties and inconvenience associated with a change of method. The frequency region with the greatest potential for exploitation over a wide range may be found below about 300 MHz, where, for most samples, the lumped impedance approximation is valid.

Wideband methods for the measurement of dielectric properties below 300 MHz involve the direct measurement of electrical impedance. Following an examination of the wideband potential of different impedance measuring schemes, it is concluded that the optimum arrangement for the central element of a wideband subgigahertz dielectric spectrometer is the voltage balanced 2-arm capacitance bridge.

The design of a spectrometer, covering the ranges -180 °C to +600 °C and 10^{-5} Hz to 10^{8} Hz has been described, and is based on three 2-arm capacitance bridges; the sample, reference and standard bridges. An air-gap balance capacitor and a 2-terminal capacitor formed by the sample constitute the sample bridge. Feeder impedance and detector output impedance set the optimum sample capacitance at 3 pF, although, at frequencies below 10^{8} Hz, higher capacitances may be used. Both elements of the sample bridge are enclosed in a cell, the temperature of which is varied by an external nitrogen gas flow. The reference bridge, which is constructed from two variable air-gap capacitors and arranged to be electrically in parallel and spatially close to the sample bridge, is used in the phase alignment of the bridge drive signals. The standard bridge is formed between the sample bridge balance capacitor and a standard capacitor situated outside the sample cell and permits monitoring of the balance capacitor at a calibration frequency.

The bridge arm drive signals are generated, above 20kHz, by two oscillators phase-locked in quadrature. Admixtures of the primary phases are summed in specially constructed, multiple-input bridge drive amplifiers to provide signal sources of variable amplitude and phase. At lower frequencies, a high precision, RAM-based digital waveform synthesiser provides the bridge drive signals.

Wideband amplifiers at the balance point of each bridge feed high sensitivity correlation detectors. Below 5 Hz, a parametric modulator is used to maintain a high resistive input impedance and to minimise the presence and effects of very low frequency noise.

The spectrometer is managed by a BBC model B microcomputer. A parallel bus system links the microcomputer, via a memory mapped interface, to the various elements, or hardware units, of the spectrometer. Computer accessing time is minimised by making those units which perform long sequential operations self-timed.

The acquisition, processing and storage of data are governed by hierarchically structured software. At the lowest software level, hardware is accessed by assembled machine code stored in a number of 16k byte ROMs within the microcomputer. At the highest level, sequences of menu options execute intermediate level BASIC routines loaded from ROMs or floppy discs.

The temperature variation scheme has been tested successfully over the range of -180 °C to +350 °C. The electrical performance of the spectrometer has been determined over the frequency range of 3×10^{-4} Hz to 10^{8} Hz.

Between 20 kHz and 10 MHz, a minimum loss angle resolution of 5×10^{-4} rads could be achieved, rising to 2×10^{-3} rads at 10^{8} Hz. The capacitance resolution is about 1fF or 0.2% for a sample capacitance of 0.5 pF: the percentage resolution should be enhanced for a 3 pF sample. The performance at the highest frequencies is expected to improve after a reduction of the inductance in the reference bridge feed connections. The absolute uncertainty of about 3.1% in the loss tangent at frequencies above 20 kHz should be reduced substantially by a change in the measurement algorithm.

Between 0.1 Hz and 10 kHz, a typical loss angle resolution of 10^{-4} rads has been achieved, rising to about 2×10^{-4} rads at 20 kHz.

The measurement of sample impedance over this region is to within 0.05%.

Below 0.1 Hz, the loss angle resolution is about 3×10^{-4} rads for measurements taking typically eight periods of the measurement frequency, with an impedance resolution of about 0.1%. The low frequency limit for sample capacitances of about 3 pF is expected to be determined by atmospheric ion concentrations, unless additional environmental controls are implemented. The use of a parametric detector system appears to have reduced the effects of flicker noise, and should, therefore, enable an extension of the spectrometer operation to even lower frequencies.

Measurements on samples of poly(methylmethacrylate) and low density polyethylene have been performed at 35°C and 30°C respectively. The measurements are consistent, within the spectrometer precision and material variation, with published data. Interpretations are given, where possible, of the processes encountered.

Over most of the frequency range investigated, the spectrometer performance is within or exceeds the design specification. To the best of the author's knowledge, no other single dielectric measuring technique has exceeded the frequency capability of the instrument described. The spectrometer has been shown to be capable of operating with a sample capacitance as low as 0.5 pF, which is significantly less than most other techniques, and might, therefore, lead to applications in other areas.

REFERENCES

1. Kittel, C., 'Introduction to Solid State Physics', John Wiley and Sons Inc: N.Y., (1976).

2. Balkanski, M., (Ed.) 'Light Scattering in Solids', Flammarion, Paris, (1971).

3. Frohlich, H., 'Theory of Dielectrics', Clarendon, Oxford, (1958).

4. Debye, R., 'Polar Molecules', Chemical Catalog Co.: N.Y., (1947).

5. Coelho, R., 'Physics of Dielectrics for the Engineer', Elsevier: Amsterdam, (1979).

6. Davidson, D.W., Can. J. Chem., 39 (1961).

7. Lynch, A.C., Proc. IEE, 118, 1, (1971).

8. Bottcher, C.J.F. and Bordewijk, P., 'Theory of Electric Polarisation', Vol. II, Elsevier: Amsterdam, (1979).

9. Cole, R.H., Inst. Phys. Conf., ser. 58, (1980).

10. Cole, K.S. and Cole, R.H., J. Chem. Phys., 9, 341, (1941).

11. Davidson, D.W. and Cole, R.H., J. Chem. Phys., 18, 1950, (1950).

12. Havriliak, S. and Negami, S., J. Polym. Sci. C., 14, 99, (1966).

13. Williams, G. and Watts, D.C., Trans. Faraday Soc., 66, 80, (1970).

14. Fuoss, R.M. and Kirkwood, J.G., J. Am. Chem. Soc., 63, 385, (1941).

15. Jonscher, A.K., Colloid and Polym. Sci., 253, 231, (1975).

16. Hill, R.M., Nature, 275, 96, (1978).

17. Kubo, R., J. Phys. Soc. Japan, 6, 570, (1957).

18. Glarum, S.H., J. Chem. Phys., 33, 639, (1960).

19. Philips, M.C., Barlow, A.J. and Lamb, J., Proc. Roy. Soc. London, A., 329, 193, (1972).

20. Bordewijk, P., Chem. Phys. Letters, 32, 592, (1975).

21. Hunt, P.I. and Powles, J.G., Proc. Phys. Soc., 88, 513, (1966).

22. Anderson, J.E. and Ullman, R., J. Chem. Phys., 47, 2178, (1967).

23. Shore, J.E. and Zwanzig, R., J. Chem. Phys., 63, 5445, (1975).

24. Jonscher, A.K., Nature, 267, 673, (1977).

25. Jonscher, A.K., Inst. Phys. Conf. Ser. 58, (1980).

26. Anderson, J.E., J. Chem. Phys., 52, 2821, (1970).

27. Pratt, G.J. and Smith, M.J.A., Br. Polym.J., 18, 105, (1986).

28. Hedvig, P., 'Dielectric Spectroscopy of Polymers', Adam Hilger: Bristol, (1977).

29. Pratt, G.J. and Smith, M.J.A., Polymer, 30, 1113, (1989).

30. Baker, E.B., Rev. Sci. Instrum., 20, 716, (1949).

31. Cross, L.E., 'Dielectric Measurement Techniques', Pennsylvania State University, (1966).

32. Lynch, A.C., IEEE Trans. Instr. and Meas., IM-23, 425, (1974).

33. Afsar, M.N., Birch, J.R. and Clarke, R.N., (Ed. Chantry, G.W.), Proc. IEEE, 74, 183, (1986).

34. Roberts, S. and von Hippel, A., J. App. Phys., 17, 610, (1946).

35. Stuchly, M.A. and Stuchly, S.S., IEEE trans. Instrum. and Meas., IM-29, 176, (1980).

36. Waldron, R.A., 'The theory of Waveguides and Cavities', Maclaren and Sons" London, (1967).

37. Cook, R.J. and Rosenberg, C.B., IEE Conf. 129, 22, (1977).

38. Lynch, A.C. and Ayers, S., Proc. IEE, 119, 767, (1972).

39. Redheffer, R.M., 'Technique of Microwave Measurements' (Ed. Montgomery, C.G.I., McGraw-Hill, N.Y., (1947).

40. Bansal, R. and Khan, S., IEE conf. 289, 167, (1988).

41. '1255 HF Frequency Response Analyser, Solartron Instruments, Farnborough, Hampshire, UK, (1987).

42. Hanscomb, J.R. and Kaahwa, Y., J. Phys. E., 11, 406, (1987).

43. Hamon, B.V., Proc. IEE, 99, 151, Part, Mon. 27, (1952).

44. Hyde, P.J., Proc. IEE, 117, 1891, (1970).

45. Odianov, V.L. and Gusev, Yu, A., Pribory i Tekhnika Eksperimenta, 6, 114, (1986).

46. Chowdhry, B.S., Shahi, S.S. and Brignell, J.E., IEE conf. 289, 293, (1988).

47. Hayward, D., Gawayne, M., Mahboubian-Jones, B. and Pethrick, R.A., J. Phys. E., 17, 683, (1984).

48. Kaatze, U. and Giese, K., J. Phys. E., 13, 133, (1980).

49. 'Chelsea Dielecric Interface' (specification sheet), John Pugh Dielectric Instrumentation, The Old Police Station, Holt Heath, Worc., UK, (1988).

50. Gabrielli, C., 'Identification of Electrochemical Processes by Frequency Response Analysis', Solartron Instrumentation Group, Farnborough, Hampshire, UK, (1980).

51. Dunmur, D.A., Hitchen, D.A. and Matnerfield, M.R., J. Phys. E., 20, 866, (1986).

52. Kent, M., J. Phys. E., 13, 457, (1980).

53. Lortz, W., Osswald, W., Kelemen, G. and Schon, G., J. Phys. E., 22, 293, (1989).

54. Hartshorn, L. and Ward, W.H., J. IEE, 79, 597, (1936).

55. Barrie, I.T., Proc. IEE, 112, 408, (1965).

56. Reddish, W., Bishop, A., Buckingham, K.A. and Hyde, P.J., Proc. IEE 188, 255, (1971).

57. Kakimoto, I., Etoh, A., Hirano, K. and Nonaka, S., Rev. Sci. Instrum., 58, 269, (1987).

58. Benadda, M.D., Curru, J.C. and Druon, C., J. Phys. E., 15, 132, (1982).

59. Savant, C.J., Roden, M.S. and Carpenter, G.L., 'Electronic Circuit Design-An Engineering Approach', Benjamin/Cummings: California, (1987).

60. Courteau, R. and Bose, T.K., Rev. Sci. Instrum., 58, 1096, (1987).

61. Hague, B., 'Alternating Current Bridge Methods', Pitman: London, (1957).

62. Head, J.G., White, N.M. and Gale, P.S., IEE Conf. 289, 61, (1988).

63. Jones, R.N., 'The Measurement of Lumped Parameter Impedance: A Metrology Guide', NBS Monograph 141, US Govt. Printing Office, (1974).

64. Thompson, A.M., Proc. IEE, 103B, 704, (1956).

65. Van Roggen, A., In International Microsymposium on Polarisation and Conduction in Insulating Materials, Bratislava, Harmonia, (1972).

66. Cavicchi, R.E. and Silsbee, R.H., Rev. Sci. Instrum., 59, 176, (1988).

67. Edmonds, I.R. and Smith, M.J.A., J. Phys. E., 5, 1067, (1972).

68. Pratt, G.J. and Smith, M.J.A., J. Phys. E., 15, 927, (1982).

69. Lynch, A.C., Proc. IEE, 124, 188, (1977).

70. Bleaney, B.I. and Bleaney, B., 'Electricity and Magnetism', O.U.P., (1978).

71. Kibble, B.P. and Rayner, G.H., 'Coaxial AC Bridges', Adam Hilger: Bristol, (1984).

72. Foote, M.C. and Anderson, A.C., Rev. Sci. Instrum., 58, 130, (1987).

73. Bikulov., A.F. and Frolov, P.M., Izmeritel'naya Tekhnika, 5, 643, (1968).

74. Pratt, G.J. and Smith, M.J.A., IUPAC-AAS-RACI Reprints Polymer 85, 1, 88, (1985).

75. Robinson, F.N.H., 'Noise and Fluctuations in Electronic Devices and Circuits', Clarendon Press: Oxford, (1974).

76. Wilmshurst, T.H., 'Signal Recovery from Noise in Electronic Instrumentation', Adam Hilger, Bristol and Boston, (1985).

77. R.S. Technical Data Library, Data Sheet 4434, RS Components Ltd., Duddeston Mill Ind. Est., Duddeston Mill Road, Saltley, Birmingham, UK, (1985).

78. Siliconix Integreated Circuits Data Book, 3-26, Siliconix Inc., Larelwood Rd., Santa Clara, U.S.A., (1985).

79. Chang, S.S.L., 'Synthesis of Optimum Control Systems', McGraw-Hill, N.Y., (1961).

80. Malmstadt, H.V., Enke, C.G. and Toren, E.C., 'Electronics for Scientists', W.A. Benjamin: N.Y., (1963).

81. Mullard Technical Handbook, Part 2, Mullard: London, (1970).

82. Hall, C., 'Polymer Materials - an introduction for technologists and scientists', Macmillan: London, (1981).

83. Pratt, G.J. and Smith, M.J.A., Polymer, 27, 1483, (1986).

84. Deutsch, K., Hoff, E.A.W. and Reddish, W., J. Polym. Sci., 13, 565, (1954).

85. Mashimo, S., Yagihara, S. and Iwasa, Y., J. Polym. SCi., Poly. Phys. Edn., 16, 1761, (1978).

86. Rutherford, H. and Soutar, I., J. Polym. Sci. Lett. Edn., 16, 131, (1978).

87. Powles, J.G. and Hunt, B.I., Phys. Letters, 14, 202, (1965).

88. Sreehari Sastry, S., Sundar Raj, T.P., Satyanandam, G. and Heyraj, M., IEE Conf. 289, 121, (1988).

89. Schoon, T.G.F. and Teichmann, O., Kolloid-Z, 197, 35 and 45, (1964).

90. Rochow, T.W., J. Appl. Poly. Sci., 9, 569, (1965).

91. Reddish, W., 'Polymers for Electrical Insulation: a review of dielectric properties in relation to structure', Materials Science Club Bulletin, Imperial Chemical Industries Ltd., UK, (1974).

92. Scheiber, D.J., J. Research Natl. Bur. Standards, 65C, 23, (1961).

93. Lobanov, A.M., Mirkamilov, D.M. and Platonov, P., Vsyokomol. Soed., A-10, 1116, (1968).

94. Reddish, W., Pure and Appl. Chem, 5, 723, (1962).

95. Pratt, G.J. and Smith, M.J.A. private communication (1988).

96. Mikhailov, G.P., Lobanov, a.M. and Sazhin, B.I., J. Tech. Phys. (USSR), 25, 590, (1954).

97. McCrum, N.G., Read, B.E. and Williams, G., 'Anelastic and Dielectric Effects in Polymeric Solids', John Wiley: N.Y., (1967).

98. Stuart, H.A., Pure and Appl. Chem., 5, 743, (1962).

99. Bergmann, K., J. Polym. Sci., 16, 1611, (1978).

100. Fischer, E.W., Discussions Faraday Soc., 25, 204, (1958).

101. Rempel, R.C. and others, J. Appl. Phys. 28, 1082.

102. Schmieder, K. and Wolf, K., Kolloid, Z., 134, 149, (1953).

103. Takayanagi, M., Mem. Fac. Eng. Kyushu Univ., 23, 1, (1963).

104. Mikhailov, G.P., Kabin, S.P. and Krylova, T.A., J. Tech. Phys. (USSR), 27, 2050, (1957).

105. Salla Tarago, J.M., Diaz Calleja, R. and Guzman, G.M., Polymer Communications, 27, 11, (1986).

106. Kline, D.e., Sauer, J.A. and Woodward, A.E., J. Polym. Sci., 22, 455, (1956).

107. Powles, J.G. and Oakes, W.G., Nature, 157, 840, (1946).

108. Jackson, W. and Forsyth, S., J. IEE, 92, 111, (1945).

109. Tuijnman, C.A.F., Polymer, 4, 259, (1963).

BIBLIOGRAPHY

1. Hedvig, P., 'Dielectric Spectroscopy of Polymers', Adam Hilger: Bristol, (1977)
2. Afsar, M.N., Birch, J.R. and Clarke, R.N., 'The Measurement of the Properties of Materials', Proc.IEEE 74, 1, 183, (1986)
3. Coll, J., 'The BBC Microcomputer User Guide', The British Broadcasting Corporation: London, (1982)
4. Bray, A.C., Dickens, A.C. and Holmes, M.A., 'The Advanced User Guide for the BBC Microcomputer', Cambridge Microcomputer Centre, (1983)
5. Pring, P.C.J. and Smith, M.J.A., 'Dielectric Materials, Measurements and Applications', IEE Conf. 289, 326-327, (1988)

TITLE A Wideband Spectrometer for the Measurement of Permittivity

AUTHOR Philip Charles Jarrett Pring

INSTITUTION and DATE University of Warwick
1989